# Assessing the accuracy of artificial intelligence synthetic CT generation for liver and brain MRI-only radiotherapy

**Lamyaa Khalid Aljaafari**

Submitted in accordance with the requirements for the degree of Doctor of Philosophy


The University of Leeds

School of Medicine

September 2025

# Intellectual Property and Publication Statements

I confirm that the work submitted is my own, except where work which has formed part of jointly authored publications has been included. My contribution and the other authors to this work has been explicitly indicated below. I confirm that appropriate credit has been given within the thesis where reference has been made to the work of others.

Chapter 3 is based on work from the jointly authored publication:

Aljaafari L, Bird D, Buckley DL, Al-Qaisieh B, Speight R. A systematic review of 4D magnetic resonance imaging techniques for abdominal radiotherapy treatment planning. Physics and Imaging in Radiation Oncology. 2024; 31:100604. https://doi.org/10.1016/j.phro.2024.

Lamyaa Aljaafari was responsible for conducting the systematic review, including data collation, analysis, drafting the manuscript, and responding to reviewers' comments. All co-authors reviewed the paper, provided feedback on written drafts, and contributed supervision and guidance throughout the project.

Chapter 4 is based on work from the jointly authored publication:

Aljaafari L, Speight R, Buckley DL, Al-Qaisieh B, Andersson S, Bird D. Evaluating the dosimetric and positioning accuracy of a deep learning based synthetic-CT model for liver radiotherapy treatment planning. Biomed Phys Eng Express. 2025; 11:035014. https://doi.org/10.1088/2057-1976/adc818.

Lamyaa Aljaafari was responsible for collecting, preparing, and analysing the data, training and testing the model, interpreting the results, drafting the manuscript, and responding to reviewers' comments. All co-authors provided essential guidance for the study design, supervision, and reviewed the paper and provided feedback on written drafts.

Chapter 5 is based on work from the jointly authored publication:

Aljaafari L, Speight R, Buckley DL, Bird D, Al-Qaisieh B. Clinical validation of using a commercial synthetic-computed tomography solution for brain MRI-only radiotherapy treatment planning. Technical Innovations and Patient Support in Radiation Oncology. 2025; 35:100328. https://doi.org/10.1016/j.tipsro.2025.

Lamyaa Aljaafari was responsible for collecting, preparing, and analysing the data, interpreting the results, drafting the manuscript, and responding to reviewers' comments. All co-authors provided essential guidance for the study design, supervision, and reviewed the paper and provided feedback on written drafts.

## Acknowledgements

I owe my sincere thanks to many people whose patience, guidance, expertise, and encouragement made the completion of this work possible.

I would like to start by thanking my supervisors for believing in me. I am fortunate to have worked with a professional, knowledgeable, respectful, and supportive team. Dr Richard Speight, thank you for your kindness and constant availability when I needed you, and for supporting me when things did not go as planned. Dr David Bird, special thanks for your day-to-day assistance, for keeping me on track, for giving me both freedom and responsibility, and for your honest opinions. Prof David Buckley, thank you for sharing your expertise in MRI and research, and for your academic guidance during my PhD. Dr Bashar Al-Qaisieh, I am profoundly grateful; I cannot imagine this journey without you. Your support, both professional and personal, has been invaluable, and I have always valued your ability to keep sight of the bigger picture, within this project and life. Thank you for the countless hours you set aside to support me; your time and guidance made all the difference.

I gratefully acknowledge the Kingdom of Saudi Arabia and King Saud bin Abdulaziz University for Health Sciences for their generous financial support, which made this research possible.

Thank you to all my colleagues in LICAMM, who I was fortunate to know during my PhD journey. I also thank Karen Porter, Malenka Bissell, and Dawn Best from the International PhD Academy for their kindness and academic encouragement.

I owe my deepest thanks to my family for their unwavering love, patience and encouragement. To my parents: thank you for your constant prayers; your belief in me has anchored me throughout this PhD. I am especially grateful for every time you travelled to the UK to be by my side; your time, sacrifices and support made this journey possible and meant the world to me. To my siblings, thank

you for always listening and for keeping me going when it was hard. To my family-in-laws, I am deeply grateful for your love, your prayers and your steadfast support.

To my husband, Mohammed: words cannot fully express my gratitude. Your love, patience, and understanding made this PhD possible. Thank you for believing in my dream and standing beside me at every step; your enduring partnership has been my greatest source of strength.

To my daughter, Almaha: you lived this PhD with me, from late nights and early mornings to quiet weekends and sudden bursts of hope and worry. Thank you for your love and patience, and for bringing joy even to the hardest days. You filled our home with laughter when I needed it most. Your everyday hugs made the longest days feel lighter. You often asked when I would finish so we could go back to our family; I know the wait was long for you. This is the thesis we have both been waiting for. I am endlessly proud of you; this achievement is ours!

My heartfelt thanks to Frank and Queeny, who I met in Leeds and became invaluable friends. Frank, thank you for every morning's help with transport and for the encouragement that began each day; your words 'you are a superwoman!' never failed to lift my spirits. Queeny, thank you for your kindness, encouragement, and friendship; your support meant a great deal.

Lastly, special thanks to my friend Nouf Alzahrani for her personal support and encouragement during my journey. Thank you for being there.

# Abstract

**Background:** Magnetic resonance imaging (MRI) is increasingly integrated into radiotherapy because of its superior soft-tissue contrast compared with computed tomography (CT). This has prompted interest in four-dimensional (4D) MRI for motion management and MRI-only radiotherapy using synthetic CT (sCT) for dose calculation and patient positioning verification. This thesis aimed to provide clinical evidence for the technical feasibility and clinical implementation of MRI-only radiotherapy for liver and brain cancer.

Methods: (i) A PRISMA-guided systematic review of the 4D MRI literature for abdominal radiotherapy was conducted. (ii) A deep-learning sCT model was developed using clinical MRI and CT data to generate liver MRI-only radiotherapy. (iii) The performance of a commercial sCT solution (Philips MRCAT) was assessed for brain MRI-only radiotherapy. For both liver and brain, dosimetric accuracy was evaluated using dose volume histogram (DVH) analysis. In addition, image guided patient positioning was verified using the clinical XVI system.

**Results:** (i) The systematic review, encompassing 39 studies, indicated that 4D MRI had the potential to improve abdominal radiotherapy by enabling accurate tumour definition and motion characterisation compared to 4D CT. (ii) For the liver sCT model, relative mean dose differences between CT and sCT were 0.0% for the planning target volume (PTV) and <0.5% for all organs at risk (OARs). Positioning verification revealed mean translational and rotational differences of <0.5 mm and <0.5°, respectively. (iii) For the brain MRCAT, relative mean dose differences were <0.4% for the PTV and <0.3% for OARs, with positioning accuracy maintained within ±1 mm and ±1°.

**Conclusion:** 4D MRI shows considerable promise for motion management, but its clinical implementation remains limited, by lack of robust clinical validation or standardisation. Both liver and brain sCT models demonstrated dosimetric and positioning accuracy comparable to CT, confirming the technical feasibility of MRI-only radiotherapy for the liver and its clinical applicability for the brain.

# Table of Contents

# List of Figures

# List of Tables

## Ethics approvals related to this work

The work in this thesis uses retrospective datasets covered by the Leeds Cancer Centre Computer Aided Theragnostics (LeedsCAT) research database Trust ethical approval. This approval was granted by the LeedsCAT Governance Board, which consists of representatives from the Trust ethics; Research & Innovation, Information Governance, patient and public involvement (PPI), and experts in radiotherapy. All necessary ethical approvals were obtained prior to data collection and analysis. Patient data were anonymised before analysis, and no identifiable information was retained.

A copy of the ethical approval forms is provided in the Appendix D.

# Abbreviation

**3D CRT: Three-dimensional conformal radiotherapy**

**4D CBCT: Four dimensional cone-beam CT**

**4D CT: Four dimensional CT**

**4D MRI: Four dimensional MRI**

**4D sCT: 4D synthetic CT**

**AI: Artificial intelligence**

**$B_0$: Magnetic field**

**CBCT: Cone beam CT**

**CC: Cross corelation**

**CNNs: Convolutional neural networks**

**CNS: Central nervous system**

**CT: Computed Tomography**

**CTV: Clinical target volume**

**DIR: Deformable images registration**

**DL: Deep learning**

**DVH: Dose volume histogram**

**EBRT: External beam radiation therapy**

**FFF: Flattening filter-free**

**FLAIR: Fluid attenuated inversion recovery**

**FOV: Field of view**

**GANs: Generative adversarial networks**

**GTV: Gross tumour volume**

**HCC: Hepatocellular carcinoma**

**HU: Hounsfield Units**

**IGRT: Image-guided radiotherapy**

**IMRT: Intensity-modulated radiotherapy**

**ITV: Internal target volume**

**LC: Local control**

**LCC: Leeds Cancer Centre**

**linac: Linear accelerator**

**MAD: Mean absolute differences**

**MAE: Mean absolute error**

**MI: Mutual information**

**MidV: Mid-ventilation**

**MLC: Multi-leaf collimator**

**MRCAT: Magnetic Resonance Calculating ATtenuation**

**MRF: Magnetic Resonance Fingerprinting**

**MRgRT: MR-guided radiotherapy**

**MRI: Magnetic Resonance Imaging**

**Mxy: Transverse magnetisation**

**Mz: Longitudinal alignment**

**NMV: Net magnetisation vector**

**OAR: Organ at risk**

**OS: Overall survival**

**PCA: Principal component analysis**

**PCC: Pearson correlation coefficient**

**PRISMA: Preferred Reporting Items for Systematic Reviews and Meta-Analyses**

**PTV: Planning target volume**

**QA: Quality assurance**

**RC-4D MRI: Respiratory-correlated 4D MRI**

**RF: Radiofrequency**

**RIR: Rigid image registration**

**RMSE: Root mean square error**

**ROI: Region of interest**

**RT: Radiation Therapy**

**SABR: Stereotactic ablative radiotherapy**

**sCT: Synthetic CT**

**SI: Superior inferior**

**SE: Spin Echo**

**SRS: Stereotactic radiosurgery**

**SRT: Stereotactic radiotherapy**

**SSIM: Structure similarity index measure**

**T1w: T1-weighted images**

**T2w: T2-weighted images**

**TACE: Trans-arterial chemoembolization**

**TE: Echo time**

**TPS: Treatment planning system**

**TPS: Treatment planning system**

**TR-4D MRI: Time-resolved 4D MRI**

**TR: Repetition time**

**UQ: Ultra-quality**

**UTE: Ultra-short echo time**

**VIBE: Volumetric interpolated breath-hold examination**

**VMAT: Volumetric-modulated arc therapy**

**XVI: X-ray Volumetric Imaging**

# Chapter 1 Introduction and scope of this work

## 1.1 Introduction

The use of magnetic resonance imaging (MRI) in radiotherapy has increased over the past decades [1]. For many years, computed tomography (CT) has been the primary imaging modality for delineation, treatment planning, and patient setup and positioning during treatment due to its geometrical accuracy and electron density information [2]. However, MRI brings several advantages over CT, including superior soft-tissue contrast, functional imaging capabilities, and the ability to provide biological information [2-6]. Recently, interest in using four dimensional MRI (4D MRI) for motion management in radiotherapy has increased, as it also offers non-ionising imaging with the potential for reducing artefacts, and flexible spatial, temporal, and contrast resolutions to meet radiotherapy clinical requirements [7, 8].

Currently, MRI has been used as a complementary imaging modality to CT, aiding in target delineation. This workflow requires image registration to CT images, a process of transferring anatomical points from the floating MRI image to the reference CT image. The challenges in this process include the need to acquire both scans, which requires additional resources, complicates the workflow, and, most importantly, can introduce registration errors due to potential variations in patient setup and internal organ motion between scans [9-13]. Thus, interest is growing in MRI-only treatment planning, where MRI serves as the sole imaging modality without the need for traditional CT scans [11]. With the availability of dedicated MRI scanners for radiotherapy (known as MRI simulators), which are optimised and installed for radiotherapy purposes, MRI-only radiotherapy is becoming gradually adapted by many centres worldwide.

However, MRI-only radiotherapy requires the development of synthetic CT (sCT) images generated from MRI, also known as substitute or pseudo-CTs, to provide necessary electron density information for dose calculation [14-17]. In addition to dose calculation, sCT images must be suitable as a reference image for patient setup and positioning verification during treatment delivery using cone beam CT (CBCT) clinical positioning software, which typically relies on a CT scan as the reference image. Therefore, evaluating the suitability of sCT

images for dose calculation and as reference images is essential for the implementation of MRI-only radiotherapy.

This makes accurate sCT development a crucial part of MRI-only radiotherapy. As a result, sCT generation has been developed and validated for certain anatomical treatment sites, each with its own challenges [11, 13-18]. However, significant research and development are still needed such as in the liver along with further clinical validation in sites such as the brain to enable widespread clinical implementation.

## 1.2 Thesis motivation

The motivation for this thesis came from the growing interest at Leeds Cancer Centre (LCC), St James' Hospital, in enhancing cancer care through the implementation of MRI-only radiotherapy workflows. This approach represents an important part of the future of radiotherapy planning. In 2023, a dedicated MRI simulator (Philips Ingenia MR-RT ) was installed in the department, increasing the use of MRI in radiotherapy and allowing MRI-only treatment planning for various anatomical sites. However, implementing MRI-only radiotherapy requires a comprehensive validation of sCT tools available in a clinical setting. The Philips Brain MRCAT solution was used for sCT generation.

Additionally, LCC will be the first centre in the UK to implement a dedicated 4D MRI sequence for radiotherapy purposes, developed by Philips for clinical use on our MRI simulator. This sequence is an essential aspect of implementing MRI-only radiotherapy for liver as an alternative to four dimensional CT (4D CT). Therefore, it is critical to understand existing 4D MRI methodologies and technical aspect to guide clinical implementation. The initial objective for this PhD was to conduct a clinical validation study comparing 4D MRI to 4D CT in patients with liver cancer. However, due to delays with our research collaboration partner (Philips), this study was postponed and does not form part of the thesis.

## 1.3 Aims, hypothesis and research questions

### 1.3.1 Aims

This thesis aims to investigate the clinical feasibility of MRI-only radiotherapy compared to the current MRI/CT workflow in brain and liver radiotherapy. The specific objectives are as follows:

1. To explore the current evidence on the use of 4D MRI in abdominal radiotherapy and to understand the existing challenges and limitations through a comprehensive systematic review of the literature.
2. To assess the dosimetric accuracy and patient positioning verification of a research sCT model developed in collaboration with RaySearch Laboratories, including preparing and pre-processing the local MRI/CT datasets and training the deep learning (DL) model for liver radiotherapy.
3. To assess the dosimetric accuracy and patient positioning verification of a commercial sCT solution developed by Philips for brain radiotherapy.

### 1.3.2 Hypothesis

The hypothesis tested for aims 2 and 3 is that MRI-only radiotherapy for liver and brain cancers is technically feasible and clinically implementable, supported by the use of artificial intelligence based sCT generation models. It is hypothesised that both models will generate sCT images that demonstrate clinically acceptable dosimetric accuracy and suitability for patient positioning verification, thereby supporting their clinical feasibility for MRI-only radiotherapy workflows.

### 1.3.3 Research questions

1. Is 4D MRI a feasible and sufficiently accurate technique for motion management in abdominal radiotherapy?
2. Can a deep learning model generate clinically acceptable sCT for liver MRI-only radiotherapy using routine clinical data, in terms of dosimetric accuracy and patient positioning using Elekta X-ray volumetric imaging (XVI) 4D CBCT-based registration?
3. How accurate is the commercial Philips sCT solution for MRI-only brain radiotherapy in term of dose calculation and Elekta XVI CBCT-based positioning system, compared to the standard CT-MRI workflow?

## 1.4 Thesis outline

The chapters of this thesis present the work undertaken for the clinical validation of synthetic CT tools developed for MRI-only radiotherapy in liver and brain cancers.

Chapter 2 summarises the background and literature review relevant to the work presented, with a particular focus on the role of MRI in radiotherapy and the growing interest in MRI-only workflow. It also includes a description of the current clinical workflow. Additional literature reviews and study-specific discussions are included within the individual chapters.

Chapter 3 presents a systematic review of 4D MRI methodologies, with a specific focus on 4D MRI techniques and their validation in patients undergoing abdominal radiotherapy treatment planning. The review highlights the need for a robust 4D MRI solution to enable liver MRI-only workflows for clinical implementation. This chapter has been published in *Physics and Imaging in Radiation Oncology* (see Appendix E for the published article).

Chapter 4 presents the clinical feasibility of sCT images for liver MRI-only radiotherapy. The study evaluates a deep learning-based sCT model developed in collaboration with RaySearch Laboratories, which is currently available for research use only but has strong potential for future clinical implementation. This work is the first study of its kind to assess the model's performance for the liver, focusing on both dosimetric accuracy and patient positioning verification using four dimensional cone-beam CT (4D CBCT) on the Elekta XVI system. This chapter has been published in *Biomedical Physics & Engineering Express* (see Appendix E for the published article).

Chapter 5 presents the clinical validation of a commercial sCT solution for an MR only pathway for brain radiotherapy treatment planning. The study evaluates MRCAT, a deep learning-based sCT model developed by Philips, focusing on its dosimetric accuracy and suitability for patient positioning verification using CBCT image registration on the Elekta XVI system. The model was assessed in a large patient cohort to demonstrate its robustness and generalisability across patient population. This chapter has been published in *Technical Innovations & Patient Support in Radiation Oncology* (see Appendix E for the published article).

Chapter 6 summarises the work presented, highlights key findings, and discusses directions for future research.

## 1.5 References


[1] Chandarana H, Wang H, Tijssen R, Das IJ. Emerging role of MRI in radiation therapy. Journal of Magnetic Resonance Imaging. 2018;48:1468-78

[2] Pereira GC, Traughber M, Muzic RF, Jr. The role of imaging in radiation therapy planning: past, present, and future. Biomed Res Int. 2014;2014:231090. 10.1155/2014/231090.

[3] Srinivasan S, Dasgupta A, Chatterjee A, Baheti A, Engineer R, Gupta T, et al. The promise of magnetic resonance imaging in radiation oncology practice in the management of brain, prostate, and GI malignancies. JCO Global Oncology. 2022;8:e2100366

[4] Scheenen TW, Zamecnik P. The role of magnetic resonance imaging in (future) cancer staging: note the nodes. Investigative Radiology. 2021;56:42-9

[5] McGee KP, Cao M, Das IJ, Yu V, Witte RJ, Kishan AU, et al. The Use of Magnetic Resonance Imaging in Radiation Therapy Treatment Simulation and Planning. Journal of Magnetic Resonance Imaging. 2024;60:1786-805

[6] Goodburn RJ, Philippens MEP, Lefebvre TL, Khalifa A, Bruijnen T, Freedman JN, et al. The future of MRI in radiation therapy: Challenges and opportunities for the MR community. Magn Reson Med. 2022;88:2592-608. 10.1002/mrm.29450.

[7] Li G, Liu Y, Nie X. Respiratory-Correlated (RC) vs. Time-Resolved (TR) Four-Dimensional Magnetic Resonance Imaging (4DMRI) for Radiotherapy of Thoracic and Abdominal Cancer. Front Oncol. 2019;9:1024. https://dx.doi.org/10.3389/fonc.2019.01024.

[8] Stemkens B, Paulson ES, Tijssen RHN. Nuts and bolts of 4D-MRI for radiotherapy. Phys Med Biol. 2018;63:21TR01. https://doi.org/10.1088/1361-6560/aae56d.

[9] Ulin K, Urie MM, Cherlow JM. Results of a multi-institutional benchmark test for cranial CT/MR image registration. Int J Radiat Oncol Biol Phys. 2010;77:1584-9. https://doi.org/10.1016/j.ijrobp.2009.10.017.

[10] Brock KK, Mutic S, McNutt TR, Li H, Kessler ML. Use of image registration and fusion algorithms and techniques in radiotherapy: Report of the AAPM Radiation Therapy Committee Task Group No. 132. Med Phys. 2017;44:e43-e76. 10.1002/mp.12256.

[11] Owrangi AM, Greer PB, Glide-Hurst CK. MRI-only treatment planning: benefits and challenges. Physics in Medicine & Biology. 2018;63:05TR1

[12] Persson E, Svanberg N, Scherman J, Jamtheim Gustafsson C, Fridhammar A, Hjalte F, et al. MRI-only radiotherapy from an economic perspective: Can new techniques in prostate cancer treatment be cost saving? Clin Transl Radiat Oncol. 2023;38:183-7. 10.1016/j.ctro.2022.11.012.

[13] Jonsson J, Nyholm T, Söderkvist K. The rationale for MR-only treatment planning for external radiotherapy. Clinical and Translational Radiation Oncology. 2019;18:60-5. https://doi.org/10.1016/j.ctro.2019.03.005.

[14] Spadea MF, Maspero M, Zaffino P, Seco J. Deep learning based synthetic-CT generation in radiotherapy and PET: A review. Med Phys. 2021;48:6537-66. 10.1002/mp.15150.

[15] Boulanger M, Nunes J-C, Chourak H, Largent A, Tahri S, Acosta O, et al. Deep learning methods to generate synthetic CT from MRI in

radiotherapy: A literature review. Physica medica. 2021;89:265-81. https://doi.org/10.1016/j.ejmp.2021.07.027.

[16] Johnstone E, Wyatt JJ, Henry AM, Short SC, Sebag-Montefiore D, Murray L, et al. Systematic Review of Synthetic Computed Tomography Generation Methodologies for Use in Magnetic Resonance Imaging-Only Radiation Therapy. Int J Radiat Oncol Biol Phys. 2018;100:199-217. 10.1016/j.ijrobp.2017.08.043.

[17] Edmund JM, Nyholm T. A review of substitute CT generation for MRI-only radiation therapy. Radiation oncology (London, England). 2017;12:28-. 10.1186/s13014-016-0747-y.

[18] Bird D, Henry AM, Sebag-Montefiore D, Buckley DL, Al-Qaisieh B, Speight R. A Systematic Review of the Clinical Implementation of Pelvic Magnetic Resonance Imaging–Only Planning for External Beam Radiation Therapy. International Journal of Radiation Oncology*Biology*Physics. 2019;105:479-92. https://doi.org/10.1016/j.ijrobp.2019.06.2530.

# Chapter 2 Background and literature review

## 2.1 Radiotherapy in cancer management

In 2022, there were 346,217 diagnosed new cancer cases in England [1]. Cancer is responsible for approximately one in four of all deaths in the United Kingdom [2]. Cancer is a disease defined by the rapid and uncontrolled growth of abnormal cells, which can originate and spread to any part of the body [3]. Treatment management for cancer includes surgery, chemotherapy, radiotherapy, and increasingly immunotherapy [4] or a combination of these treatments. Around 50% of the patients diagnosed with cancer undergo radiotherapy at some point during their treatment [5].

Radiotherapy, also known as radiation therapy (RT), uses ionising radiation to destroy the cancerous cells by depositing energy that damages their DNA, leading to cell death [6]. Although radiation affects both cancerous and normal tissues along its path, normal tissues are generally able to repair the damage faster and more effectively than cancer cells [6]. The goal is to deliver the radiation dose precisely to a defined target volume while minimising exposure to healthy tissues. Radiotherapy can be given with four different intents: radical (curative), to completely eradicate cancer; adjuvant, to reduce the risk of local recurrence following primary treatment; neoadjuvant, given before primary treatment to shrink the tumour; or palliative, to relieve symptoms [6, 7]. The most common method of delivering radiation is external beam radiation therapy (EBRT), which uses a machine called a linear accelerator (linac) to deliver radiation beams from outside the body to the tumour [8]. The radiation dose, prescribed by the clinician, can vary depending on the cancer type, location and treatment goals. The total prescribed dose is divided into smaller amounts, known as fractions, and delivered over multiple treatment sessions, usually daily. This fractionated approach allows healthy tissues time to repair between treatment sessions, helping to minimise side effects [9].

### 2.1.1 Liver cancer

In the UK, approximately 6,200 new liver cancer cases are diagnosed annually, which has increased by 45% over the last decade [10]. The five-year survival rate for patients with liver cancer is 13.7% [10]. Treatment options for primary or metastatic liver cancer depend on the stage of the disease, the

patient's condition, and other factors. Surgical interventions such as resection or transplantation are possible if the cancer is diagnosed early; however, many liver tumours are unresectable at the time of diagnosis [10]. Other options include ablation therapy, trans-arterial chemoembolization (TACE), and radiotherapy [10]. In liver radiotherapy, higher-dose fractions have gained interest as a treatment option, delivered using stereotactic ablative radiotherapy (SABR) [10, 11]. Its benefits have been reported in terms of overall survival (OS), local control (LC), and toxicity [12-15]. SABR is a highly targeted form of radiotherapy that delivers a precise, high-dose of radiation in fewer fractions compared to conventional radiotherapy. Liver cancer can originate in the liver (i.e., hepatocellular carcinoma) or spread from other parts of the body (called secondary or metastatic liver cancer), most commonly from colorectal, followed by pancreatic and breast cancer [16]. Based on LCC clinical protocols, the prescribed dose for primary and metastatic liver tumours typically ranges from 40 to 60 Gy delivered in 5 fractions, typically daily. To ensure successful SABR treatment, precise tumour delineation and motion management are essential to deliver a high dose to the tumour while limiting the exposure of healthy tissue to high radiation doses. The accuracy of treatment delivery should be about 1 mm [17], allowing minimal margin for error throughout the process.

### 2.1.2 Brain cancer

Over 12,288 new brain tumour cases are diagnosed annually in the UK, accounting for 3% of all new cancer diagnoses and ranking as the ninth most common cause of cancer death [18]. Survival rates remain low, with a 10-year survival rate of less than 11% and over 5,456 deaths annually [18]. Over the past decade, the incidence rate of brain tumours has increased by 9%, highlighting the need for improved treatment options [18]. Brain tumours can be either primary or metastases. Primary brain tumours consist mostly of gliomas, which account for around 80 % of central nervous system (CNS) tumours [19]. Glioblastoma is the most common malignant subtype in adults. It is highly aggressive and fast-growing, making it the lethal primary CNS cancer, with a median survival of 12–18 months after treatment [20, 21]. Treatment of primary brain tumours typically begins with surgical resection, if feasible, to limit tumour growth, relieve symptoms, prolong survival, and improve quality of life; this is commonly combined with radiotherapy and chemotherapy, followed by a six-

month course of adjuvant chemotherapy, which has been shown to increase two-year survival rates [22-24]. In LCC, the standard prescribed dose for radical treatment of brain tumours ranges from 50.4 Gy to 60 Gy, delivered over 28 to 30 fractions, depending on the type, size, location, and grade of the brain tumours.

Secondary brain metastases most commonly originate from the lung, breast, or skin [25]. Median survival ranges from a few months to about a year, and untreated patients survive only around three months [26]. Treatment for brain metastases is most often palliative, including surgery, radiotherapy, or targeted/immunotherapy or combined depending on the number, size, and location of lesions and the primary tumour site [26]. Surgery is the treatment of choice for resectable lesions; another option is advanced radiotherapy techniques include stereotactic radiosurgery (SRS) or stereotactic radiotherapy (SRT), which deliver high doses in a single or a few fractions to the surgical cavity shortly after surgery to minimise tumour recurrence [27] or directly to the lesions [28]. If SRS/SRT are not suitable, partial-brain or whole-brain radiotherapy can be used [26, 29]. At LCC, palliative radiotherapy typically delivers 30-40 Gy in 6–15 fractions.

## 2.2 Overview of the radiotherapy workflow

Radiotherapy is a multidisciplinary and comprehensive process involving several key stages, including pre-treatment, treatment planning, and treatment delivery. As modern techniques become more advanced, the risk of errors also increases if each step is not carefully managed. To ensure safe and effective treatment, each member of the clinical team plays a critical role: clinicians must accurately define and contour the target and surrounding healthy tissues; medical physicists or dosimetrists are responsible for producing an optimal treatment plan that delivers the prescribed dose while minimising exposure to healthy tissue; and radiographers must ensure precise patient positioning at the time of treatment delivery. The following sections will describe each of these stages in detail, with a focus on liver and brain radiotherapy.

### 2.2.1 The role of imaging in radiotherapy

Medical imaging is integrated into every stage of the radiotherapy process to ensure accuracy, consistency, and precision in treatment delivery.

### 2.2.2 Basic CT physics

CT has been recognised as the principal imaging modality [30] and is based on X-ray imaging with a rotating X-ray tube and multiple detectors surrounding the patient to produce cross-sectional images of the body. As the X-ray beam passes through the body, it interacts with different tissues and may be absorbed, scattered, or transmitted to the detectors. These interactions vary based on tissue density, e.g., fat, muscle, and bone, which create an attenuation map. The attenuated X-rays are reconstructed into a 3D image using computational techniques such as filtered back projection or more recently via iterative methods, with each voxel's intensity measured in Hounsfield Units (HU). HU provide a quantitative measure of tissue X-ray attenuation relative to water and air and are defined as:

$$HU = 1000 \times \frac{\mu_{tissue} - \mu_{\text{water}}}{\mu_{\text{water}}}$$

Where $\mu_{tissue}$ is the linear attenuation coefficient of the tissue and $\mu_{\text{water}}$ is the linear attenuation coefficient of water.

HU is approximately proportional to a tissue's electron density, which is fundamental for calculating the radiation dose deposited in the body. This relationship is established through the HU-to-electron density calibration curve, which converts CT HU into relative electron densities compared to water for different tissues, enabling a treatment planning system (TPS) to calculate the dose accurately [31].

Despite its widespread clinical use and importance for dose calculation, CT imaging has inherent limitations in terms of soft-tissue contrast. Image contrast in CT is derived from differences in X-ray attenuation, and many soft tissues show similar attenuation coefficients, resulting in overlapping HU values. Consequently, differentiation between soft tissues such as muscle, organs, and tumours can be challenging, which motivates the use of complementary imaging modalities,

In addition to dose calculation, the planning CT is used as a reference image for patient position verification before treatment delivery. In the treatment room, CT-based image-guided radiotherapy (IGRT) is also used to ensure precise patient setup and to correct for any positioning errors during radiation delivery [32, 33]. A guideline outlining the requirements for CT scanning has

been established to ensure accuracy in treatment planning and delivery [34]. Although CT provides the necessary precision in localising the anatomical positioning of the tumour and adjacent healthy organs, it has poor soft tissue contrast in various treatment sites [32]. Therefore, many treatment sites also rely on MRI for accurate target delineation—this will be discussed further in section 2.2.3.2

### 2.2.3 Pre-treatment

#### 2.2.3.1 CT simulation

CT simulation is a crucial step in the radiotherapy workflow. It provides detailed 3D images of the patient in the exact treatment position, offering accurate spatial location of the tumour, and organ at risks (OAR) [35]. This stage includes the immobilisation process, which involves the use of a flat-top couch, positioning devices and a laser positioning system to ensure consistent and reproducible patient positioning for each treatment session (as shown in Figure 2.1). It also helps to minimise co-registration errors between the MRI and CT scans.

The treatment position at LCC for liver SABR radiotherapy involves the patient immobilised in a supine position with arms raised above the head to clear the treatment field, supported by a vacuum bag and knee support. To reduce respiratory motion during pre-treatment imaging and throughout treatment delivery, abdominal compression is used by applying controlled pressure to the upper abdomen. Three reference points positioned anteriorly and laterally at patient skin to ensure reproducible setup. Lastly, 50 ml of water is taken orally to improve stomach and bowel visibility. Two scans are acquired. 3D CT images are acquired during an exhalation breath-hold to minimise motion and ensure a reproducible liver position for delineation. These images are used for planning and as a reference for patient positioning during treatment. Four-dimensional CT (4D CT) is acquired during free breathing to measure respiratory motion using the liver boundary, which is visible on CT, as a surrogate for internal tumour motion; this helps define tumour margins that account for motion.

For brain radiotherapy the patient is immobilised in the supine position using a thermoplastic head mask with three reference points, two lateral points,

one superior point at the top of the head, laser positioning markers, and neck and knee supports to reduce setup uncertainties and reproduce the same positioning during treatment. Only a 3D CT scan is typically required for simulation, as the brain is a fixed organ with minimal internal motion.

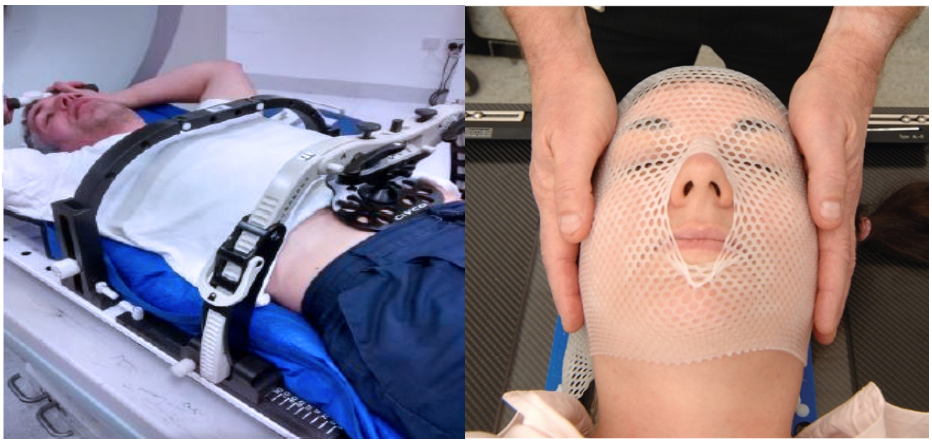

**Figure 2.1: Examples of immobilisation devices used in liver and brain radiotherapy to ensure accurate and reproducible patient positioning throughout treatment, replicated from [36, 37]**

#### 2.2.3.1.1 4D CT in liver radiotherapy

4D CT, also known as respiration-correlated CT, is currently the standard method for motion management in liver radiotherapy [38]. It allows clinicians to assess respiratory-induced organ motion, which is essential for accurate target localisation and treatment planning. The 4D CT imaging depends on acquiring sufficient data at each couch position over one full breathing cycle, and the time needed for image reconstruction [39, 40]. For this a respiratory surrogates is used to match breathing motion with acquired image set. These surrogates are most commonly external, such as optical tracking systems [41] or abdominal pressure belts [42]. Alternatively, internal surrogates can be used, such as implanted fiducial markers [43] or internal respiratory signal measurements [44].

4D CT images are acquired by capturing multiple 2D projections throughout the patient's breathing cycle, which are linked to a respiratory surrogate and sorted into respiratory bins to create multiple phase 2D slices (typically ten per cycle). The binned 2D slices are then reconstructed to form 3D

images. These 3D image sets can be viewed sequentially as a cine loop to visualise respiratory motion. There are two primary approaches to binning: phase-based and amplitude-based. Figure 2.2 shows a graphical illustration of phase and amplitude binning methods used in 4D CT acquisition. In phase-binning, images are sorted into phase bins based on the respiratory phase recorded at the time of image acquisition. Bins are defined as percentages of the breathing cycle, with 0% typically corresponding to peak inhalation. In amplitude binning, images are sorted based on the magnitude of the breathing signal, ranging from maximum to minimum amplitudes, which correlate with diaphragm motion, where 0% usually represents end-exhalation. Amplitude binning has been shown to improve image quality and reduce motion artefacts such as blurring, overlapping, and distorted anatomical structures compared to phase binning [45, 46]. However, it is more sensitive to irregular breathing patterns, which can lead to insufficient data for reconstruction [45, 46].

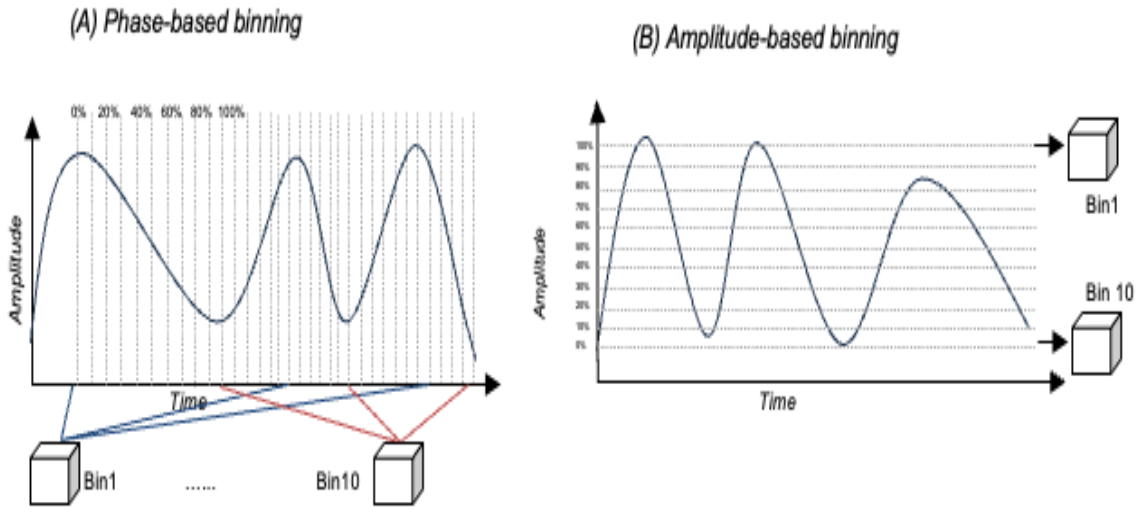


**Figure 2.2: Graphical representation of 4D CT image reconstruction using (a) phase-based binning and (b) amplitude-based binning. In phase-based binning, the respiratory signal is divided into equally spaced phases ranging from 0% to 100%. In amplitude-based binning, data are grouped based on the amplitude of the respiratory signal. Figure adapted from [47].**

While 4D CT is widely used in clinical practice, artefacts are common and have been reported in up to 90% of clinical scans [46]. These artefacts can result from irregular breathing, coughing, bin-sorting errors, or suboptimal scan parameters, and typically manifest as blurring, duplication, or incomplete anatomical structures. The clinical impact of these artefacts depends on their

severity and proximity to the treatment target, as they can negatively affect local control [48]. However, this does not necessarily mean they are clinically unusable. Another important limitation is that external respiratory surrogates do not accurately reflect the actual motion of internal organs or the tumour due to complex, patient-specific anatomical variations [38]. This challenge becomes more relevant in liver, where another key limitation of 4D CT is its poor soft tissue contrast in the abdomen, making accurate tumour delineation challenging. As a result, the liver dome or diaphragm is often used as an internal surrogate to estimate tumour motion. However, the liver is a deformable organ that moves in a complex, oval-shaped pattern, and the motion of the liver dome does not necessarily reflect the motion in all directions of the tumour itself. These uncertainties in motion assessment and target localisation are often compensated for by applying larger safety margins to ensure adequate target coverage, but this may lead to increased radiation dose to surrounding healthy tissues and potentially higher toxicity.

#### 2.2.3.2 Role of MRI in radiotherapy

##### 2.2.3.2.1 Basic MRI physics

The principles of MRI are based on the interactions between a strong magnetic field and hydrogen nuclei (proton) inside the body to generate detailed images of internal structures. While the physics of MRI is complex and covered in detail in many textbooks [49, 50], this section provide a simplified overview of the fundamental concepts.

The hydrogen nucleus (a single proton) produces measurable effects equivalent to a tiny magnetic field, known as the magnetic moment. In the absence of an external magnetic field, the proton spins are randomly oriented, resulting in no net magnetisation. When placed in a strong magnetic field ($B_0$), the proton spins begin to precess around field direction, but on average a slightly greater fraction are found aligned with $B_0$. The sum of these spins creates the net magnetisation vector (NMV), which is aligned with $B_0$. Each proton also precesses around $B_0$ at a specific frequency called the Larmor frequency ($\omega = \gamma.B_0$). To generate a measurable signal, a radiofrequency (RF) pulse is applied by the RF transmit coil, flipping the NMV away from its alignment with $B_0$ and creating transverse magnetisation (Mxy). As Mxy

precesses in phase, it induces a voltage in the RF receiver coil, forming the detectable NMR signal. Once the RF pulse ends, the transverse magnetisation relaxes and returns gradually to its equilibrium longitudinal alignment (Mz).

There are two main types of relaxation in MRI: (1) longitudinal relaxation (T1 recovery) and (2) transverse relaxation (T2 & T2* decay). T1 relaxation refers to the realignment of proton spins with the main magnetic field ($B_0$) as they release energy to their molecular surroundings. T2 relaxation, on the other hand, describes the loss of phase coherence among spinning protons in the transverse plane due to interactions between neighbouring spins T2 decay can be natural T2 or effective T2*, where measured field inhomogeneities will increase the relaxation rate. An MR signal is only detected when spins are in phase within the transverse magnetisation. Both T1 and T2 relaxation follow exponential processes: T1 is defined as the time it takes for 63% of the longitudinal magnetisation to recover, while T2 is the time at which 63% of the transverse magnetisation has decayed, (37% remaining of the original signal). The rate of this recovery or decay is tissue dependent and influenced by factors such as molecular size, tumbling rate, composition, and structural complexity. These differences cause the image contrast. T1 is also affected by the field strength.

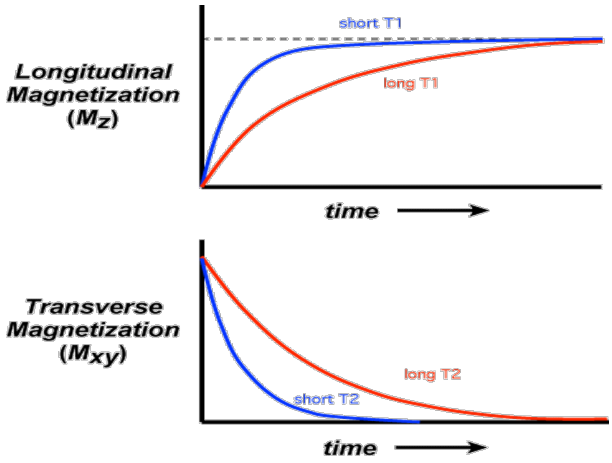


**Figure 2.3: An illustration of T1 and T2 relaxation in MRI. The top graph shows longitudinal recovery (T1), and the bottom shows transverse decay (T2) for tissues with short (blue) and long (red) relaxation times, demonstrating their role in image contrast. Figure replicated from [51].**

Two timing parameters are used in the acquisition of MRI signals: repetition time (TR) and echo time (TE), which play a critical role in image

contrast. TR refers to the time interval between successive RF excitation pulses, and TE is the time between an RF pulse and the peak of the detected echo signal. These parameters control the extent to which T1 and T2 relaxation contribute to signal intensity as illustrated in Figure 2.3. Adjusting TR and TE allows for contrast manipulation between different tissues based on their relaxation characteristics. For example, a sequence with a short TR and short TE enhances T1 contrast, producing T1-weighted (T1w) images. Conversely, using a long TR and long TE enhances T2 contrast, resulting in T2-weighted (T2w) images.

After RF excitation creates transverse magnetisation, precessing spins induce a tiny voltage in dedicated receive coils but rapidly dephase, so the magnetisation must be refocused to measure a signal. This is achieved through pulse-sequences such as spin-echo sequences and gradient-echo sequences. Understanding these sequences and their key parameters helps optimise MRI protocols to meet radiotherapy requirements.

Gradient encoding is a key concept in MRI, used to locate MR signals detected by the receiver coil by slightly altering the main magnetic field ($B_0$). These variations shift the resonance frequency of protons based on their location along the x, y, and z axes, allowing the MR signal to be spatially encoded. MRI images are formed by collecting raw data in k-space (spatial frequencies). Once k-space is filled, a Fourier transform is applied to convert the frequency data into spatially encoded data that can be displayed as an image.

In MRI, both two-dimensional (2D) and three-dimensional (3D) acquisition techniques are commonly used. In 2D MRI acquisition, data are collected on a slice-by-slice basis with a defined slice thickness. This allows shorter acquisition times and reduced sensitivity to patient motion. However, 2D is limited by slice thickness, which can reduce through-plane resolution and introduce artefacts when images are reformatted. In contrast, 3D MRI data are collected from the entire imaging volume, allowing reconstruction of very thin slices. This will improve signal to noise ratio (SNR), excellent spatial resolution, high-quality multiplanar views. However, 3D MRI typically longer acquisitions and more sensitive to patients motion unless accelerated.

#### 2.2.3.2.2 MRI simulation

Using MRI in radiotherapy requires careful consideration. Guidelines and recommendations for the use of MRI in radiotherapy from multiple groups have been reported in the literature [52, 53]. Dedicated MRI simulators are being adopted more widely in radiotherapy [54-56], supporting the importance of MRI in the radiotherapy workflow. Figure 2.4 shows an example of a Philips MRI simulator. This system includes key features commonly found in CT simulators, such as an external laser positioning system and an indexable flat tabletop. It is also equipped with MRI coils appropriate for radiotherapy use and anterior coil bridge/support, which hold the coil off the patient to prevent the coil from compressing or deforming the anatomy. A potential concern when using MRI in radiotherapy is its susceptibility to geometric distortions, which can compromise geometric accuracy. These distortions originate from both scanner-related and patient-related sources [52]. Scanner-related distortions are caused by static magnetic field inhomogeneities, gradient field non-linearities, and eddy currents. These distortions are minimal at the isocentre but increase towards the edges of the field of view (FOV). There are different strategies to minimise distortions, including shimming distortion correction software and optimising sequences differently compared to diagnostic purposes [52]. Patient-related distortions arise from magnetic susceptibility differences between different tissues such as air-tissue boundaries or near metallic implants, which can cause shifts in resonance frequency and signal loss or image distortion [52]. Another cause of distortion is chemical shift which can be seen at the interface of water and fat tissue. These effects can be reduced by applying shimming and adjusting the receiver bandwidth [52]. While increasing bandwidth reduces chemical shift distortions, it may also introduce greater image noise, potentially affecting overall image quality.

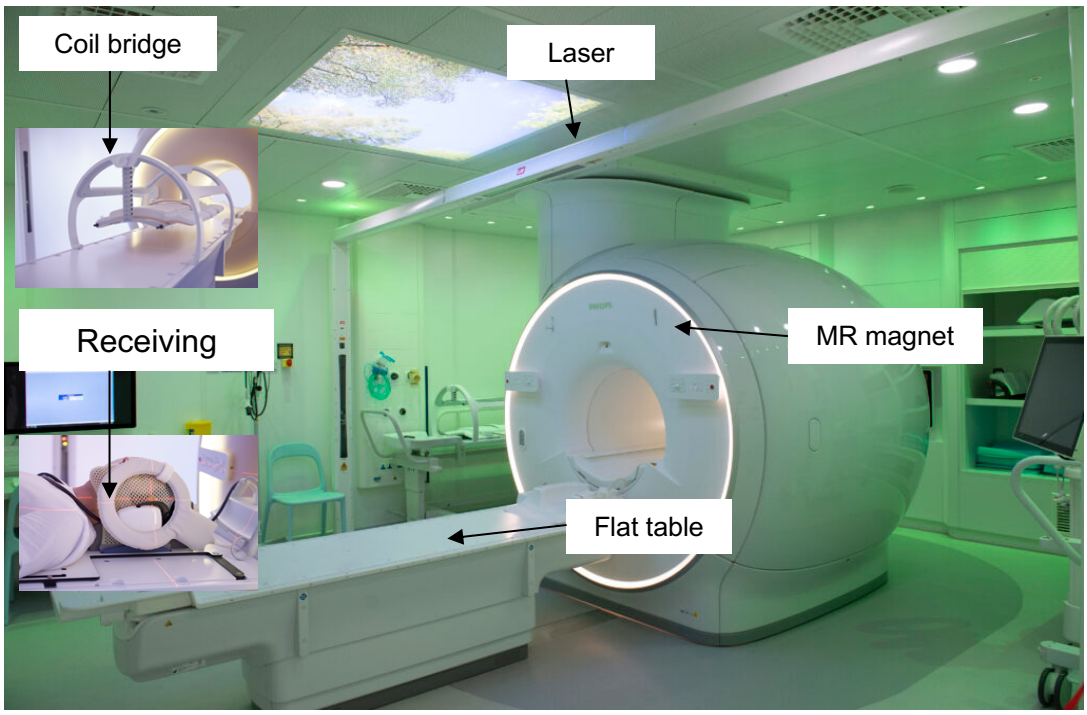


**Figure 2.4: Philips Ingenia 1.5T MR-RT dedicated MR simulator scanner with flat tabletop and external laser positioning system, located at St James's Hospital, Leeds Teaching Hospitals NHS Trust, replicated from [37].**

#### 2.2.3.2.3 MRI Sequences for target delineation

The choice of MRI sequences is essential for achieving accurate delineation of target volumes. For liver SABR at LCC, patients were scanned on a flat couch top with a coil bridge on a 1.5 T Siemens diagnostic MRI using a 3D T1-weighted VIBE (volumetric interpolated breath-hold examination) sequence with fat saturation. VIBE is a fast gradient-echo MRI sequence, ideal for capturing dynamic contrast-enhanced liver images within a single ~17-second breath-hold. It enables visualisation of arterial, venous, and delayed phases following the injection of the liver-specific contrast agent Primovist, which is actively taken up by hepatocytes. This MRI sequence was used to acquire the liver MR dataset presented in Chapter 4. Similarly, a 3D T1w Dixon sequence often combined with a gradient-echo for faster acquisition is widely used in liver imaging. This sequence acquires images at multiple echo times and combines them to create fat-only and water-only images. It produces four image contrasts (in-phase, out-of-phase, water-only, and fat-only) in a single acquisition.

For brain radiotherapy, the standard imaging sequences for delineation include T1w post-contrast, which highlights residual or enhancing tumour tissue, and T2w fluid attenuated inversion recovery (FLAIR), which helps differentiate oedema from non-enhancing tumour [57].

#### 2.2.3.2.4 MRI in liver and brain radiotherapy

The success of radiotherapy treatment planning and delivery relies heavily on accurate visualisation and localisation of both tumours and surrounding healthy structures, aiming for adequate tumour coverage while sparing nearby OARs. Poorly defined target volumes can lead to a geographic miss, which may compromise local tumour control and negatively impact patient survival [58, 59]. Similarly, overestimating margins may expose surrounding healthy tissues to unnecessary radiation and may increase the risk of toxicity [58, 59]. CT remains the most widely used imaging modality. It is widely accessible, provides high spatial resolution and geometric accuracy, and produces reproducible images along with electron density information essential for dose calculation. Despite its advantages, CT provides suboptimal imaging for delineating many tumour sites due to its limited soft tissue contrast, which can result in underestimation of the target in complex regions such as the brain and liver [60-62]. This poor contrast makes it harder to clearly define tumour boundaries, often leading to larger safety margins that may compromise target coverage and may increase the risk of toxicity to surrounding healthy tissues.

In contrast, MRI offers superior soft tissue characterisation and has become the imaging complement to CT in radiotherapy planning [57, 63]. MRI has been shown to reduce interobserver variability in target volume definition compared to CT in brain and liver tumours [60, 61, 64-66]. Moreover, the use of MRI not only improves anatomical detail but also has the potential to provide functional information [67-69]. MRI supports functional and quantitative imaging through biomarkers such as diffusion and perfusion sequences, which are increasingly being explored for adaptive radiotherapy and personalised treatment [67-69].

### 2.2.3.3 CT to MRI image registration

In the current CT-MRI workflow, target delineation is typically performed on MRI and then transferred to the CT by spatially aligning the two image sets

using image registration. Image registration is defined as the process of transferring anatomical points from the floating image (MRI) onto the reference image (CT) [70, 71]. Image registration can be performed using rigid (RIR) or affine and deformable (DIR) methods. The AAPM report Task Group No. 132 [70, 71] define the following:

- Rigid registration — a registration where the transformation preserves the distance between all points in the image. A rigid registration can include translation in all directions as well as rotations in all directions.
- Affine registration — a registration that includes the transformations from rigid registration and adds the additional transformations of scaling, shearing, and plane reflection. The distance between all points is not maintained, as in rigid registration, however parallel lines remain parallel after the transformation.
- Deformable registration — a registration transformation can also be spatially variant where the number of degrees of freedom can be as large as three times the number of voxels in the source dataset (e.g., a unique displacement vector for every voxel in the source dataset).

In radiotherapy, the most common registration methods used in clinical practice are RIR and DIR. RIR allows for translations and rotations in six degrees of freedom, assuming that the anatomy remains unchanged in shape or size, making it suitable for regions with minimal anatomical variation, such as the brain [70, 71]. In contrast, DIR allows non-rigid transformations, including scaling and shearing, in addition to translations and rotations [70, 71]. This added flexibility makes it useful for deformed organs, such as the liver, where internal organs may shift or change shape between scans. Each method has its advantages and limitations. RIR maintain geometric fidelity and anatomical accuracy, as it does not alter internal spatial information between scans [70, 71]. However, it is limited when the size, shape, or orientation of structures differs between the CT and MRI [70, 71]. DIR offers the flexibility to correct such misalignments but it may introduce deformations that do not accurately represent the patient's true anatomy if not properly validated, since no ground truth exists to confirm anatomical accuracy [70, 71]. The accuracy of image registration depends on several factors, including image acquisition parameters,

image quality, the time between scans, and consistency in patient positioning. Accurate image registration can be challenging, particularly due to respiratory motion. At LCC, rigid registration is commonly used for liver and brain registration, involving automatic alignment followed by manual registration in regions of interest. Image registration between CT and MRI is inherently imperfect due to multiple factors explained. As a result, residual errors may still occur, making it essential to assess registration quality to ensure it is clinically acceptable [52, 70, 71].

#### 2.2.3.4 Target volume and OAR delineation

After acquiring the CT and MRI simulations, the clinician can begin delineation process to the target volume and surrounding OARs. OARs are healthy tissues or organs located near the tumour that are sensitive to radiation and at risk of toxicity due to their presence within high-dose regions; therefore, the prescribed dose need to be optimised to reduce the risk of damage [72]. Typical OARs for liver and brain radiotherapy are summarised in Table 2.1. In brain and liver radiotherapy, MRI is commonly used to contour the tumour volume due to its superior soft tissue contrast, while OARs are typically delineated on CT, which serves as the planning image for dose calculation. In current workflows, tumours delineated on MRI are transferred to the planning CT dataset through image registration. Since MRI and CT are acquired in separately, patient-related motion between scans may introduce systematic uncertainties. Therefore, aligning all contours within the same frame of reference as the planning CT is essential for accurate dose delivery and consistent treatment planning.

**Table 2.1: Summary of organ at risk (OAR) delineated in liver and brain radiotherapy.**

| | |
|---|---|
| **Liver** | Liver (non-tumor), duodenum, stomach, small bowel, kidneys, spinal cord, chest wall, heart |
| **Brain** | Brainstem, optic nerves, optic chiasm, orbits, lenses, cochleae, hippocampi, pituitary gland |

Radiotherapy target volumes are defined according to established clinical in ICRU guidelines [73]. An illustration of the differences in target delineation between liver and brain tumours is shown in Figure 2.5. The gross tumour

volume (GTV) represents the clinically visible tumour. However, since most tumours spread microscopically beyond the visible lesion, the GTV is typically expanded to form the clinical target volume (CTV). For liver tumours, asymmetric margins are added to the CTV to create the internal target volume (ITV). This accounts for physiological motion, such as respiratory movement and organ filling, which cannot be assessed directly using 4D CT imaging. The last margin, known as the planning target volume (PTV), is used to compensate for all remaining uncertainties, including geometric variations, patient setup errors, and contouring inaccuracies. According to the LCC clinical protocol, in liver radiotherapy the ITV is expanded with a 5 mm margin to create the PTV. In brain radiotherapy, where internal motion is negligible, the CTV is expanded with a 4–5 mm margin to create the PTV [74].

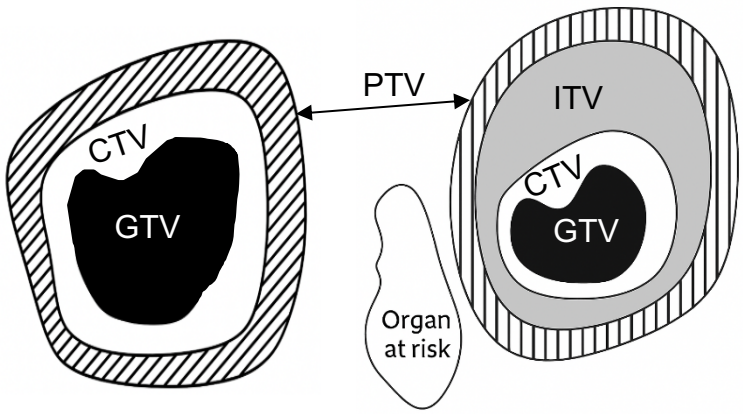


**Figure 2.5: Graphical representation of the volume margins, as defined by the ICRU reports. PTV = planning target volume, ITV = internal target volume, CTV = clinical target volume and GTV = gross target volume. Margins for brain tumours (Left), margins for liver tumours (Right).**

#### 2.2.3.5 The motivation of 4D MRI

To estimate the uncertainties arising from respiratory motion, an accurate definition of the ITV is essential in liver radiotherapy, ensuring adequate tumour coverage while minimising radiation to surrounding OAR. Current radiotherapy pathways for liver tumours rely on 4D CT for ITV delineation, but this approach is limited as discussed previously. Most liver tumours are poorly visualised or invisible on CT. Therefore, clinicians rely on visible landmark to define CTV to ITV margins such as the displacement of the liver dome rather than direct

tumour tracking. This uncertainty leads to the use of large margins to ensure coverage, which potentially increases radiation dose to normal liver tissue and surrounding OARs [75]. The motivation for using 4D MRI arises from this limitation. MRI provides excellent soft-tissue contrast for liver tumours, capturing realistic motion throughout the respiratory cycle and allowing for more accurate and personalised ITV definition [76, 77]. 4D MRI has the potential to reduce margins, spare healthy tissue, and improve treatment precision [78, 79]. Chapter 3 presents a systematic review of 4D MRI techniques applied in abdominal radiotherapy. It summarises the proposed methodologies, their clinical validation in patient studies, and highlights key findings reported in the literature.

### 2.2.4 Treatment planning

Radiotherapy treatment planning is an essential stage of modern radiotherapy, aiming to deliver the prescribed radiation dose accurately to the target while minimising exposure to surrounding healthy tissues. This is achieved by shaping the radiation beams so that the high-dose region conforms to the target volume as much as possible [80]. Treatment planning relies on CT images, precise contouring, optimised dose calculations, and advanced delivery methods to achieve high treatment accuracy [80]. The planning techniques have evolved over the past decades, from three-dimensional conformal radiotherapy (3D CRT) planning to intensity-modulated radiotherapy (IMRT) and volumetric-modulated arc therapy (VMAT) planning [80]. 3D CRT shapes radiation beams to match the 3D geometry of the tumour. It uses fixed-intensity beams delivered from multiple angles to ensure the dose conforms closely to the tumour shape while minimising exposure to surrounding healthy tissues. Unlike 3D CRT, IMRT and VMAT offer more flexibility. They use inverse planning, which means the planner specifies the dose objectives for targets and constraints for OARs. The plan is optimised by modifying radiation intensity, the multi-leaf collimator (MLC) positions and the monitor units delivered. VMAT has additional advantages over IMRT. It delivers radiation in a continuous arc from multiple angles as the gantry rotates around the patient, with variable dose rate, beam shape, and speed. This allows for highly conformal dose distributions, better sparing of surrounding OAR, and shorter treatment time [81]. VMAT is a

preferred option for complex cases such as brain and liver SABR, due to its high precision, dose conformity, and sparing OAR [82-84].

Treatment planning and dose calculation are performed using a computerised treatment planning system (TPS), such as RayStation (RaySearch), Eclipse (Varian), and Monaco (Elekta). These systems use different dose calculation algorithms to model how radiation interacts with tissues and to accurately predict the dose distribution delivered to the patient. Accurate dose calculation relies on information about the electron density of tissues, which can be obtained from CT scans. A calibration curve that maps HU values to electron density is developed during commissioning procedure of the CT scanner. The process involves scanning a phantom with a variety of known electron densities and comparing those to the HU measured from the scanner to generate the curve.

To evaluate the plan produced, one of the key outputs of TPS is the dose volume histogram (DVH), a graphical representation that summarises the dose distribution within a volume of interest, used to evaluate whether clinical objectives and safety margins have been met for both target and normal tissues [80]. Once the treatment plan is approved by the clinician, all necessary data is transferred electronically to treatment machine.

### 2.2.5 Treatment delivery

IGRT has revolutionised radiotherapy over the past decades by enabling more accurate and precise treatment delivery [85-87]. IGRT uses medical imaging integrated into the treatment machine (linac) to provide detailed and accurate information about the patient's anatomy at the time of treatment. It accounts for daily changes in patient anatomy, enables visualisation of the tumour and surrounding OARs, and ensures the patient’s position matches the planning CT scan before radiation is delivered. This helps reduce setup errors before each treatment session and ensures accurate delivery of the planned dose to the intended target while sparing nearby healthy tissues. Among the various imaging systems developed, CBCT is the most widely used in current clinical practice. One commonly used system is X-ray volume imaging (XVI) (Elekta AB, Stockholm, Sweden), as shown in Figure 2.6. Unlike conventional CT scans, the CBCT system uses a cone-shaped X-ray beam and a flat-panel detector to capture images of the patient from multiple projection angles,

allowing reconstruction of 3D or 4D images in a single rotation. However, compared to CT, it has lower image quality due to increased scatter radiation, and reduced soft-tissue contrast .

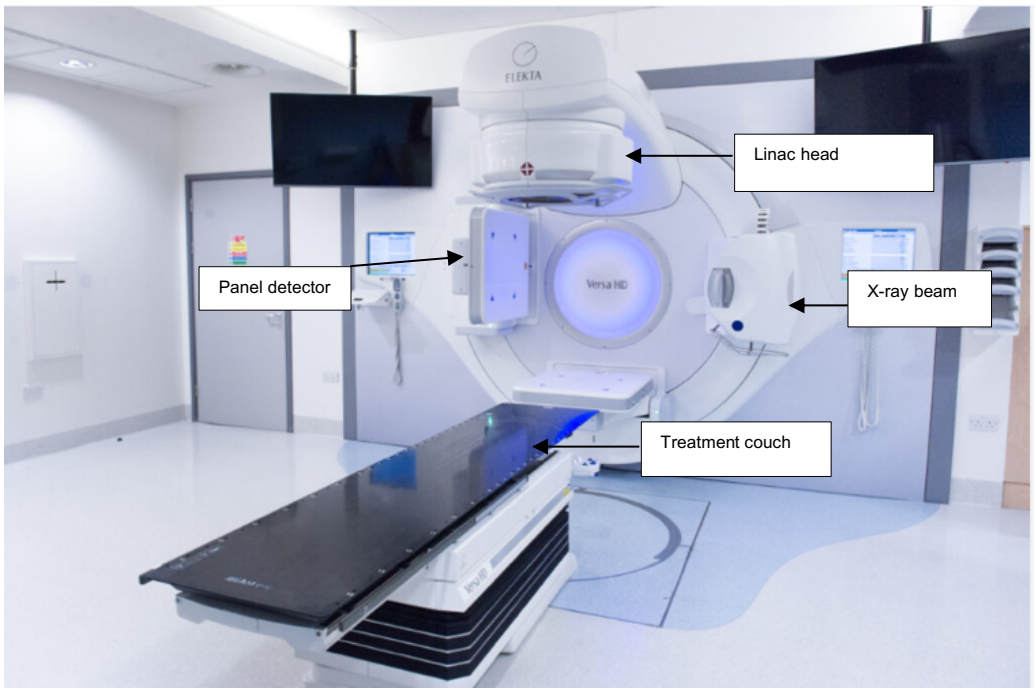


**Figure 2.6: Elekta linear accelerator system, showing key components including the linac head, cone-beam CT (CBCT) unit, and treatment couch, which is used for external beam radiotherapy, replicated from [37].**

3D CBCT is suitable for imaging fixed and less complex anatomical sites, such as the brain. However, its use is limited for treatment sites affected by respiratory motion, as it does not capture changes in tumour shift due to breathing. 4D CBCT is similar to 4D CT, acquires a large number of projections over a slow scan [88]. These projections are sorted into respiratory phase bins, and reconstructed into 3D images representing different phases of the breathing cycle. This requires a breathing trace obtained from a bellows placed over the patient. This enables the evaluation of tumour position at each phase, allowing verification that the patient's breathing amplitude remains within planned limits. Elekta XVI system can acquire a full-fan 4D CBCT scan in approximately 3 to 4 minutes, whereas a 3D CBCT scan takes up to one minute [88]. In the liver, however, 4D CBCT presents specific challenges due to its poor soft tissue contrast. As a result, the entire liver volume is often used as a surrogate for patient setup verification. Other options have been investigated, such as lipiodol deposits or implanted fiducial markers, as direct surrogates to improve

localisation accuracy [88]. Although CBCT typically offers lower soft tissue contrast and higher image noise, and is more prone to artefacts from patient motion or metal objects compared to conventional CT scan, its image quality is optimised to allow accurate alignment with the planning CT for patient setup verification [89].

Before treatment begins, the patient is positioned in the same position as in CT and MRI simulation using same immobilisation devices. A CBCT scan is then acquired and rigidly registered to the planning CT, which is considered to be the reference image for patient setup verification. At LCC, the Elekta XVI system is used to verify and adjust the patient's position before treatment by aligning the daily CBCT with the planning CT. This process accounts for anatomical changes and setup variations, ensuing that the radiation is accurately delivered to the planned target volume while minimising exposure to nearby OARs. Rigid registration between the reference image and CBCT can be performed using up to six degrees of freedom, including translational (left–right, superior–inferior, anterior–posterior) and rotational (pitch, roll, yaw) movements. However, in our current clinical practice, rotational corrections are not applied for liver and brain. In LCC's clinical protocol for brain radiotherapy, 3D CBCT is used for patient position verification during the first three treatment sessions. If a systematic setup difference is observed, a correction is applied and verified on the fourth session. Weekly imaging is then performed. Additional scans can be acquired if any concerns arise. This allows for on-line correction before treatment delivery, while setup errors from the initial sessions are used for off-line correction in the remaining fraction directly without imaging [90]. This approach provides an adequate assessment of setup accuracy while minimising workload, because the head is relatively fixed organ and is not subject to significant internal motion compared with other treatment sites.

Liver SABR is more complicated to treat and so requires daily imaging verification. A minimum of three 4D CBCT scans are required for daily positioning verification to account for internal motion caused by respiration or organ movement. Two liver contours are provided on the CT reference for matching: the liver max-exhale and the liver max-inhale. Initially, the liver max-exhale contour is matched with the 4D CBCT max-exhale phase. This is followed by a second check to match the liver max-inhale contour with the 4D

CBCT max-inhale phase. Ideally, the superior/inferior liver motion should closely align with these contours for accurate matching. The clinical workflow begins with a 4D CBCT scan for setup verification, using automatic matching to assess bony alignment and rotation. Necessary corrections are made under the supervision of medical physicist. A manual match then focuses on the tumour and OARs. The patient is then moved based on this registration to the correct treatment position, and a second 4D CBCT scan is acquired for post-correction verification to ensure accurate alignment.

If positioning errors are ≤2 mm, treatment proceeds; otherwise, a rescan is performed. A final 4D CBCT scan is used for post-treatment verification, essentially to ensure the patient didn't move during treatment. If any movement is detected, the dosimetric consequences on the OARs are evaluated to determine whether the treatment plan needs adjustment for the remaining fractions. For brain and liver SABR, the setup error tolerance is no greater than 3 mm and 2 mm, respectively, while any excessive rotation should be evaluated by the multidisciplinary team. In some cases, a new treatment planning CT may be required if the patient's anatomy in the treatment region has changed significantly since the original planning CT. Due to factors such as weight gain or loss, tumour progression or shrinkage, or internal anatomical changes like bowel gas or organ motion.

## 2.3 MRI-only radiotherapy

### 2.3.1 Motivation and Challenges

The role of MRI in radiotherapy has been growing, transitioning from a complementary role used with CT for target delineation to becoming the sole imaging modality in MRI-only radiotherapy [91, 92]. As discussed in the previous section (2.2.2.2.4), one of the primary advantages is MRI's superior soft tissue contrast, which allows for accurate target delineation. Furthermore, the potential benefits of removing CT from the radiotherapy workflow have also been discussed in the literature. One major advantage is the elimination of CT-MRI image registration, which can introduce systematic errors that persist throughout the treatments. These errors may be caused by differences between CT and MRI scans acquired at different times, including variations in patient positioning, anatomical changes, or inherent inaccuracies. Co-registration errors

have been reported of approximately 2 mm [93] in the brain and up to 5 mm [94] in the liver. Image registration uncertainties may compromise the accuracy of target delineation, often requiring larger margins. This effect is particularly critical in SABR, which typically requires small margins, commonly limited to 1 mm [17]. Using a single imaging modality reduces hospital visits and burden of appointments, improving patient experience while also simplifying the clinical workflow for both clinicians and patients. Tyagi et al. reported that MRI-only workflows in prostate can save approximately 15 minutes compared to the current workflow [95]. Additional time savings may also be achieved, as target delineation is performed directly on the MR images, eliminating the need for image registration process. Reducing overall costs is another advantage of MRI-only workflows by eliminating the need for additional CT imaging and its associated resource requirements [96]. The calculated financial saving for MR-only radiotherapy compared to a MR-CT workflow can vary between institutions. For example, a study by Korhonen et al. at a public hospital in Helsinki found that MRI-only radiotherapy in the prostate can be more cost-effective by eliminating the need for CT simulation [97]. However, the additional cost of quality assurance (QA) should be considered when implementing an MRI-only workflow [96]. Lastly, an MRI-only workflow eliminates unnecessary exposure to ionising radiation. However, this benefit may be questioned, as the radiation dose from modern, high-quality CT scanners is relatively low compared to the therapeutic doses used in radiotherapy. Although the dose from CT is relatively low, careful consideration is required when 4D CT need to be repeated due to image artefacts or issues that impact clinical decision-making. In contrast, 4D MRI provides a non-ionising imaging alternative with excellent soft tissue contrast, making it valuable in MRI-only radiotherapy for the liver, where repeated imaging may be required. However, Philips still offers no commercial 4D MRI solution; this thesis provides a step towards that direction to facilitate future research. It is essential to develop 4D MRI technologies that align with the standard requirements for MRI use in radiotherapy. In general, the potential benefits of MRI-only radiotherapy are important and require further investigation in treatment sites such as the brain and liver. These advantages were not addressed within the scope of this thesis.

A key challenge in implementing MRI-only workflows is that MRI does not inherently provide electron density information, which is essential for

accurate dose calculation. Unlike CT, which provide a direct relationship between image intensity and tissue density, MRI signals are based on proton relaxation properties and do not reflect electron density. To address this limitation, several techniques have been developed to generate images with CT properties, known as sCT, from MRI data. These methods include bulk density, atlas-based, voxel based approaches, and more recently, deep learning models capable of predicting continuous HU-based electron density maps with high accuracy [98-101]. Another issue of MRI only is the requirement to generate a reference CT for CBCT verification on the treatment machine. The ability to generate reliable sCT images is essential to ensure that MRI-only planning provides dosimetric accuracy and patient positioning verification comparable to a conventional CT scan.

### 2.3.2 Synthetic-CT generation

#### 2.3.2.1 Bulk density methods

Bulk density assignment is the earliest and most straightforward method for generating sCT images in MRI-only radiotherapy [99, 100]. In this method, individual structures are segmented and assigned a fixed bulk density (HU) value. One of its forms assigns a single water-equivalent HU value to the entire patient volume, assuming homogeneous tissue density. However, a major limitation is the absence of bone anatomy, which restricts its use for patient setup verification. An alternative approach is to manually segment key anatomical structures such as bone, soft tissue, and air, directly on MRI and assign each a predefined electron density value. In some studies, these structures were initially contoured on CT and then transferred to MRI for density overriding; however, this is not feasible in true MRI-only workflows. The primary advantages of this method are its simplicity and low computational requirements. Nevertheless, it has several limitations: manual segmentation is time-consuming and operator-dependent, and standard MRI sequences do not clearly visualise short T2* structures like cortical bone, which can compromise accuracy. Additionally, the method does not account for tissue heterogeneity, making it less suitable for anatomically complex regions. Despite these limitations, bulk density method has been evaluated in multiple studies for the brain [100]. The first commercial solutions adopted this technique for MRI-only radiotherapy, such as early versions of Philips prostate MRCAT (MR for

calculating attenuation, Philips Healthcare) [102], or in Siemens syngo.via (syngo.via software platform, Siemens Healthineers), integrated with atlas-based methods to enhance bone delineation [103].

#### 2.3.2.2 Atlas-based Method

Atlas-based methods are the next approach that was widely studied for generating sCT images in MRI-only radiotherapy, offering more advantages compared to bulk density-based methods [99, 100]. This technique relies on co-registered pairs of MRI and CT images, called an "atlas", using either a single atlas or, a multi-atlas. A new MRI scan is deformably registered to the MRI atlas data, and the same transformation is applied to the CT images to estimate the sCT that closely matches the anatomy of the new patient. This method is considered practical for clinical use, typically using a single standard MRI, which minimise scan time. Additional advantages include automatic contouring, the ability to generate reference images (e.g. CBCT-based image registration) for patient positioning, and robustness to MRI artefacts. However, their accuracy relies heavily on the quality and anatomical similarity of the atlas to the target patient. Challenges such as anatomical abnormalities and bone segmentation may require manual adjustments and can reduce accuracy. Atlas-based methods have been evaluated for brain [104, 105] and also applied in combination with a voxel-based approach in abdomen [106-108].

#### 2.3.2.3 Voxel-based methods

Voxel-based methods are another technique for generating sCT images, and they offer improved anatomical accuracy for individual patients compared to previous methods [99, 100]. This method relies on MRI voxel intensities to assign HUs, enabling tissue density estimation directly from the MRI data using statistical models. Voxel-based methods can utilise either standard or specialised MRI sequences such as ultra-short echo time (UTE) imaging or both. When using standard sequences, distinguishing between bone and air remains difficult, often requiring manual bone delineation, which is time-consuming and impractical in clinical settings. Additionally, using multiple MRI sequences to improve tissue classification increases scanning time and the risk of patient motion between acquisitions. UTE sequences allow better imaging of cortical bone due to its short T2* relaxation time, but they have been used only in brain and are not routinely included in clinical MRI protocols [99, 100].

#### 2.3.2.4 Deep learning based Methods

Deep learning methods represent the most advanced and robust methods of sCT generation techniques for MRI-only radiotherapy [98, 101, 109]. These methods are the most commonly used in commercial systems. Since deep learning was first introduced for sCT generation in brain [110], it has rapidly evolved into a key method for MRI-only radiotherapy. As a subset of machine learning and artificial intelligence (AI), deep learning uses neural networks, most commonly convolutional neural networks (CNNs) or generative adversarial networks (GANs), trained on paired CT and MRI data, to learn a mapping between MRI signal intensities and corresponding CT Hounsfield Units to generate sCT images**.** CNN consists of input and output nodes connected through multiple hidden layers, where each connection learns specific parameters during training. One common architecture is the U-Net, which features an encoder–decoder structure with skip connections that help extract and reconstruct MR image features. GAN consists of two components: a generator and a discriminator. The generator creates sCT images, while the discriminator evaluates whether an image is real (from actual CT data) or fake (generated). The training process is considered optimal when the discriminator can no longer distinguish between real and generated images. Several variants of GANs have been developed. Conditional GANs require paired MRI and CT data, aligned through rigid or deformable image registration. In contrast, CycleGANs consist of two generators and two discriminators and do not require paired data; instead, they learn the mapping between the two modalities using unpaired MRI and CT datasets. Deep learning models can generate reliable and accurate sCTs within seconds, making them highly efficient for clinical workflows. However, they often require accurate image registration of MRI and CT training data, large datasets, and are sensitive to data quality. Their generalisability is limited, as performance depends on the characteristics of the training data, and they are also associated with high computational demand [111] .

#### 2.3.2.5 Liver MRI-only radiotherapy

A recent review reported that 58% of studies on sCT generation have focused on the brain, while only 2.9% addressed the abdomen [109]. Unlike the

brain, generating accurate sCTs for the liver poses additional challenges. These include motion artefacts that reduce image quality, CT-MRI misregistration due to differences in breath-hold, and variable air content in abdominal organs. Most previous studies generating sCT based on DL in the liver have developed local research-based algorithms [112-120], and currently, no commercial solution is available. Chapter 4 evaluates sCT generation for liver radiotherapy using a DL training platform provided by a commercial company (RayStation Laboratories), with potential for clinical implementation. This model is not MRI vendor specific and can be accessed directly within a treatment planning system, making it broadly available in radiotherapy centres. This DL model is inspired from CycleGAN architecture, which include both paired and unpaired data for training. This method, first introduced for brain sCT generation [121], combines paired and unpaired training to reduce the misalignment issues of unpaired training while also addressing the registration errors and blurriness associated with paired training, thereby enhancing robustness in abdominal sCT generation. Compared to previous studies that evaluated sCT DL models for the liver [112-120], none of them performed a full assessment of MRI-only workflows in terms of image similarity, dosimetric evaluation, and position verification using 4D CBCT as the clinical routine practice. They mainly focused on image similarity and dosimetric analysis [112-120]. Chapter 4 makes a significant contribution to the literature by presenting the first comprehensive evaluation of both dosimetric and positioning accuracy of sCT generation for the liver in a single study.

#### 2.3.2.6 Brain MRI-only radiotherapy

For brain MRI-only radiotherapy, sCT generation has progressed from a research-based approach to a commercially available solution, making it ready for clinical implementation. Currently, four AI-based commercial solutions for sCT generation are available for clinical use, all of which have received CE marking or FDA approval. An overview of the commercially available solutions is provided in Table 2.2. In this thesis, the MRCAT (Philips) system was used.

**Table 2.2: Overview of commercially available synthetic CT generation solutions for brain MRI-only radiotherapy.** *Abbreviation: convolutional neural networks (CNN); conditional GANs (cGAN); Cycle-Consistent GANs; (CycleGAN) and Gadolinium contrast (Gd).*

| Product | Company | sCT method | MRI vendor availability | MRI-sequence | Clinical validation studies |
|---|---|---|---|---|---|
| **MRCAT** | Philips Healthcare, Netherland | CNN | Philips only | T1 Dixon | [122-125] |
| **Syngo.via RT** | Siemens Healthcare, Germany | cGAN | Siemens only | T1 Dixon | [126, 127] |
| **MRI Planner** | Spectronic, Medical, Sweden | CNN | Not vendor specific | T1 Dixon | [126, 128] |
| **MR-box by ART-plan** | Therapanacea, France | cycleGAN | | T1 + Gd | [126] |

Four studies have been identified that evaluated the MRCAT solution for clinical validation and implementation [122-125]. The first group implemented MRI-only brain radiotherapy using MRCAT and developed a local QA protocol and local consensus recommendations on contouring and image QA criteria to support clinical implementation [122, 123]. Their clinical implementation included two cohorts: 30 patients for commissioning and 30 for validation. However, these studies did not include a quantitative assessment of CBCT-based patient positioning. Another group [124], clinically validated MRCAT retrospectively for dosimetric and patient positioning in only 20 patients; however, they used TPS rather than positioning software system (such as XVI). Similarly, another study evaluated only dosimetric accuracy in a cohort of 18

patients; however, positioning accuracy was not evaluated [125]. Chapter 5 of this thesis addresses the limited clinical validation of patient positioning by using clinical positioning software (Elekta XVI system) replicates the standard workflow used in brain radiotherapy. A larger patient cohort of 93 was used compared to previous studies in the literature, allowing for a more robust evaluation of both dosimetric and positioning accuracy.

#### 2.3.2.7 sCT validation methods

The validation methods used to assess sCT image quality are presented, focusing on the most commonly used metrics for image similarity, dosimetric, and patient positioning evaluations discussed in the literature. In all evaluations, sCT images were compared against CT images, which were considered the ground truth. These validation methods represent a critical part of the commissioning and clinical implementation of MRI-only radiotherapy, ensuring that sCT images meet the required standards. Several quantitative metrics for evaluating sCT quality have been reported in the literature [98, 101].

##### 2.3.2.7.1 Image similarity evaluation

The first step in evaluating sCT image quality is to assess the accuracy of HU values compared to the corresponding CT. This is commonly done using HU analysis such as mean absolute error (MAE) [98, 100, 101], which quantifies the mean absolute differences in HU values on a voxel-by-voxel basis between the two images and provides a straightforward measure of overall HU accuracy. The MAE is calculated according to following equation1:

$$MAE = \frac{1}{N}\sum_{i=1}^{N}|sCT_i - CT_i| \qquad \text{Equation (1)}$$

where N is the number of voxels, CT is HU value at voxel i in the planning CT, and $sCT_i$ is the corresponding HU value in the synthetic-CT.

MAE is not always suitable for all cases. For example, the liver's heterogeneous structure and the presence of variable abdominal gas in the bowel region, can skew HU values due to anatomical differences between MRI and CT [100]. Furthermore, MAE does not necessarily reflect clinical impact, as VMAT delivers radiation from multiple angles, averaging out local HU discrepancies during dose calculation. Errors captured by MAE may also occur outside high-dose regions and thus have minimal dosimetric relevance.

Additionally, even minor misregistration between sCT and CT may bias MAE results [111].

#### 2.3.2.7.2 Dosimetric evaluation

Dose distributions calculated on the sCT can be compared to the planning CT to assess differences in target coverage and OAR. By registering the sCT and planning CT, the same plan can be calculated on both images for a direct comparison. Commonly used evaluation metrics include DVH analysis and gamma analysis [98, 101]. DVHs are widely accepted and routinely used in clinical practice. DVHs enable comparison of dose distributions within target volumes and relative OARs, and provide DVH statistics such as D95 (the dose received by 95% of the target volume), Dmean (the mean dose received by the structure), and Dmax (the maximum dose received at any point in the structure), which are essential for evaluating treatment plan quality.

Gamma analysis is a quantitative method commonly used to compare dose distributions between sCT and CT by assessing both dose difference and spatial distance-to-agreement**.** A point passes if it meets predefined criteria (e.g., 3% dose difference and 3 mm distance), and the gamma pass rate reflects the percentage of points that satisfy these conditions. However, it has limitations. It is sensitive to the choice of thresholds, may overlook clinically relevant structure and does not offer spatially detailed information about where dose differences occur in relation to the PTV and OARs.

#### 2.3.2.7.3 Patient positioning verification

MRI-only radiotherapy workflows rely on sCT image to enable accurate patient positioning in the absence of conventional CT. Verifying patient setup involves assessing the suitability of sCT as a reference image for IGRT, where precise anatomical localisation is essential. As per LCC clinical practice, 3D or 4D CBCT was used for setup verification depending on the treatment site, following the same principle as the standard workflow, except using sCT instead of the planning CT as the reference image.

### 2.3.3 MRI-only clinical implementation

To ensure safe and effective clinical implementation of MRI-only radiotherapy, a multi-phase process has been introduced in the literature,

including commissioning, validation, and clinical use [54, 111, 123]. The first clinical use of MRI-only radiotherapy was implemented for prostate [129-131] and was also the first anatomical site to be supported by commercially available synthetic CT solutions [95, 129]. More recently, there has been growing interest in brain MRI-only for radiotherapy, supported by commercially available solutions. These facilitate a smoother transition to routine clinical use. At LCC, MRI-only radiotherapy has already been implemented for prostate cancer. MRI-only radiotherapy for the brain has now been commissioned and implemented at our centre. The work presented in Chapter 5 was used as part of the commissioning, and the first patient was treated in August 2025. Meanwhile, liver MRI-only radiotherapy remains under investigation and development stage. Although not yet clinically implemented, it is considered a promising site for future adoption, especially with ongoing advances in 4D MRI technology, which may enable motion management in abdominal regions [132].

As part of the pre-commissioning research, Chapter 5 assessed the Philips MRCAT solution, focusing on validating its clinical suitability in a large brain cohort for providing accurate dose calculation and reliable patient positioning comparable to conventional CT images. This evaluation was conducted retrospectively, without changing patient standard of care. However, several other technical considerations must be addressed to ensure safe transition to clinical use. For example, MRI geometric distortion, which can compromise spatial accuracy. Distortion correction strategies must be applied and verified using QA phantoms [52].

Another important aspect of MRI-only implementation is target and OAR delineation. Post-contrast T1w and T2 FLAIR images are commonly used for target delineation in brain radiotherapy due to their superior soft tissue contrast and tumour visibility [133, 134]. In contrast, OARs are typically delineated on CT, as structures such as the lacrimal glands, lenses, and bony structures are often better visualised on CT. One study compared MRI-only and CT-MRI workflows [122], providing local consensus recommendations for contouring practices. The authors recommended maintaining existing CT-MRI protocols for delineation and applied automatic segmentation of brain and bone structures on sCT images. However, contouring of critical structures like the lenses and lacrimal glands was not addressed. The Dixon water-phase sequence, which is

inherently registered with the sCT generated from the same MRI acquisition, may also support OAR delineation.

Another technical limitation in MRI-only workflows is the invisibility of the treatment couch and fixation mask on MRI or sCT images, which can impact dose calculation accuracy and patient setup. To address this, three studies have proposed practical solutions. Masitho et al. [135] used MRI-visible silicone to define the mask and couch position. Lerner et al. [128] used a zero echo time (ZTE) MRI sequence to directly visualise the treatment couch. Emin et al. [123] suggested using liquid markers on the couch surface combined with large FOV to manually identify couch positioning. A QA program must be developed based on identified risks. Once the commissioning criteria are met, the workflow progressed to the validation phase.

Following the commissioning phase, the validation phase involves prospective testing of the MRI-only workflow [123, 128], with CT scans still acquired as a backup for quality assurance. During this stage, treatment plans are generated and optimised on the sCT, then compared to CT plans to assess dosimetric accuracy. Once the validation stage is successfully completed and a comprehensive QA program is established, the workflow can transition to the clinical use phase.

In the clinical use phase, the CT is fully removed from the workflow. Routine QA procedures, daily, weekly and monthly focus on MRI scanner stability, sCT accuracy, and plan QA [123, 128]. Ongoing multidisciplinary collaboration and staff training are essential to maintaining the robustness and safety of the MRI-only workflow. The QA program adapted for brain MRI-only radiotherapy is illustrated in Figure 2.7, from a published study [123]. It outlines the key steps and decision points across MRI QA, sCT validation, and treatment plan verification to ensure safe clinical implementation.

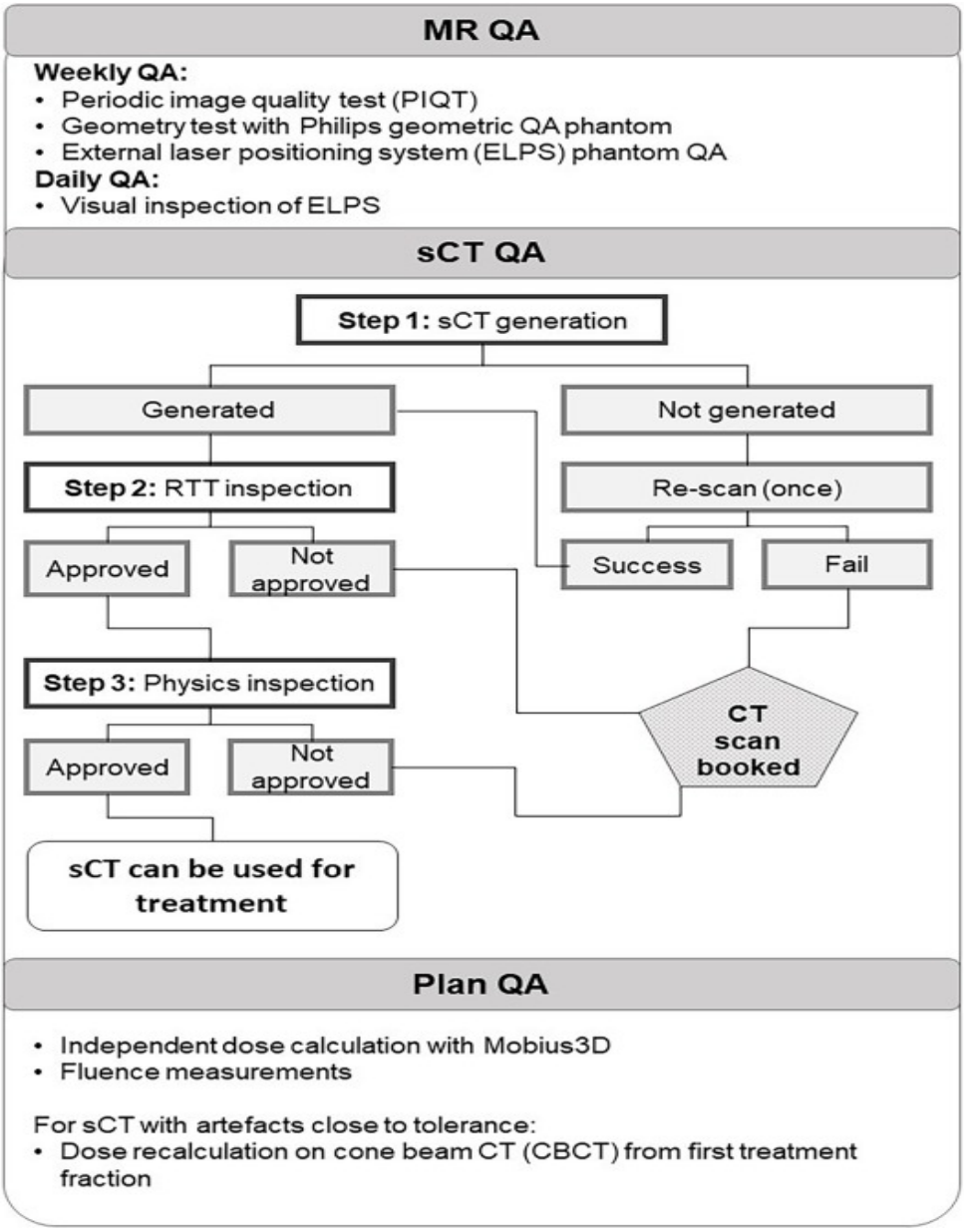


**Figure 2.7: A QA program for brain MRI-only radiotherapy, duplicated from [123].** *Abbreviation: radiographers (RRT) and quality assurance (QA).*

## 2.4 References


[1] NHS England. Cancer Registrations Statistics, England 2021- First release, counts only 2023 [updated 16 May 2024. Available from: https://digital.nhs.uk/data-and-information/publications/statistical/cancer-registration-statistics/england-2021---summary-counts-only/cancer-incidence.

[2] Cancer Research UK. Cancer mortality statistics 2022 [Available from: https://www.cancerresearchuk.org/health-professional/cancer-statistics/mortality#heading-Zero.

[3] National Cancer Institue. What Is Cancer? 2021 [updated October 11, 2021. Available from: https://www.cancer.gov/about-cancer/understanding/what-is-cancer.

[4] DeVita VT, Jr., Rosenberg SA. Two hundred years of cancer research. N Engl J Med. 2012;366:2207-14. 10.1056/NEJMra1204479.

[5] Borras JM, Lievens Y, Dunscombe P, Coffey M, Malicki J, Corral J, et al. The optimal utilization proportion of external beam radiotherapy in European countries: An ESTRO-HERO analysis. Radiother Oncol. 2015;116:38-44. 10.1016/j.radonc.2015.04.018.

[6] Baskar R, Lee KA, Yeo R, Yeoh KW. Cancer and radiation therapy: current advances and future directions. Int J Med Sci. 2012;9:193-9. 10.7150/ijms.3635.

[7] Spencer K, Parrish R, Barton R, Henry A. Palliative radiotherapy. BMJ. 2018;360:k821. 10.1136/bmj.k821.

[8] Barish RJ. Radiation Oncology Physics: A Handbook for Teachers and Students. LWW; 2006.

[9] Withers HR, Thames HD. Dose Fractionation and Volume Effects in Normal Tissues and Tumors. American Journal of Clinical Oncology. 1988;11

[10] Cancer Research UK. [Available from: https://www.cancerresearchuk.org/about-cancer/liver-cancer/treatment/treatment-options.

[11] SABR UK Consortium. Stereotactic Ablative Body Radiation Therapy (SABR) 2015 [Available from: https://www.sabr.org.uk/wp-content/uploads/2019/04/SABRconsortium-guidelines-2019-v6.1.0.pdf.

[12] Lukovic J, Dawson LA. Stereotactic body radiation therapy for colorectal cancer liver metastases. Journal of Gastrointestinal Oncology. 2023;15:1917-25

[13] Mahadevan A, Blanck O, Lanciano R, Peddada A, Sundararaman S, D'Ambrosio D, et al. Stereotactic Body Radiotherapy (SBRT) for liver metastasis – clinical outcomes from the international multi-institutional RSSearch® Patient Registry. Radiat Oncol. 2018;13:26. 10.1186/s13014-018-0969-2.

[14] Kimura T, Fujiwara T, Kameoka T, Adachi Y, Kariya S. The Current Role of Stereotactic Body Radiation Therapy (SBRT) in Hepatocellular Carcinoma (HCC). Cancers. 2022;14:4383

[15] Gerum S, Grambozov B, Roeder F. Stereotactic body radiation therapy (SBRT) in patients with hepatocellular cancer—a narrative review and expert opinion. Journal of Gastrointestinal Oncology. 2024;15:1880

[16] Griscom JT, Wolf PS. Liver metastasis. StatPearls [Internet]: StatPearls Publishing; 2023.

[17] Schmitt D, Blanck O, Gauer T, Fix MK, Brunner TB, Fleckenstein J, et al. Technological quality requirements for stereotactic radiotherapy. Strahlentherapie und Onkologie. 2020;196:421-43. 10.1007/s00066-020-01583-2.
[18] Cancer Research UK. Brain, other CNS and intracranial tumours mortality statistics: CRUK; [Available from: https://www.cancerresearchuk.org/health-professional/cancer-statistics/statistics-by-cancer-type/brain-other-cns-and-intracranial-tumours/mortality.
[19] Goodenberger ML, Jenkins RB. Genetics of adult glioma. Cancer Genetics. 2012;205:613-21. https://doi.org/10.1016/j.cancergen.2012.10.009.
[20] Bulbeck H, Noble K, Oliver K, Skinner TM. Challenges and opportunities in newly diagnosed glioblastoma in the United Kingdom: A Delphi panel. Neuro-Oncology Practice. 2024;11:740-52. 10.1093/nop/npae058.
[21] Le Calvez K, Mauricaite R, Treasure P, Booth TC, Price SJ, Brodbelt A, et al. Adult glioblastoma in England: Incidence, treatment, and outcomes with novel population-based strata. Cancer Epidemiology. 2025;97:102811. https://doi.org/10.1016/j.canep.2025.102811.
[22] Stupp R, Mason WP, van den Bent MJ, Weller M, Fisher B, Taphoorn MJ, et al. Radiotherapy plus concomitant and adjuvant temozolomide for glioblastoma. N Engl J Med. 2005;352:987-96. 10.1056/NEJMoa043330.
[23] Tan AC, Ashley DM, López GY, Malinzak M, Friedman HS, Khasraw M. Management of glioblastoma: State of the art and future directions. CA: a cancer journal for clinicians. 2020;70:299-312
[24] Weller M, van den Bent M, Preusser M, Le Rhun E, Tonn JC, Minniti G, et al. EANO guidelines on the diagnosis and treatment of diffuse gliomas of adulthood. Nat Rev Clin Oncol. 2021;18:170-86. 10.1038/s41571-020-00447-z.
[25] Brenner AW, Patel AJ. Review of Current Principles of the Diagnosis and Management of Brain Metastases. Front Oncol. 2022;12:857622. 10.3389/fonc.2022.857622.
[26] Vogelbaum MA, Brown PD, Messersmith H, Brastianos PK, Burri S, Cahill D, et al. Treatment for Brain Metastases: ASCO-SNO-ASTRO Guideline. Journal of Clinical Oncology. 2021;40:492-516. 10.1200/JCO.21.02314.
[27] Redmond KJ, De Salles AAF, Fariselli L, Levivier M, Ma L, Paddick I, et al. Stereotactic Radiosurgery for Postoperative Metastatic Surgical Cavities: A Critical Review and International Stereotactic Radiosurgery Society (ISRS) Practice Guidelines. International Journal of Radiation Oncology*Biology*Physics. 2021;111:68-80. https://doi.org/10.1016/j.ijrobp.2021.04.016.
[28] England N. Clinical Commissioning Policy: Stereotactic radiosurgery/radiotherapy for cerebral metastases. 2013.
[29] Shah SN, Shah SS, Shukla G, Shah SA. Conformal Partial Brain Irradiation Versus Stereotactic Radiation Therapy in the Management of Resected Brain Metastases: A Retrospective Study. Cureus. 2025;17:e77762. 10.7759/cureus.77762.
[30] Noble DJ, Ramaesh R, Brothwell M, Elumalai T, Barrett T, Stillie A, et al. The Evolving Role of Novel Imaging Techniques for Radiotherapy Planning. Clin Oncol. 2024;36:514-26. 10.1016/j.clon.2024.05.018.

[31] E. P. Radiation Oncology Physics: a Handbook for Teachers and Students. Vienna:: International Atomic Energy Agency; 2005.
[32] Pereira GC, Traughber M, Muzic RF, Jr. The role of imaging in radiation therapy planning: past, present, and future. Biomed Res Int. 2014;2014:231090. 10.1155/2014/231090.
[33] Royal College of Radiologists. On Target 2 updated guidance for image-guided radiotherapy: Radiotherapy board; 2021 [Available from: https://www.rcr.ac.uk/sites/default/files/radiotherapy-board-on-target-2-updated-guidance-image-guided-radiotherapy.pdf.
[34] Mutic S, Palta JR, Butker EK, Das IJ, Huq MS, Loo L-ND, et al. Quality assurance for computed-tomography simulators and the computed-tomography-simulation process: Report of the AAPM Radiation Therapy Committee Task Group No. 66. Medical Physics. 2003;30:2762-92. https://doi.org/10.1118/1.1609271.
[35] Aird EGA, Conway J. CT simulation for radiotherapy treatment planning. British Journal of Radiology. 2014;75:937-49. 10.1259/bjr.75.900.750937.
[36] Paul Hatfield SP, Esther Macmillan. Radiotherapy to the brain The Leeds Teaching Hospital [updated 24/10/2024. 008:[Available from: https://www.leedsth.nhs.uk/patients/resources/radiotherapy-to-the-brain/.
[37] Goody EB, Richard Garratt. Stereotactic Ablative Radiotherapy (SABR) to the liver The Leeds Teaching Hospital [updated 24/10/2024. 003:[Available from: https://www.leedsth.nhs.uk/patients/resources/stereotactic-ablative-radiotherapy-sabr-to-the-liver/#:~:text=The%20treatment%20technique%20used%20is,for%20you%20during%20your%20treatment.
[38] Keall PJ, Mageras GS, Balter JM, Emery RS, Forster KM, Jiang SB, et al. The management of respiratory motion in radiation oncology report of AAPM Task Group 76 a. Medical physics. 2006;33:3874-900. 10.1118/1.2349696.
[39] Pan T. Comparison of helical and cine acquisitions for 4D-CT imaging with multislice CT. Medical physics. 2005;32:627-34
[40] Parker DL. Optimal short scan convolution reconstruction for fan beam CT. Medical physics. 1982;9:254-7
[41] Vedam S, Keall P, Kini V, Mostafavi H, Shukla H, Mohan R. Acquiring a four-dimensional computed tomography dataset using an external respiratory signal. Physics in Medicine & Biology. 2002;48:45
[42] Heinz C, Reiner M, Belka C, Walter F, Söhn M. Technical evaluation of different respiratory monitoring systems used for 4D CT acquisition under free breathing. J Appl Clin Med Phys. 2015;16:334-49
[43] Beddar AS, Kainz K, Briere TM, Tsunashima Y, Pan T, Prado K, et al. Correlation between internal fiducial tumor motion and external marker motion for liver tumors imaged with 4D-CT. International Journal of Radiation Oncology* Biology* Physics. 2007;67:630-8
[44] Li R, Lewis JH, Cerviño LI, Jiang SB. 4D CT sorting based on patient internal anatomy. Phys Med Biol. 2009;54:4821-33. 10.1088/0031-9155/54/15/012.
[45] Abdelnour A, Nehmeh S, Pan T, Humm J, Vernon P, Schöder H, et al. Phase and amplitude binning for 4D-CT imaging. Physics in medicine & biology. 2007;52:3515

[46] Yamamoto T, Langner U, Loo BW, Jr., Shen J, Keall PJ. Retrospective analysis of artifacts in four-dimensional CT images of 50 abdominal and thoracic radiotherapy patients. Int J Radiat Oncol Biol Phys. 2008;72:1250-8. https://doi.org/10.1016/j.ijrobp.2008.06.1937.
[47] Aldosary G. Four-Dimensional Computed Tomography (4DCT) in Radiation Oncology: A Practical Overview. Current Radiology Reports. 2024;12:65-76
[48] Sentker T, Schmidt V, Ozga A-K, Petersen C, Madesta F, Hofmann C, et al. 4D CT image artifacts affect local control in SBRT of lung and liver metastases. Radiother Oncol. 2020;148:229-34. 10.1016/j.radonc.2020.04.006.
[49] McRobbie DW, Moore EA, Graves MJ, Prince MR. MRI from Picture to Proton: Cambridge university press; 2017.
[50] Westbrook C, Talbot J. MRI in Practice: John Wiley & Sons; 2018.
[51] Elster AD. Questions and Answers in MRI 1994 [Available from: MRIquestions.com.
[52] Speight R, Dubec M, Eccles CL, George B, Henry A, Herbert T, et al. IPEM topical report: guidance on the use of MRI for external beam radiotherapy treatment planning. Phys Med Biol. 2021; 66:055025. https://doi.org/10.1088/1361-6560/abdc30.
[53] Glide-Hurst CK, Paulson ES, McGee K, Tyagi N, Hu Y, Balter J, et al. Task group 284 report: magnetic resonance imaging simulation in radiotherapy: considerations for clinical implementation, optimization, and quality assurance. Med Phys. 2021;48:e636-e70. 10.1002/mp.14695.
[54] Moore-Palhares D, Ho L, Lu L, Chugh B, Vesprini D, Karam I, et al. Clinical implementation of magnetic resonance imaging simulation for radiation oncology planning: 5 year experience. Radiat Oncol. 2023;18:27. 10.1186/s13014-023-02209-4.
[55] Speight R, Tyyger M, Schmidt MA, Liney G, Johnstone R, Eccles CL, et al. IPEM Topical Report: an international IPEM survey of MRI use for external beam radiotherapy treatment planning. Phys Med Biol. 2021;66. 10.1088/1361-6560/abe9f7.
[56] Tang S, Rai R, Vinod SK, Elwadia D, Forstner D, Moretti D, et al. Rates of MRI simulator utilisation in a tertiary cancer therapy centre. J Med Imag Radiat Oncol. 2022;66:717-23. https://doi.org/10.1111/1754-9485.13422.
[57] Niyazi M, Andratschke N, Bendszus M, Chalmers AJ, Erridge SC, Galldiks N, et al. ESTRO-EANO guideline on target delineation and radiotherapy details for glioblastoma. Radiother Oncol. 2023;184. 10.1016/j.radonc.2023.109663.
[58] Eaton DJ, Byrne JP, Cosgrove VP, Thomas SJ. Unintended doses in radiotherapy—over, under and outside? The British Journal of Radiology. 2018;91:20170863
[59] Segedin B, Petric P. Uncertainties in target volume delineation in radiotherapy–are they relevant and what can we do about them? Radiology and oncology. 2016;50:254
[60] Fiorentino A, Caivano R, Pedicini P, Fusco V. Clinical target volume definition for glioblastoma radiotherapy planning: magnetic resonance imaging and computed tomography. Clinical and Translational Oncology. 2013;15:754-8

[61] Khoo VS, Adams EJ, Saran F, Bedford JL, Perks JR, Warrington AP, et al. A comparison of clinical target volumes determined by CT and MRI for the radiotherapy planning of base of skull meningiomas. International Journal of Radiation Oncology*Biology*Physics. 2000;46:1309-17. https://doi.org/10.1016/S0360-3016(99)00541-6.

[62] Chen H-y, Ma X-m, Ye M, Hou Y-l, Hu B, Bai Y-r. CT-pathologic correlation in primary hepatocellular carcinoma: an implication for target delineation. Journal of Radiation Research. 2013;54:938-42. 10.1093/jrr/rrt030.

[63] Srinivasan S, Dasgupta A, Chatterjee A, Baheti A, Engineer R, Gupta T, et al. The Promise of Magnetic Resonance Imaging in Radiation Oncology Practice in the Management of Brain, Prostate, and GI Malignancies. JCO Glob Oncol. 2022;8:e2100366. 10.1200/go.21.00366.

[64] Marshall C, Thirion P, Mihai A, Armstrong JG, Cournane S, Hickey D, et al. Interobserver Variability of Gross Tumor Volume Delineation for Colorectal Liver Metastases Using Computed Tomography and Magnetic Resonance Imaging. Adv Radiat Oncol. 2023;8:101020. 10.1016/j.adro.2022.101020.

[65] Peltenburg JE, Hosni A, Bahij R, Boeke S, Braam PM, Hall WA, et al. Interobserver variation in tumor delineation of liver metastases using Magnetic Resonance Imaging. Physics and Imaging in Radiation Oncology. 2024;30:100592. https://doi.org/10.1016/j.phro.2024.100592.

[66] Weltens C, Menten J, Feron M, Bellon E, Demaerel P, Maes F, et al. Interobserver variations in gross tumor volume delineation of brain tumors on computed tomography and impact of magnetic resonance imaging. Radiother Oncol. 2001;60:49-59. 10.1016/s0167-8140(01)00371-1.

[67] McGee KP, Cao M, Das IJ, Yu V, Witte RJ, Kishan AU, et al. The Use of Magnetic Resonance Imaging in Radiation Therapy Treatment Simulation and Planning. Journal of Magnetic Resonance Imaging. 2024;60:1786-805

[68] Aldawsari AM, Al-Qaisieh B, Broadbent DA, Bird D, Murray L, Speight R. The role and potential of using quantitative MRI biomarkers for imaging guidance in brain cancer radiotherapy treatment planning: A systematic review. Phys Imaging Radiat Oncol. 2023;27:100476. 10.1016/j.phro.2023.100476.

[69] Li M, Zhang Q, Yang K. Role of MRI-based functional imaging in improving the therapeutic index of radiotherapy in cancer treatment. Frontiers in Oncology. 2021;11:645177

[70] Brock KK, Mutic S, McNutt TR, Li H, Kessler ML. Use of image registration and fusion algorithms and techniques in radiotherapy: Report of the AAPM Radiation Therapy Committee Task Group No. 132. Med Phys. 2017;44:e43-e76. 10.1002/mp.12256.

[71] Liney G, van der Heide U. MRI for radiotherapy: planning, delivery, and response assessment: Springer; 2019.

[72] Washington C, Leaver D. Principles and Practice of Radiation Therapy. 4th Edition ed2015.

[73] Prescribing I. recording and reporting photon beam therapy (supplement to ICRU report 50). ICRU report. 1999;62

[74] The ICRU Report 83: prescribing, recording and reporting photon-beam intensity-modulated radiation therapy (IMRT) 2012 [97-9]. Available from: https://academic.oup.com/jicru/article-lookup/doi/10.1093/jicru/ndq002.

[75] Yoganathan SA, Maria Das KJ, Agarwal A, Kumar S. Magnitude, Impact, and Management of Respiration-induced Target Motion in Radiotherapy Treatment: A Comprehensive Review. J Med Phys. 2017;42:101-15. 10.4103/jmp.JMP_22_17.
[76] Li G, Liu Y, Nie X. Respiratory-Correlated (RC) vs. Time-Resolved (TR) Four-Dimensional Magnetic Resonance Imaging (4DMRI) for Radiotherapy of Thoracic and Abdominal Cancer. Front Oncol. 2019;9:1024. https://dx.doi.org/10.3389/fonc.2019.01024.
[77] Stemkens B, Paulson ES, Tijssen RHN. Nuts and bolts of 4D-MRI for radiotherapy. Phys Med Biol. 2018;63:21TR01. https://doi.org/10.1088/1361-6560/aae56d.
[78] Thomas HR, Miao X, Ferguson D, Calvin C, Bhaskar Krishnamurthy U, Anwar M, et al. Contrast-enhanced 4D-MRI for internal target volume generation in treatment planning for liver tumors. Radiat Oncol. 2022;173:69-76. https://doi.org/10.1016/j.radonc.2022.05.037.
[79] Liao Y-P, Xiao H, Wang P, Li T, Aguilera TA, Visak JD, et al. Internal Target Volume Estimation for Liver Cancer Radiation Therapy Using an Ultra Quality 4D MRI. Advances in Radiation Oncology. 2025:101774
[80] Hansen CR, Hussein M, Bernchou U, Zukauskaite R, Thwaites D. Plan quality in radiotherapy treatment planning – Review of the factors and challenges. J Med Imag Radiat Oncol. 2022;66:267-78. https://doi.org/10.1111/1754-9485.13374.
[81] Teoh M, Clark CH, Wood K, Whitaker S, Nisbet A. Volumetric modulated arc therapy: a review of current literature and clinical use in practice. The British journal of radiology. 2011;84:967-96
[82] Sood S, Pokhrel D, McClinton C, Lominska C, Badkul R, Jiang H, et al. Volumetric-modulated arc therapy (VMAT) for whole brain radiotherapy: not only for hippocampal sparing, but also for reduction of dose to organs at risk. Med Dosim. 2017;42:375-83. 10.1016/j.meddos.2017.07.005.
[83] Sheu T, Briere TM, Olanrewaju AM, McAleer MF. Intensity Modulated Radiation Therapy Versus Volumetric Arc Radiation Therapy in the Treatment of Glioblastoma—Does Clinical Benefit Follow Dosimetric Advantage? Advances in Radiation Oncology. 2019;4:50-6
[84] Cantaloube M, Castan F, Creoff M, Prunaretty J, Bordeau K, Michalet M, et al. Image-guided liver stereotactic body radiotherapy using VMAT and real-time adaptive tumor gating: evaluation of the efficacy and toxicity for hepatocellular carcinoma. Cancers. 2021;13:4853
[85] Goyal S, Kataria T. Image guidance in radiation therapy: techniques and applications. Radiology research and practice. 2014;2014:705604
[86] Herrmann H, Seppenwoolde Y, Georg D, Widder J. Image guidance: past and future of radiotherapy. Der Radiologe. 2019;59:21
[87] Verellen D, De Ridder M, Storme G. A (short) history of image-guided radiotherapy. Radiother Oncol. 2008;86:4-13
[88] Zhang Y, Jiang Z, Zhang Y, Ren L. A review on 4D cone-beam CT (4D-CBCT) in radiation therapy: Technical advances and clinical applications. Medical Physics. 2024;51:5164-80. https://doi.org/10.1002/mp.17269.
[89] Srinivasan K, Mohammadi M, Shepherd J. Applications of linac-mounted kilovoltage Cone-beam Computed Tomography in modern radiation therapy: A review. Polish journal of radiology. 2014;79:181
[90] Radiologists TRCo. On target 2: updated guidance for image-guided radiotherapy 2021 [Available from: https://rcr.ac.uk/our-services/all-our-

publications/clinical-oncology-publications/on-target-2-updated-guidance-for-image-guided-radiotherapy/.

[91] Jonsson J, Nyholm T, Söderkvist K. The rationale for MR-only treatment planning for external radiotherapy. Clinical and Translational Radiation Oncology. 2019;18:60-5. https://doi.org/10.1016/j.ctro.2019.03.005.

[92] Owrangi AM, Greer PB, Glide-Hurst CK. MRI-only treatment planning: benefits and challenges. Physics in Medicine & Biology. 2018;63:05TR1

[93] Ulin K, Urie MM, Cherlow JM. Results of a multi-institutional benchmark test for cranial CT/MR image registration. Int J Radiat Oncol Biol Phys. 2010;77:1584-9. https://doi.org/10.1016/j.ijrobp.2009.10.017.

[94] Brock KKPD. Results of a Multi-Institution Deformable Registration Accuracy Study (MIDRAS). International journal of radiation oncology, biology, physics. 2010;76:583-96. 10.1016/j.ijrobp.2009.06.031.

[95] Tyagi N, Fontenla S, Zelefsky M, Chong-Ton M, Ostergren K, Shah N, et al. Clinical workflow for MR-only simulation and planning in prostate. Radiat Oncol. 2017;12:119. 10.1186/s13014-017-0854-4.

[96] Persson E, Svanberg N, Scherman J, Jamtheim Gustafsson C, Fridhammar A, Hjalte F, et al. MRI-only radiotherapy from an economic perspective: Can new techniques in prostate cancer treatment be cost saving? Clin Transl Radiat Oncol. 2023;38:183-7. 10.1016/j.ctro.2022.11.012.

[97] Korhonen J, Visapää H, Seppälä T, Kapanen M, Saarilahti K, Tenhunen M. Clinical experiences of treating prostate cancer patients with magnetic resonance imaging–only based radiation therapy treatment planning workflow. International Journal of Radiation Oncology, Biology, Physics. 2016;96:S225

[98] Boulanger M, Nunes J-C, Chourak H, Largent A, Tahri S, Acosta O, et al. Deep learning methods to generate synthetic CT from MRI in radiotherapy: A literature review. Physica medica. 2021;89:265-81. https://doi.org/10.1016/j.ejmp.2021.07.027.

[99] Edmund JM, Nyholm T. A review of substitute CT generation for MRI-only radiation therapy. Radiation oncology (London, England). 2017;12:28-. 10.1186/s13014-016-0747-y.

[100] Johnstone E, Wyatt JJ, Henry AM, Short SC, Sebag-Montefiore D, Murray L, et al. Systematic Review of Synthetic Computed Tomography Generation Methodologies for Use in Magnetic Resonance Imaging-Only Radiation Therapy. Int J Radiat Oncol Biol Phys. 2018;100:199-217. 10.1016/j.ijrobp.2017.08.043.

[101] Spadea MF, Maspero M, Zaffino P, Seco J. Deep learning based synthetic-CT generation in radiotherapy and PET: A review. Med Phys. 2021;48:6537-66. 10.1002/mp.15150.

[102] Tyagi N, Fontenla S, Zhang J, Cloutier M, Kadbi M, Mechalakos J, et al. Dosimetric and workflow evaluation of first commercial synthetic CT software for clinical use in pelvis. Phys Med Biol. 2017;62:2961-75. 10.1088/1361-6560/aa5452.

[103] O'Connor LM, Skehan K, Choi JH, Simpson J, Martin J, Warren-Forward H, et al. Optimisation and validation of an integrated magnetic resonance imaging-only radiotherapy planning solution. Phys Imaging Radiat Oncol. 2021;20:34-9. 10.1016/j.phro.2021.10.001.

[104] Andreasen D, Van Leemput K, Hansen RH, Andersen JA, Edmund JM. Patch-based generation of a pseudo CT from conventional MRI

sequences for MRI-only radiotherapy of the brain. Medical physics. 2015;42:1596-605

[105] Edmund JM, Andreasen D, Mahmood F, Van Leemput K. Cone beam computed tomography guided treatment delivery and planning verification for magnetic resonance imaging only radiotherapy of the brain. Acta oncologica. 2015;54:1496-500

[106] Guerreiro F, Koivula L, Seravalli E, Janssens GO, Maduro JH, Brouwer CL, et al. Feasibility of MRI-only photon and proton dose calculations for pediatric patients with abdominal tumors. Physics in Medicine & Biology. 2019;64:055010

[107] Bredfeldt JS, Liu L, Feng M, Cao Y, Balter JM. Synthetic CT for MRI-based liver stereotactic body radiotherapy treatment planning. Phys Med Biol. 2017;62:2922-34. 10.1088/1361-6560/aa5059.

[108] Hsu SH, DuPre P, Peng Q, Tomé WA. A technique to generate synthetic CT from MRI for abdominal radiotherapy. J Appl Clin Med Phys. 2020;21:136-43. 10.1002/acm2.12816.

[109] Bahloul MA, Jabeen S, Benoumhani S, Alsaleh HA, Belkhatir Z, Al-Wabil A. Advancements in synthetic CT generation from MRI: A review of techniques, and trends in radiation therapy planning. J Appl Clin Med Phys. 2024;25:e14499

[110] Han X. MR-based synthetic CT generation using a deep convolutional neural network method. Medical Physics. 2017;44:1408-19. https://doi.org/10.1002/mp.12155.

[111] Villegas F, Dal Bello R, Alvarez-Andres E, Dhont J, Janssen T, Milan L, et al. Challenges and opportunities in the development and clinical implementation of artificial intelligence based synthetic computed tomography for magnetic resonance only radiotherapy. Radiother Oncol. 2024;198:110387. 10.1016/j.radonc.2024.110387.

[112] Cusumano D, Lenkowicz J, Votta C, Boldrini L, Placidi L, Catucci F, et al. A deep learning approach to generate synthetic CT in low field MR-guided adaptive radiotherapy for abdominal and pelvic cases. Radiother Oncol. 2020;153:205-12. 10.1016/j.radonc.2020.10.018.

[113] Florkow MC, Guerreiro F, Zijlstra F, Seravalli E, Janssens GO, Maduro JH, et al. Deep learning-enabled MRI-only photon and proton therapy treatment planning for paediatric abdominal tumours. Radiother Oncol. 2020;153:220-7. https://doi.org/10.1016/j.radonc.2020.09.056.

[114] Fu J, Singhrao K, Cao M, Yu V, Santhanam AP, Yang Y, et al. Generation of abdominal synthetic CTs from 0.35 T MR images using generative adversarial networks for MR-only liver radiotherapy. Biomed Phys Eng Express. 2020;6:015033

[115] Kang SK, An HJ, Jin H, Kim J-i, Chie EK, Park JM, et al. Synthetic CT generation from weakly paired MR images using cycle-consistent GAN for MR-guided radiotherapy. Biomedical engineering letters. 2021;11:263-71

[116] Liu L, Johansson A, Cao Y, Dow J, Lawrence TS, Balter JM. Abdominal synthetic CT generation from MR Dixon images using a U-net trained with ‘semi-synthetic’CT data. Physics in Medicine & Biology. 2020;65:125001

[117] Liu Y, Lei Y, Wang T, Kayode O, Tian S, Liu T, et al. MRI-based treatment planning for liver stereotactic body radiotherapy: validation of a deep learning-based synthetic CT generation method. The British Journal of Radiology. 2019;92:20190067

[118] Liu Y, Lei Y, Wang Y, Wang T, Ren L, Lin L, et al. MRI-based treatment planning for proton radiotherapy: dosimetric validation of a deep learning-based liver synthetic CT generation method. Physics in Medicine & Biology. 2019;64:145015. 10.1088/1361-6560/ab25bc.
[119] Qian P, Xu K, Wang T, Zheng Q, Yang H, Baydoun A, et al. Estimating CT from MR abdominal images using novel generative adversarial networks. Journal of Grid Computing. 2020;18:211-26
[120] Xu K, Cao J, Xia K, Yang H, Zhu J, Wu C, et al. Multichannel residual conditional GAN-leveraged abdominal pseudo-CT generation via Dixon MR images. IEEE Access. 2019;7:163823-30
[121] Jin CB, Kim H, Liu M, Jung W, Joo S, Park E, et al. Deep CT to MR Synthesis Using Paired and Unpaired Data. Sensors (Basel). 2019;19. 10.3390/s19102361.
[122] Rossi E, Emin S, Gubanski M, Gagliardi G, Hedman M, Villegas F. Contouring practices and artefact management within a synthetic CT-based radiotherapy workflow for the central nervous system. Radiat Oncol. 2024;19:27. https://doi.org/10.1186/s13014-024-02422-9.
[123] Emin S, Rossi E, Rooth EM, Dorniok T, Hedman M, Gagliardi G, et al. Clinical implementation of a commercial synthetic computed tomography solution for radiotherapy treatment of glioblastoma. Physics and Imaging in Radiation Oncology. 2024;30:100589. https://doi.org/10.1016/j.phro.2024.100589.
[124] Ranta I, Wright P, Suilamo S, Kemppainen R, Schubert G, Kapanen M, et al. Clinical feasibility of a commercially available MRI-only method for radiotherapy treatment planning of the brain. J Appl Clin Med Phys. 2023;24:e14044. https://doi.org/10.1002/acm2.14044.
[125] Yip TTY, Li Z, Li T. Clinical validation of MR-generated synthetic CT by MRCAT for brain tumor radiotherapy. J Appl Clin Med Phys. 2025;26. https://doi.org/10.1002/acm2.14494.
[126] Levardon M, Autret D, Le Dorze T, Guillerminet C, Dufreneix S. Brain MR-only workflow in clinical practice: A comparison among generators for quality assurance and patient positioning. J Appl Clin Med Phys. 2024:e14583. https://doi.org/10.1002/acm2.14583.
[127] Masitho S, Szkitsak J, Grigo J, Fietkau R, Putz F, Bert C. Feasibility of artificial-intelligence-based synthetic computed tomography in a magnetic resonance-only radiotherapy workflow for brain radiotherapy: Two-way dose validation and 2D/2D kV-image-based positioning. Physics and Imaging in Radiation Oncology. 2022;24:111-7. https://doi.org/10.1016/j.phro.2022.10.002.
[128] Lerner M, Medin J, Jamtheim Gustafsson C, Alkner S, Siversson C, Olsson LE. Clinical validation of a commercially available deep learning software for synthetic CT generation for brain. Radiat Oncol. 2021;16:1-11. https://doi.org/10.1186/s13014-021-01794-6.
[129] Bird D, Henry AM, Sebag-Montefiore D, Buckley DL, Al-Qaisieh B, Speight R. A Systematic Review of the Clinical Implementation of Pelvic Magnetic Resonance Imaging–Only Planning for External Beam Radiation Therapy. International Journal of Radiation Oncology*Biology*Physics. 2019;105:479-92. https://doi.org/10.1016/j.ijrobp.2019.06.2530.
[130] Tyagi N, Zelefsky MJ, Wibmer A, Zakian K, Burleson S, Happersett L, et al. Clinical experience and workflow challenges with magnetic resonance-only radiation therapy simulation and planning for prostate

cancer. Phys Imaging Radiat Oncol. 2020;16:43-9. 10.1016/j.phro.2020.09.009.

[131] Persson E, Jamtheim Gustafsson C, Ambolt P, Engelholm S, Ceberg S, Bäck S, et al. MR-PROTECT: Clinical feasibility of a prostate MRI-only radiotherapy treatment workflow and investigation of acceptance criteria. Radiat Oncol. 2020;15:77. 10.1186/s13014-020-01513-7.

[132] Aljaafari L, Bird D, Buckley DL, Al-Qaisieh B, Speight R. A systematic review of 4D magnetic resonance imaging techniques for abdominal radiotherapy treatment planning. Physics and Imaging in Radiation Oncology. 2024;31:100604. https://doi.org/10.1016/j.phro.2024.100604.

[133] Niyazi M, Andratschke N, Bendszus M, Chalmers AJ, Erridge SC, Galldiks N, et al. ESTRO-EANO guideline on target delineation and radiotherapy details for glioblastoma. Radiother Oncol. 2023;184:109663. https://doi.org/10.1016/j.radonc.2023.109663.

[134] Paulson ES, Crijns SP, Keller BM, Wang J, Schmidt MA, Coutts G, et al. Consensus opinion on MRI simulation for external beam radiation treatment planning. Radiother Oncol. 2016;121:187-92

[135] Masitho S, Grigo J, Brandt T, Lambrecht U, Szkitsak J, Weiss A, et al. Synthetic CTs for MRI-only brain RT treatment: integration of immobilization systems. Strahlentherapie und Onkologie. 2023;199:739-48

# Chapter 3 A systematic review of 4D magnetic resonance imaging techniques for abdominal radiotherapy treatment planning.

**Chapter note:** Supplementary materials referenced in this chapter are provided in Appendix A. Additional information of the updated systematic review search are available in Appendix B. The work was presented as a poster at ESTRO 2024 (see Appendix C). This chapter has been published in *Physics and Imaging in Radiation Oncology. 2024;31:100604. https://doi.org/10.1016/j.phro.2024.100604.*

## Abstract

**Background and purpose:** Four-dimensional magnetic resonance imaging (4D MRI) has gained interest as an alternative to the current standard for motion management four-dimensional tomography (4D CT) in abdominal radiotherapy treatment planning (RTP). This review aims to assess the 4D MRI literature in abdomen, focusing on technical considerations and the validity of using 4D MRI for patients within radiotherapy protocols.

**Materials and methods:** The review followed the Preferred Reporting Items for Systematic Reviews and Meta-Analyses (PRISMA) guidelines. A comprehensive search was performed across the Medline, Embase, Scopus, and Web of Science databases, covering all years up to December 31, 2023. The studies were grouped into two categories: 4D MRI reconstructed from 3D MRI acquisition; and 4D MRI reconstructed from multi-slice 2D MRI acquisition.

**Results:** A total of 39 studies met the inclusion criteria and were analysed to provide key findings. Key findings were that 4D MRI had the potential to improve abdominal RTP for patients by providing accurate tumour definition and motion assessment compared to 4D CT. 4D MRI reconstructed from 3D MRI acquisition showed promise as a feasible approach for motion management in abdominal RTP regarding spatial resolution. Currently, the slice thickness achieved on 4D MRI reconstructed from multi-slice 2D MRI acquisitions is unsuitable for clinical purposes. Lastly, the current barriers for clinical implementation of 4D MRI are the limited availability of validated commercial

solutions and the lack of larger cohort comparative studies to 4D CT for target delineation and plan optimisation.

**Conclusion:** 4D MRI showed potential improvements in abdominal RTP, but standards and guidelines for the use of 4D MRI in radiotherapy were required to demonstrate clinical benefits.

**Keywords:** four-dimensional computed tomography; four-dimensional magnetic resonance imaging; motion management; abdominal radiotherapy treatment planning.

## 3.1 Introduction

Radiotherapy aims to deliver the prescribed dose to the target area whilst minimising radiation to healthy tissues. For accurate treatment planning, advanced imaging techniques are used to identify the targets and organs at risk (OAR), calculate the dose, and verify positioning before and during treatment. However, there can be geometric uncertainties caused by motion which may result in underdosing the target or overdosing OAR. For abdominal radiotherapy breathing motion is a source of uncertainty and must be managed appropriately [1]. Currently, abdominal radiotherapy relies on four-dimensional CT (4D CT) for managing motion [2]. 4D CT acquires data over several minutes over multiple breathing cycle while the patient slowly moves through the CT scanner with projections being acquired and linked to when in a breathing cycle they were acquired. Data is binned based on amplitude or phase within the breathing cycle, with all projection data within that bin being used to reconstruct an image corresponding to that bin. This 4D CT data provides information about tumour motion during breathing to help with target delineation. However, 4D CT has limitations such as poor soft tissue contrast, motion artefacts, reliance on liver motion to estimate tumour movement that lead to uncertainties related to tumour position [3, 4].

As an alternative to 4D CT, four-dimensional magnetic resonance imaging (4D MRI) has emerged as a tool for planning radiotherapy. It offers better visualisation of tumours and potentially more accurate motion estimation as it does not rely on the diaphragm motion as a surrogate for tumour motion. Recently, there has been a growing interest in developing 4D MRI for radiotherapy [5-7]. These applications can broadly be categorised into multislice

2D MRI data acquisition and 3D MRI data acquisition repeatedly acquired, where the 4$^{th}$ dimension can be reconstructed into respiratory-correlated 4D MRI (RC-4D MRI) or time-resolved 4D MRI (TR-4D MRI). RC-4D MRI is acquired over several minutes capturing breathing cycles during scanning. This is achieved by binning and averaging data acquired in multiple breathing cycles to represent the motion in different phases, hence they assume breathing is periodic. Whereas TR-4D MRI involves capturing a series of fast 3D images over time. This eliminates the need to assume periodic respiratory motion and avoids inconsistency in binning the data during 4D reconstruction.

Despite these efforts, the clinical implementation of 4D MRI in practice remains limited. To the best of the author's knowledge, there was no systematic review specifically focused on clinical requirements to develop 4D MRI in abdominal radiotherapy. Existing reviews primarily discussed different approaches and challenges in acquiring and using 4D MRI for radiotherapy [5-7]. Thus, to facilitate future research, it is essential to develop 4D MRI technologies that align with the standard requirements for MRI use in radiotherapy. The aim of this review is to evaluate the current literature reports on the use of 4D MRI during simulation in abdominal planning. Its scope focused on technical considerations and the validity of using 4D MRI for patients within radiotherapy protocols.

## 3.2 Method and materials

A systematic review was conducted to evaluate publications that investigated the use of 4D MRI techniques for radiotherapy treatment planning in the abdomen. The review followed the Preferred Reporting Items for Systematic Reviews and Meta-Analyses guidelines [8]. The search was performed on the Embase, Medline, Scopus, and Web of Science databases for all years up to December 31, 2023, using the search protocols in supplementary material A. A wide search criterion was implemented to ensure the inclusion of all relevant papers in the review. Articles were included that referred to '4D MRI' and 'respiratory motion' and 'radiotherapy' or their synonyms in the title and abstract. The search results for each database were combined, and duplicates were removed. The remaining results were screened using 3 levels. Primary screening involved evaluating titles and abstracts for specific use of 4D MRI in radiotherapy. Articles that focused on organs unrelated to respiratory motion or

were not relevant to 4D MRI and radiotherapy were excluded. Abstracts, and review articles were excluded. The secondary screening evaluated titles and abstracts and focused on the utilisation of 4D MRI in abdominal treatment planning applications. Articles related to 4D MRI acquired for online magnetic resonance guided radiotherapy (MRgRT) were excluded from the review, including studies involving tumour tracking, and adaptation. Additionally, studies that used orthogonal 2D cine, 4D synthetic CT (4D sCT), solely in lung patients or involved animals were also excluded. Tertiary screening involved full-text screening, and studies acquired in volunteers or phantoms only were excluded as they did not meet the inclusion criteria for abdominal radiotherapy. The primary organs of interest in this review were the liver, pancreas, and kidneys. After identifying the eligible studies, a backward and forward citation search was conducted to identify any additional relevant studies.

The eligible studies were then categorised based on the method of data acquisition (1) 3D MRI data acquisition and (2) multi-slice 2D MRI data acquisition. Key findings from each study were summarised in data tables for each category. To be applicable in clinical settings, the included articles have been evaluated based on criteria essential to using MRI in radiotherapy [9]. These criteria include spatial resolution, slice thickness, temporal resolution, geometric fidelity of 4D MRI, field of view (FOV), scan time, reconstruction time, and methods of validation in cancer patients.

## 3.3 Results

### 3.3.1 Study selection

Figure 3.1 presents the results of the database search. Initially, the combined databases search produced 3286 records, which were then refined to 1004 unique records by removing duplicates. Following primary title and abstract screening, 294 records remained. Secondary screening identified 75 studies for retrieval, and out of these, 75 studies underwent tertiary full-text screening. A total of 36 studies met the inclusion criteria. Furthermore, an additional 3 studies were discovered through forward and backward citation searches, bringing the total number of included studies in this systematic review to 39. Table 3.1 provides a breakdown of the excluded articles based on their classifications and quantities.

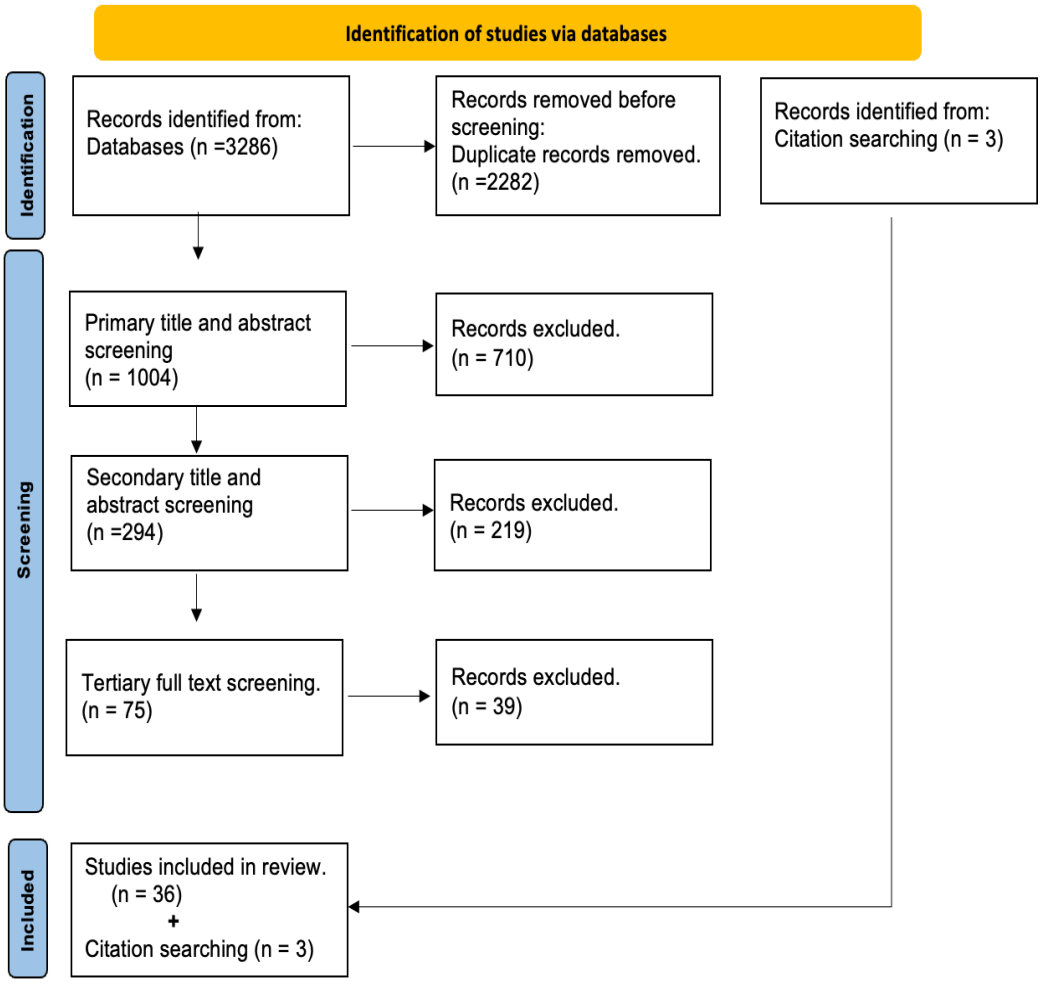


**Figure 3.1: Flowchart of the systematic review process, including the number of studies included in this review**

**Table 3.1: Categories and number of articles excluded from this review after primary, secondary, and full-text screening.**

| Reasons for exclusion | No. of articles |
|---|---|
| **Primary title and abstract screening** | |
| Not related to 4D MRI | 281 |
| Not related to radiotherapy | 103 |
| Not related to respiratory motion | 237 |
| Review papers | 74 |
| Abstract | 15 |
| **Total** | 710 |
| **Secondary title and abstract screening** | |
| MRgRT (on board) application | 89 |
| Orthogonal 2D cine | 60 |
| 4D sCT | 27 |
| Animals | 2 |
| 4D MRI in Lung patients | 41 |
| **Total** | 219 |
| **Tertiary full-text screening** | |
| Abdomen 4D MRI in volunteers or phantom only | 39 |
| **Total** | 39 |

*Abbreviation: computed tomography (CT); magnetic resonance imaging (MRI); four dimensional (4D); two dimensional (2D); magnetic resonance guided radiotherapy (MRgRT) and synthetic CT(sCT).*

### 3.3.2 4D MRI reconstructed from 3D MRI data acquisition

The systematic review identified 26 articles investigating 4D MRI reconstructed from 3D MRI data acquisition for abdominal radiotherapy [10-35]. An overview of 4D MRI techniques and imaging parameters used in these studies can be found in supplementary material B, along with the key findings (supplementary material C). The studies achieved various 3D spatial resolutions, with anisotropic voxel sizes ranging from 1.1 x 1.1 x 3 $mm^3$ to 3 x 3 x 5$mm^3$ [10, 13, 16, 18, 22, 23, 25-30, 32, 35], and isotropic voxel sizes ranging from 1.56 $mm^3$ to 3 $mm^3$ [11, 12, 14, 15, 17, 19, 21, 24, 31, 33, 34], with scan time ranging between 49.6 seconds to 9 minutes. Additionally, a few studies have reported the temporal resolution from RC-4D MRI, with values ranging from 300 ms to 500 ms [11, 12, 14, 19] with similar results was reported in TR-4D MRI [25, 28, 30, 32-34, 36]. Reconstruction time for 4D MRI techniques varied from 3 seconds to 10 hours [10, 19, 21, 24-26, 28, 32-34]. The patient cohort size reported ranged from 1-43 patients with different type of abdominal cancers (liver, pancreas, kidneys, and adrenal gland) [10-32]. Eight studies [12, 18, 19, 25-29] included a minimum sample size of 10 patients or more , while three studies [31, 34, 35] used a sample size exceeding 20 patients.

This review highlighted 13 studies that developed RC-4D MRI reconstruction, using self-gating as a motion surrogate technique for motion detection [11-15, 17-20, 22, 24, 28, 29]. Self-gating is solely an MRI-based approach, which relies on the MRI signal itself to quantify respiratory motion. Feng et al [13] developed a novel image reconstruction called (XD-GRASP) extra-Dimensional golden-angle radial MRI using compressed sensing. Five studies [14, 15, 19, 20, 24] investigated techniques aimed at improving the overall image quality of 4D MRI to achieve more accurate tumour delineation while preserving motion information. Other studies investigated different types of motion surrogates. Stemkens et al [10] used a 1D MRI navigator, while Navest et al [23] employed a noise navigator.

Limited studies have validated the accuracy of 4D MRI in comparison with 4D CT, as shown in supplementary material B [12, 18, 29]. Yang et al [12] showed the cross corelation (CC) in tumour motion was 0.91, with mean absolute difference (MAD) of 1.1 ±0.4 mm in superior inferior (SI) direction. While the

mean of standard deviation of absolute gross tumour volume (GTV) calculated from 10 breathing phases was a statistically significant reduction in 4D MRI. Oar et al [18] found the median difference between 4D CT and 4D MRI in tumour amplitude motion was 0.6 mm greater in 4D MRI. The only study that investigated dosimetric consequences was Thomas et al [29] who found statistical significant lower dosimetric coverage of planning target volume (PTV) obtained from 4D MRI compared to 4D CT when using a CT optimised plan. Specifically, the volume of the PTV receiving 90% of the prescribed dose was 76% in MR and 89% in CT ($p = 0.002$).

Other studies have validated 4D MRI using real-time 2D MRI [11, 12, 22], the results showed CC in tumour motion trajectories, with an approximate CC value of 0.93, with mean absolute differences (MAD) of $\leq 1$ mm in the SI direction [11, 12], and GTV motion was 10% less in 4D MRI [22]. In addition, four studies [11, 12, 18, 22] demonstrated the motion accuracy of 4D MRI against phantom studies.

Five studies investigated 3D real-time TR-4D MRI reconstruction by using motion models and deep learning (DL), aiming for enhancing 3D real-time quality while minimising acquisition and reconstruction times. Romaguera et al [27] developed a deep probabilistic motion model that predict volumetric images with a mean landmark error of $1.7 \pm 1.7$ mm in tested MRI data. Xiao et al [31] used a DL model to developed ultra-quality (UQ) 4D MRI reconstruction, with relative motion errors less than 1 mm in all directions. Liu et al [33] investigated prior-augmented implicit neural representation learning (NeRP model), achieved similar structure similarity index (SSIM) value of 0.98 and approximately less than 2.5 mm using tumour Hausdorff distance. Xiao et al [34] used downsampling-Invariant deformable registration (D2R model) to reconstructed high quality 4D MRI with relative region of interest (ROI) motion errors less than 2.7 mm to original 4D MRI. Lastly, Stemkens et al [16] demonstrated that intrafraction variation with the principal component analysis (PCA) model could lead to GTV underdosing and was more accurate, with an root mean square error (RMSE) of 1.09, outperforming other motion models.

Other methods directly obtain real-time 3D MRI by matching motion states learned offline with motion signatures acquired in real time (MRSIGMA) [25]. This method improved image quality of liver tumours and showed positive

linear correlation ($R^2$=0.94) compared to real-time 2D MRI. A similar technique called Live-view 4D GRASP MRI was demonstrated by Feng [32]. Another method acquired pseudo-3D real-time images through simultaneous 2D cine imaging in both sagittal and coronal planes, which were then reconstructed into isotropic resolution 4D MRI using a super-resolution technique [21]. Feng et al [25] and Mickevicius and Paulson [21] demonstrated the motion accuracy of 4D MRI against phantom studies.

Two studies developed DL 4D MRI reconstructions, Freedman et al [26] proposed deep radial convolutional neural network (4D-Dracula), which showed mean structural similarity index (SSIM) value of 0.9 and statistically insignificant median tumour motion differences of less than 2.4 mm compared to state of the art 4D reconstruction. Murray et al,[35] developed deep space–time-coil reconstruction network without k-space data consistency (Movienet), which showed similar multiscale-SSIM and mean square errors compared to XD-GRASP reconstruction.

### 3.3.3 4D MRI reconstructed from multislice 2D MRI data acquisition

The systematic review identified 13 articles investigating multi-slice 2D MRI data acquisition reconstructed into 4D MRI [36-48]. An overview of 4D MRI techniques and imaging parameters used in these studies can be found supplementary material D, and along with the key findings (supplementary material E). Through-plane spatial resolution ranged from 4-5 mm, with in-plane pixel sizes ranging from 0.78-1.9 mm². The acquisition time for the 4D MRI data ranged from 1.2-20 minutes [36, 39-42, 45]. Few studies have reported the temporal resolution and reconstruction time, with temporal resolution ranging from 180 ms to 333 ms [37, 40, 41, 44, 47]. Several methods for internal motion surrogates have been reported, mutual information (MI) [40], clustering method [44], body area (BA) [37, 38, 47], 1D navigator [36, 41, 42, 45], while one study reported external motion surrogate [39]. Meschini et al [44] reported varying reconstruction times based on respiratory surrogate methods; the MI method took 2 minutes [40, 44], while the k-clustering approach varied between 11 to 35 minutes [44]. The cohort size ranged from 1-36 patients with abdominal cancers [36-38, 40-48]. One study [48] included 13 patients while three studies [40, 42, 45] used a sample size exceeding 20 patients.

Limited studies have validated the accuracy of 4D MRI in comparison with 4D CT [36, 38, 45]. A study found a good agreement in mean tumour motion trajectories, with the range of CC between 0.93 to 0.98 [38]. The mean differences in GTV centroid motion were 0.7 (LR), 0.9 mm (AP), and 1.9 mm (SI) [45] and mean differences in tumour motion amplitude were 0.74 ± 0.0 mm (SI), 0.3 ± 0.1 mm (AP), and 0.2 ± 0.1 mm (RL) [38]. Other studies compared the target volume from the two modalities. Statistically significant reduction was found in GTV and internal target volume (ITV) in 4D MRI compared to 4D CT [45]. However, 4D MRI showed an increase in liver volume and in OAR (not specified) compared to 4D CT [45]. Moreover, the Dice similarity of ITV between 4D CT and 4D MRI was 92%-95% for the youngest patients with similar breathing characteristics and reduced (82%-88%) for other patients due to variation in breathing characteristics [36]. Uh et al [36, 41] demonstrated the accuracy of 4D MRI in phantom studies.

Other studies have validated 4D MRI using real-time 2D MRI [37, 38, 41, 48]. The CC ranged from 0.98 to 0.99, with mean differences in motion amplitude between less than 1mm [38], and MAD in tumour motion magnitude in all direction ranged from 1.1 to 2.1 mm [37]. The MAD in diaphragm motion magnitude was found to be smaller using a diaphragm navigator compared to 2D MRI, which ranged from 0.7 to 1.8 mm in AP direction [41]. Respiratory correlated MRI fingerprinting (MRF) was assessed as a method of 4DMRI, with mean difference in motion between 2D MRI and 4D MRF of 1.5 ± 1.1 mm SI and 0.8 ± 0.6 mm AP, with mean Pearson correlation coefficient (PCC) 0.95 ± 0.05 SI and 0.93 ± 0.09 AP[48]. Five studies [37, 39, 43, 44, 47] demonstrated the motion accuracy of 4D MRI against phantom studies.

## 3.4 Discussion

This systematic review evaluates the current literature on 4D MRI used in patients undergoing abdominal radiotherapy. It highlights the potential benefits of 4D MRI in the planning stage. The key findings drawn from this systematic review are as follows: (1) 4D MRI has the potential to improve abdominal radiotherapy treatment planning for patients by providing more accurate tumour definition and motion assessment compared to 4D CT. However, it would be recommended to validate 4D MRI using both 4D CT and phantoms for a robust and comprehensive assessment. (2) 4D MRI reconstructed from 3D MRI

acquisition shows promise as a feasible approach for motion management in abdominal radiotherapy planning in terms of spatial resolution. (3) large slice thickness currently achieved on 4D MRI reconstructed from multi-slice 2D acquisition is unsuitable for clinical purposes. (4) The current barriers for clinical implementation of 4D MRI in radiotherapy are the limited availability of validated commercial solutions and the lack of larger patient cohort studies that directly compare it to 4D CT. These comparisons are essential to highlight the potential clinical benefits of 4D MRI, particularly concerning target volume delineation and radiotherapy plan optimisation.

Several studies developed 4D MRI reconstructed from 3D acquisition that met some technical requirements for use in radiotherapy protocols. The recommended MRI image parameters for clinical implementation in radiotherapy require a spatial resolution of ≤ 1 mm and slice thickness of < 3 mm [9]. However, acquiring a 1 mm spatial resolution in MRI results in long scan times from a clinical standpoint. Scan time remains a challenge in most 4D MRI techniques. Therefore, there currently is a trade-off between spatiotemporal resolution and scan time due to MRI scanner constraints. High spatial resolutions of approximately 1x1x3 $mm^3$ have been achieved [13, 18, 23, 26, 29] with scan time varying from less than 2 minutes to 10 minutes. However, Feng et al [13] and Oar et al [18], Freedman et al [26], who were able to obtain short scan time of around 5 minutes or less with high spatial resolution. Another technical consideration is the choice of the number of bins, which varies with each method. Increasing the number of bins to match the 10 used in 4D CT could potentially increase both the reconstruction burden and the issues related to undersampling.

Meanwhile, 4D image reconstruction times have not been thoroughly reported. 4D reconstruction requires processing large amount of data, complex reconstruction algorithms and adequate hardware such as processing power, memory, and storage. All of these can be optimised to reduce reconstruction times to a clinically acceptable level. Ideally, near real time would be acceptable clinically because it is important to ensure the quality of the 4D MRI before the patient leaves the scanner or hospital. If any artefacts or errors are detected, it is more efficient to repeat the scan immediately rather than calling the patient back for a repeat scan later. This will ensure the best patient

experience and enhances the efficiency of the radiotherapy department. Future developments in MRI technology could get around these constraints by reducing scan and reconstruction times using cutting-edge methods such compressed sensing [13, 49, 50], SMS [21, 51], or DL reconstruction [26, 33-35, 52]. The application of DL reconstruction has shown promise with a reconstruction time of around 3s [34], 28s [26], and 0.73s [35]. However, DL methods are still in the early stages of validation, and this need further investigation to be used in clinical settings [26, 33-35].

Several studies attempted to reconstruct 4D MRI from multislice 2D MRI acquisition using retrospective or prospective sorting, which involves acquiring multiple 2D MRI slices to reconstruct 3D volumes, and then binning them into respiratory phases or amplitude bins. Different internal motion surrogates have been proposed [36-38, 40-47] and the advantages of using internal motion surrogates over external motion surrogates have been demonstrated [39]. These advantages include simplified equipment setup, enhanced image quality, improved synchronisation with image acquisition, and a more reliable representation of internal structures. Regardless of the motion surrogates used [36-38, 40-48], all of the reported methods obtained a relatively large slice thickness of around 5 mm. This slice thickness is inadequate for accurate treatment planning purposes, which require < 3mm [9]. Therefore, it is crucial to consider optimising the acquisition parameters to achieve thinner slice thickness with no slice gap. Another consideration is that high spatial and temporal resolutions require a longer scan time to collect sufficient data for reconstruction. Significant reduction in scan time have been achieved by Chen et al [45] with 5 minutes scan times using a 1D navigator, while the MI method allowed similar image quality with a reduced scan acquisition time of 1.2 minutes [40].

For both 3D or multislice 2D MRI acquisitions used to reconstruct 4D MRI, the common image contrast is typically obtained from T2/T1w GRE and T1w GRE sequences. This choice is primarily made to achieve high spatiotemporal resolution. However, it is important to note that T2w 4D MRI has been explored in multislice 2D MRI sequences [36, 39, 43, 45]. Nevertheless, it still faces challenges for clinical implementation, particularly due to the relatively large slice thickness of 5 mm. On the other hand, employing T2 3D MRI

sequences requires a longer acquisition time and remains a challenge in the context of 4D MRI.

Another important technical concern in using MRI for radiotherapy is geometric distortion. This review revealed that there is a lack of research investigating the potential geometric distortions in abdominal 4D MRI techniques. Geometric distortion can compromise the spatial accuracy of MRI, which is particularly crucial for tumour localisation in radiotherapy. Solutions for reducing geometric distortion such as post processing geometric distortion correction algorithms are essential [9]. For most radiotherapy applications, a residual distortion errors of 2 mm considered acceptable. The 4D phantom study demonstrated geometric accuracy up to 1.31 mm [53] , another study reported maximum of 2.5 mm error [54]. Therefore, future studies should test the reliability of geometric distortions in 4D MRI acquisition methods in patients and develop strategies for addressing potential distortions in order to use these methods for clinical use in radiotherapy planning.

There are several ways to validate 4D MRI, each with its own limitation. Firstly, phantoms are more controlled with predefined motion, allowing for a direct comparison between the expected and measured movement. However, phantoms simplify the complexity and variability of human anatomy and physiology as well as not precisely replicating the characteristics of human tissues and thus results may not be directly translatable to patient results. Secondly, real-time 2D MRI provides immediate imaging of motion on the same MR scan position and time, however it might not represent the full 3D motion. Lastly, 4D CT is commonly used in clinical practice for evaluating respiratory motion in radiotherapy, but it lacks contrast for abdominal tumours, often making them invisible which limits the usefulness of comparison in the region of the tumour. Additionally, external motion surrogates don't accurately match the actual motion of tumours and internal organs. Therefore, combining multiple validation methods to overcome individual limitations is desirable to achieve a comprehensive motion accuracy assessment. Several studies have validated motion accuracy of 4D MRI techniques in patients against 4D CT and phantoms [12, 18] and real-time 2D MRI and phantoms [10, 12, 22, 25, 37]. Yet, a lack of validation against 4D CT and phantoms is notable. Whereas a few studies validated 4D MRI motion accuracy in patients against either 4D CT [36, 45] or

real-time 2DMRI [38, 41, 48], However, it would be recommended to ensure a robust and comprehensive validation of 4D MRI using both 4D CT and phantoms. Firstly, phantoms allow direct, accurate, and reusable measurement comparisons, which confirm that all technological components of the 4D MRI are working optimally. Secondly, 4D CT has been widely accepted as a clinical standard to evaluate respiratory motion, thus, a reliable benchmark is provided by comparing 4D MRI to 4D CT in patient data. It is beneficial to understand how 4D MRI relates to what is currently accepted. By integrating both in the validation process, researchers can ensure both technical precision and clinical relevance of the results, which ultimately leads to increased levels of confidence in the use of 4D MRI in clinical settings.

Regardless of the 4D MRI reconstruction methods using 3D or multislice 2D MRI acquisitions, 4D MRI motion accuracy showed high agreement in tumour motion pattern compared to 4D CT and real-time 2D MRI, especially in the SI direction, however moderate correlation in the other direction. This could be due to the hysteresis effect. Several studies have demonstrated the presence of hysteresis in motion using 3D motion model trajectories [10, 11, 16, 27]. However, this hysteresis effect is often underestimated when using respiratory belts in 4D CT, as the signal does not accurately represent the internal motion of the tumour [17]. On the other hand, 2D MRI captures motion in only one direction, which limits the understanding of hysteresis motion. Thomas et al [29] demonstrated that the two-directional binning method revealed an additional displacement of at least 3 mm of anterior motion, due to hysteresis effects. Therefore, 4D MRI has a greater potential for reliable motion evaluation, owing to its unique feature of using internal motion surrogates, which can enhance the accuracy in tracking tumour motion.

A small number of studies reported differences in target volumes between 4D MRI and 4D CT. 4D MRI showed a reduced GTV and ITV compared to 4D CT [36, 38, 45] which is hypothesised to be due to MRI's superior soft tissue contrast compared to CT. Traditional radiation treatment planning uses 4D CT scans to estimate GTV-ITV margins for abdominal patients, but this method is over-conservative as tumours are not always visible on CT so structures like the liver wall that can be visualised in both images must be used as a surrogate. This leads to uncertainty and consequently, oncologists

use larger margins to avoid under-treatment of targets, which exposes healthy tissue to higher radiation doses than necessary. 4D MRI, by contrast, provides clear visualisation of tumours and their motion, allowing for more accurate and precise ITV definition. This is hypothesised to result in smaller treatment volumes, minimising radiation to healthy tissue and potentially reducing patient toxicity due to the treatment. A single study conducted a comparative assessment of target volumes and plan dosimetry optimisation between 4D CT and 4D MRI [29]. The study highlighted that when optimising treatment plans based on PTVs derived from 4D CT there was a statistically significant lower dosimetric coverage of PTVs derived on MRI. Therefore, the failure to incorporate PTVs derived from 4D MRI in the planning process may lead to suboptimal dosing of the actual PTV. However, it is crucial to validate 4D MRI before use in order to accurately capture both motion and volume, hence enhancing the accuracy of treatment planning. 4D MRI has the potential to enhance the coverage of prescribed radiation doses to target volumes, while minimising the radiation exposure to surrounding healthy tissues. Yet, drawing a definitive conclusion can be challenging when limited studies in the literature compare dosimetric assessment with 4D CT plan.

4D MRI reconstructed from multislice 2D and 3D acquisition demonstrated similar accuracy. However, their inherent differences must be taken into consideration. Although they showed similar tumour motion accuracy, their clinical advantages over 4D CT have not been thoroughly investigated. The current studies focused on the differences in motion amplitude between 4D CT and 4D MRI, instead of exploring the possible clinical benefits of 4D MRI compared to 4D CT such as tumour volume changes and treatment plan differences due to this change. 4D MRI reconstructed from 3D acquisition appears more promising for use in radiotherapy, providing acquisitions closer to the clinical specifications. However, the majority of the studies included small patient’s cohorts, which limited the generalisability. Furthermore, patient validation requires further investigation using a larger cohort. It is hypothesised that larger cohort studies have not been presented so far in the literature due to the limited availability of validated commercial solutions for 4D MRI for RT from vendors, as well as the rarity of abdominal cancers, such as in the liver and pancreas, making large cohort studies more challenging.

Future work should focus on optimising the parameters of multi-slice 2D MRI to meet the specific needs of treatment planning. Furthermore, comparing dosimetric plans derived from 4D MRI and 4D CT could reveal the clinical advantages of each modality. It is also important for MRI vendors to support these advancements in 4D MRI and ensure its validation for clinical use. Currently, all these developments are institution-based as there are limited commercial solutions available for clinical implementation. To the best of our knowledge, Siemens has a product designed for 4D MRI in RT [55]. However, more studies are needed to validate this product in larger patient cohorts. Additionally, an important consideration is the need for standardisation of both quantitative and qualitative metrics among different studies. This is essential to facilitate future research to perform more comprehensive comparisons. Currently, the diverse methods and metrics used across different studies pose a challenge to drawing reliable and valid conclusions to guide 4D MRI for clinical implementation.

This review is not without limitations. Primarily, the screening was conducted by a sole reviewer, the scope of the articles was limited to papers written in English, and therefore introducing an element of selection bias. Next, the author also excluded studies involving phantoms or volunteers only. Instead, the review was exclusive to the assessment of clinical validation in actual patients. Finally, studies related to developing 4D MRI for online MRgRT were excluded since their primarily focus is on adaptation and tumor tracking. However, more centres have access to MR simulation and therefore the goal of this study was to evaluate treatment planning options rather than to guide treatments online.

## 3.5 Conclusion

4D MRI has continuously evolved and improved over the years, which may support the growing interest in implementing an MRI-only pathway for enhancing abdominal radiotherapy treatment planning. It potentially offers advantages over 4D CT, such as reduced tumour margins and sparing healthy tissue. However, standards and guidelines were needed to ensure the consistency and reliability of these clinical benefits. While 4D MRI reconstructed from 3D MRI acquisitions was feasible for clinical implementation, 4D MRI reconstructed from multislice 2D MRI is not currently clinically acceptable due to

unsuitable through-plane resolution. The development of the reported techniques has focused on research applications, highlighting the need for validated commercial solutions.

## 3.6 References


[1] Brandner E, Chetty I, Giaddui T, Xiao Y, Huq M. Motion management strategies and technical issues associated with stereotactic body radiotherapy of thoracic and upper abdominal tumors: A review from NRG oncology. Med Phys. 2017;44:2595-612. https://doi.org/10.1002/mp.12227.

[2] Antony R, Lonski P, Ungureanu E, Hardcastle N, Yeo A, Siva S, et al. Independent review of 4DCT scans used for SABR treatment planning. Appl Clin Med Phys. 2020;21:62-7. https://doi.org/10.1002/acm2.12825.

[3] Mittauer K, Paliwal B, Hill P, Bayouth JE, Geurts MW, Baschnagel AM, et al. A new era of image guidance with magnetic resonance-guided radiation therapy for abdominal and thoracic malignancies. Cureus. 2018;10. https://doi.org/10.7759/cureus.2422. .

[4] Yamamoto T, Langner U, Loo BW, Jr., Shen J, Keall PJ. Retrospective analysis of artifacts in four-dimensional CT images of 50 abdominal and thoracic radiotherapy patients. Int J Radiat Oncol Biol Phys. 2008;72:1250-8. https://doi.org/10.1016/j.ijrobp.2008.06.1937.

[5] Stemkens B, Paulson ES, Tijssen RHN. Nuts and bolts of 4D-MRI for radiotherapy. Phys Med Biol. 2018;63:21TR01. https://doi.org/10.1088/1361-6560/aae56d.

[6] Paganelli C, Whelan B, Peroni M, Summers P, Fast M, van de Lindt T, et al. MRI-guidance for motion management in external beam radiotherapy: current status and future challenges. Phys Med Biol. 2018;63:22tr03. https://doi.org/10.1088/1361-6560/aaebcf.

[7] Li G, Liu Y, Nie X. Respiratory-Correlated (RC) vs. Time-Resolved (TR) Four-Dimensional Magnetic Resonance Imaging (4DMRI) for Radiotherapy of Thoracic and Abdominal Cancer. Front Oncol. 2019;9:1024. https://dx.doi.org/10.3389/fonc.2019.01024.

[8] Moher D, Liberati A, Tetzlaff J, Altman DG, Group. P. Preferred Reporting Items for Systematic Reviews and Meta-Analyses: The PRISMA Statement. Annals of internal medicine. 2009;151:264-9. https://doi.org/10.1371/journal.pmed.1000097.

[9] Speight R, Dubec M, Eccles CL, George B, Henry A, Herbert T, et al. IPEM topical report: guidance on the use of MRI for external beam radiotherapy treatment planning. Phys Med Biol. 2021; 66:055025. https://doi.org/10.1088/1361-6560/abdc30.

[10] Stemkens B, Tijssen RH, de Senneville BD, Heerkens HD, van Vulpen M, Lagendijk JJ, et al. Optimizing 4-dimensional magnetic resonance imaging data sampling for respiratory motion analysis of pancreatic tumors. Int J Radiat Oncol Biol Phys. 2014;91:571-8. https://doi.org/10.1016/j.ijrobp.2014.10.050.

[11] Deng Z, Pang J, Yang W, Yue Y, Sharif B, Tuli R, et al. Four-dimensional MRI using three-dimensional radial sampling with respiratory self-gating to characterize temporal phase-resolved respiratory motion in the abdomen. Magn Reson Med. 2015;75:1574-85. https://doi.org/10.1002/mrm.25753.

[12] Yang W, Fan Z, Tuli R, Deng Z, Pang J, Wachsman A, et al. Four-dimensional magnetic resonance imaging with 3-dimensional radial sampling and self-gating–based K-space sorting: early clinical experience on pancreatic cancer patients. Int J Radiat Oncol Biol Phys. 2015;93:1136-43. https://doi.org/10.1016/j.ijrobp.2015.08.028.

[13] Feng L, Axel L, Chandarana H, Block KT, Sodickson DK, Otazo R. XD-GRASP: Golden-angle radial MRI with reconstruction of extra motion-state dimensions using compressed sensing. Magn Reson Med. 2016;75:775-88. https://doi.org/10.1002/mrm.25665.

[14] Jin J, McKenzie E, Fan Z, Tuli R, Deng Z, Pang J, et al. Nonlocal means denoising of self-gated and k-space sorted 4-dimensional magnetic resonance imaging using block-matching and 3-dimensional filtering: implications for pancreatic tumor registration and segmentation. Int J Radiat Oncol Biol Phys. 2016;95:1058-66. https://doi.org/10.1016/j.ijrobp.2016.02.006.

[15] Deng Z, Yang W, Pang J, Bi X, Tuli R, Li D, et al. Improved vessel–tissue contrast and image quality in 3D radial sampling-based 4D-MRI. J Appl Clin Med Phys. 2017;18:250-7. https://doi.org/10.1002/acm2.12194.

[16] Stemkens B, Glitzner M, Kontaxis C, De Senneville BD, Prins FM, Crijns SP, et al. Effect of intra-fraction motion on the accumulated dose for free-breathing MR-guided stereotactic body radiation therapy of renal-cell carcinoma. Phys Med Biol. 2017;62:7407. https://doi.org/10.1088/1361-6560/aa83f7.

[17] Breuer K, Meyer CB, Breuer FA, Richter A, Exner F, Weng AM, et al. Stable and efficient retrospective 4D-MRI using non-uniformly distributed quasi-random numbers. Phys Med Biol. 2018;63:075002. http://dx.doi.org/10.1088/1361-6560/aab342.

[18] Oar A, Liney G, Rai R, Deshpande S, Pan L, Johnston M, et al. Comparison of four dimensional computed tomography and magnetic resonance imaging in abdominal radiotherapy planning. Phys Imaging Radiat Oncol. 2018;7:70-5. https://dx.doi.org/10.1016/j.phro.2018.09.004.

[19] Yang W, Fan Z, Deng Z, Pang J, Bi X, Fraass BA, et al. Novel 4D-MRI of tumor infiltrating vasculature: Characterizing tumor and vessel volume motion for selective boost volume definition in pancreatic radiotherapy 11 Medical and Health Sciences 1112 Oncology and Carcinogenesis. Radiat Oncol. 2018;13:1-8. https://doi.org/10.1186/s13014-018-1139-2.

[20] Deng Z, Pang J, Lao Y, Bi X, Wang G, Chen Y, et al. A post-processing method based on interphase motion correction and averaging to improve image quality of 4D magnetic resonance imaging: A clinical feasibility study. Brit J Radiol. 2019;92:20180. https://doi.org/10.1259/bjr.20180424.

[21] Mickevicius NJ, Paulson ES. Simultaneous acquisition of orthogonal plane cine imaging and isotropic 4D-MRI using super-resolution. Radiother Oncol. 2019;136:121-9. https://dx.doi.org/10.1016/j.radonc.2019.04.005.

[22] Stemkens B, Prins FM, Bruijnen T, Kerkmeijer LG, Lagendijk JJ, Van den Berg CA, et al. A dual-purpose MRI acquisition to combine 4D-MRI and dynamic contrast-enhanced imaging for abdominal radiotherapy planning. Phys Med Biol. 2019;64:06NT2. https://doi.org/10.1088/1361-6560/ab0295.

[23] Navest R, Mandija S, Bruijnen T, Stemkens B, Tijssen R, Andreychenko A, et al. The noise navigator: a surrogate for respiratory-correlated 4D-MRI for motion characterization in radiotherapy. Phys Med Biol. 2020;65:01NT2. https://doi.org/10.1088/1361-6560/ab5c62.

[24] Weick S, Breuer K, Richter A, Exner F, Strohle SP, Lutyj P, et al. Non-rigid image registration of 4D-MRI data for improved delineation of

moving tumors. BMC Med Imag. 2020;20:10. https://doi.org/10.1186/s12880-020-00439-6.

[25] Feng L, Tyagi N, Otazo R. MRSIGMA: Magnetic Resonance SIGnature MAtching for real-time volumetric imaging. . Magn Reson Med. 2020;84:1280–92. https://doi.org/10.1002/mrm.28200.

[26] Freedman JN, Gurney-Champion OJ, Nill S, Shiarli A-M, Bainbridge HE, Mandeville HC, et al. Rapid 4D-MRI reconstruction using a deep radial convolutional neural network: Dracula. Radiat Oncol. 2021;159:209-17. https://doi.org/10.1016/j.radonc.2021.03.034.

[27] Romaguera LV, Mezheritsky T, Mansour R, Carrier J-F, Kadoury S. Probabilistic 4D predictive model from in-room surrogates using conditional generative networks for image-guided radiotherapy. Med Image Anal. 2021;74:102250. https://doi.org/10.1016/j.media.2021.102250.

[28] Mansour R, Romaguera LV, Huet C, Bentridi A, Vu K-N, Billiard J-S, et al. Abdominal motion tracking with free-breathing XD-GRASP acquisitions using spatio-temporal geodesic trajectories. MBEC. 2022;60:583-98. https://doi.org/10.1007/s11517-021-02477-w.

[29] Thomas HR, Miao X, Ferguson D, Calvin C, Bhaskar Krishnamurthy U, Anwar M, et al. Contrast-enhanced 4D-MRI for internal target volume generation in treatment planning for liver tumors. Radiat Oncol. 2022;173:69-76. https://doi.org/10.1016/j.radonc.2022.05.037.

[30] Wong OL, Law MWK, Poon DMC, Yung RWH, Yu Sk, Cheung Ky, et al. A pilot study of respiratory motion characterization in the abdomen using a fast volumetric 4D-MRI for MR-guided radiotherapy. Precis Radiat Oncol. 2022;6:100-9. https://doi.org/10.1002/pro6.1153.

[31] Xiao H, Ni R, Zhi S, Li W, Liu C, Ren G, et al. A dual-supervised deformation estimation model (DDEM) for constructing ultra-quality 4D-MRI based on a commercial low-quality 4D-MRI for liver cancer radiation therapy. Med Phys. 2022;49:3159-70. https://dx.doi.org/10.1002/mp.15542.

[32] Feng L. Live-view 4D GRASP MRI: A framework for robust real-time respiratory motion tracking with a sub-second imaging latency. Magn Reson Med. 2023;90 1053-68. https://dx.doi.org/10.1002/mrm.29700.

[33] Liu LL, Shen LY, Johansson A, Balter JM, Cao Y, Vitzthum L, et al. Volumetric MRI with sparse sampling for MR-guided 3D motion tracking via sparse prior-augmented implicit neural representation learning. Med Phys. 2023;51:2526-37. https://doi.org/10.1002/mp.16845.

[34] Xiao HN, Han XY, Zhi SH, Wong YL, Liu CY, Li W, et al. Ultra-fast multi-parametric 4D-MRI image reconstruction for real-time applications using a downsampling-invariant deformable registration (D2R) model. Radiat Oncol. 2023;189:109948. https://doi.org/10.1016/j.radonc.2023.109948.

[35] Murray V, Siddiq S, Crane C, El Homsi M, Kim T-H, Wu C, et al. Movienet: Deep space–time-coil reconstruction network without k-space data consistency for fast motion-resolved 4D MRI. J Magn Reson. 2024;91:600-14. https://doi.org/10.1002/mrm.29892.

[36] Uh J, Kadbi M, Hua CH. Effects of age-related breathing characteristics on the performance of four-dimensional magnetic resonance imaging reconstructed by prospective gating for radiation therapy planning. Phys Imaging Radiat Oncol. 2019;11:82-7. http://dx.doi.org/10.1016/j.phro.2019.09.004.

[37] Liu YL, Yin FF, Chang Z, Czito BG, Palta M, Bashir MR, et al. Investigation of sagittal image acquisition for 4D-MRI with body area as respiratory surrogate. Med Phys. 2014;41:13. https://doi.org/10.1118/1.4894726.

[38] Yang J, Cai J, Wang HJ, Chang Z, Czito BG, Bashir MR, et al. Four-Dimensional Magnetic Resonance Imaging Using Axial Body Area as Respiratory Surrogate: Initial Patient Results. Int J Radiat Oncol Biol Phys. 2014;88:907-12. https://doi.org/10.1016/j.ijrobp.2013.11.245.

[39] Glide-Hurst CK, Kim JP, To D, Hu Y, Kadbi M, Nielsen T, et al. Four dimensional magnetic resonance imaging optimization and implementation for magnetic resonance imaging simulation. Pract Radiat Oncol. 2015;5:433-42. http://dx.doi.org/10.1016/j.prro.2015.06.006.

[40] Chiara P, SUMMERS P, MASSIMO B, GUIDO B, MARCO R. Liver 4DMRI: A retrospective image-based sorting method. Med Phys. 2015;42:4814-21. https://doi.org/10.1118/1.4927252.

[41] Uh J, Khan MA, Hua C. Four-dimensional MRI using an internal respiratory surrogate derived by dimensionality reduction. Phys Med Biol. 2016;61:7812. https://doi.org/10.1088/0031-9155/61/21/7812.

[42] Uh J, Krasin MJ, Li Y, Li X, Tinkle C, Lucas JT, et al. Quantification of Pediatric Abdominal Organ Motion With a 4-Dimensional Magnetic Resonance Imaging Method. Int J Radiat Oncol Biol Phys. 2017;99:227-37. http://dx.doi.org/10.1016/j.ijrobp.2017.05.026.

[43] van Kesteren Z, van der Horst A, Gurney-Champion OJ, Bones I, Tekelenburg D, Alderliesten T, et al. A novel amplitude binning strategy to handle irregular breathing during 4DMRI acquisition: improved imaging for radiotherapy purposes. Radiat Oncol. 2019;14:80. https://dx.doi.org/10.1186/s13014-019-1279-z.

[44] Meschini G, Paganelli C, Gianoli C, Summers P, Bellomi M, Baroni G, et al. A clustering approach to 4D MRI retrospective sorting for the investigation of different surrogates. Phys Medica. 2019;58:107-13. https://doi.org/10.1016/j.ejmp.2019.02.003.

[45] Chen Y, Gong G, Wang Y, Liu C, Su Y, Wang L, et al. Comparative Evaluation of 4-Dimensional Computed Tomography and 4-Dimensional Magnetic Resonance Imaging to Delineate the Target of Primary Liver Cancer. Technology in Cancer Research & Treatment 2021;20:15330338211045499. https://doi.org/10.1177/15330338211045499.

[46] Meschini G, Paganelli C, Vai A, Fontana G, Molinelli S, Pella A, et al. An MRI framework for respiratory motion modelling validation. JMIRO. 2021;65:337-44. https://doi.org/10.1111/1754-9485.13175.

[47] Zhang L, Yin FF, Li T, Teng XZ, Xiao HN, Harris W, et al. Multi-contrast four-dimensional magnetic resonance imaging (MC-4D-MRI): Development and initial evaluation in liver tumor patients. Med Phys. 2021;48:7984-97. https://doi.org/10.1002/mp.15314.

[48] Liu C, Li T, Cao P, Hui ES, Wong YL, Wang Z, et al. Respiratory-Correlated 4-Dimensional Magnetic Resonance Fingerprinting for Liver Cancer Radiation Therapy Motion Management. Int J Radiat Oncol Biol Phys. 2023;117:493-504. https://dx.doi.org/10.1016/j.ijrobp.2023.04.015.

[49] Feng L, Benkert T, Block KT, Sodickson DK, Otazo R, Chandarana H. Compressed sensing for body MRI. J Magn Reson Imaging. 2017;45:966-87. https://doi.org/10.1002/jmri.25547.

[50] Yoon JH, Nickel MD, Peeters JM, Lee JM. Rapid imaging: recent advances in abdominal MRI for reducing acquisition time and its clinical applications. KJR. 2019;20:1597-615. https://doi.org/10.3348/kjr.2018.0931.

[51] Barth M, Breuer F, Koopmans PJ, Norris DG, Poser BA. Simultaneous multislice (SMS) imaging techniques. Magn Reson Med. 2016;75:63-81. https://doi.org/10.1002/mrm.25897.

[52] Liang D, Cheng J, Ke Z, Ying L. Deep MRI Reconstruction: Unrolled Optimization Algorithms Meet Neural Networks. ArXiv. 2019. https://doi.org/10.48550/arXiv.1907.11711.

[53] Schneider S, Dolde K, Engler J, Hoffmann A, Pfaffenberger A. Commissioning of a 4D MRI phantom for use in MR-guided radiotherapy. Med Phys. 2019;46:25-33. https://doi.org/10.1002/mp.13261.

[54] Kavaluus H, Koivula L, Salli E, Seppälä T, Saarilahti K, Tenhunen M. Motion modeling from 4D MR images of liver simulating phantom. J Appl Clin Med Phys. 2022;23:e13611. https://doi.org/10.1002/acm2.13611.

[55] Siemens-healthineers. 4D MRI – RT Respiratory Self-Gating: Siemens; 2023 [Available from: https://www.siemens-healthineers.com/en-uk/magnetic-resonance-imaging/options-and-upgrades/clinical-applications/4d-mri.

# Chapter 4 Evaluating the dosimetric and positioning accuracy of a deep learning-based synthetic-CT generation model for liver radiotherapy

**Chapter note:** Initial results from this chapter were presented as a poster at MRinRT 2024. The completed work was later presented as an oral presentation at BIR 2025 (see Appendix C). This chapter has been published in *Biomedical Physics & Engineering Express 2025;11: 035014. https://doi.org/10.1088/2057-1976/adc818.*

## Abstract

**Background and purpose:** An MRI-only workflow requires synthetic computed tomography (sCT) images to enable dose calculation. This study evaluated the dosimetric and patient positioning accuracy of deep learning-generated sCT for liver radiotherapy.

**Methods and materials:** sCT images were generated for eleven patients using a CycleGAN algorithm. Clinical volumetric modulated arc treatment plans (VMAT) were calculated on CT and recalculated on sCT, and dose differences were assessed using dose volume histogram (DVH). For position verification, the sCT images were validated as reference images to 4D cone beam computed tomography (4D CBCT) by calculating the translational and rotational differences between sCT and CT registrations to 4D CBCT.

**Results:** The relative mean dose differences for the planning target volume (PTV) and organs at risk (OAR) between the CT and sCT plans were 0.0% and < 0.5% respectively. For positioning verification, the systematic translational and rotational differences were < 0.5 mm and < 0.5° respectively in all directions

**Conclusion:** This is the first study to validate a sCT model for liver cancer in terms of both dosimetry and patient positioning, marking a significant step in demonstrating the feasibility of an MRI-only workflow for treating liver cancer. The generated sCT showed dosimetric differences within clinically acceptable levels and was successfully used as reference images for treatment position

verification. This CycleGAN model is accessible through the research version of a commercial vendor, with potential for development as a clinical solution.

**Keywords:** MRI-only radiotherapy treatment planning; dosimetric accuracy; liver radiotherapy; patients positioning accuracy; synthetic-CT; Artificial intelligence.

## 4.1 Introduction

Stereotactic ablative radiotherapy (SABR) is a commonly used technique for treating liver cancer [1]. It is a viable treatment option for unresectable liver cancer such as hepatocellular carcinoma (HCC) [2, 3] and liver metastasis [4, 5]. SABR delivers precise, focused doses of radiation to tumours while minimising exposure to healthy surrounding tissues. Thus, it demands precise planning to ensure tumour coverage and minimise harm to normal tissues. Currently, computed tomography (CT) is the standard modality for patient simulation, treatment planning and as a reference for treatment delivery, given its superior geometric information. However, CT often provides poor contrast in liver images, leading to the need for magnetic resonance imaging (MRI) to accurately delineate tumours. The current treatment planning process involves transferring target contours from MRI to CT through image registration, which is challenging and introduces uncertainties due to differences in patient setup, respiratory motion, and internal movement.

Recently there has been a growing interest in the MRI-only workflow among many radiotherapy centres, with the aim of eliminating CT from the treatment planning process. MRI-only workflows have been successfully implemented in pelvis and brain treatments [6-9]. This approach includes generating synthetic CT (sCT) images from MRI scans for radiation dose calculations, treatment planning and delivery. This is because MRI images alone do not provide the required electron density information for treatment planning, which has led to the investigation of various sCT methods in the literature. These methodologies can be categorised into non-deep learning [10] and deep learning methods [11, 12], with the latter having proven promising results. Some sCT generation methods have also been incorporated into commercial solutions for brain, pelvis, head and neck regions [13-17]. However, the adoption of an MRI-only workflow for liver radiotherapy is still in its early

stages due to various challenges. Generating accurate sCT images based on deep learning models relies on the quality of the training data. Liver MRI scans are typically acquired using short breath-hold sequences, which significantly limits their image quality compared to scans in the pelvis, head and neck, or brain, where scans can take minutes. Additional issues can occur due to variations in internal anatomical motion and air pockets. As a result, these challenges lead to poor-quality data for training deep learning models. Another impediment is the requirement for 4D MRI to capture liver motion information during simulation stage, rather than 4D CT, which is not yet widely implemented in practice and is still in the development stage [18].

Several promising approaches have evaluated sCT generation for their geometric and dosimetric accuracy in the abdomen [19-28]. sCT models demonstrated dosimetric accuracy within the clinically acceptable level of ±2%, with mean PTV dose differences reported as 0.9% [27] 0.4% [28], -0.5% [21], 0.8% [22] <1% [24]. However, these models were research-only algorithms, so implementing them clinically would be difficult. To the best of our knowledge, this paper is the first to assess dosimetric and positioning accuracy in sCT generation for liver radiotherapy using a deep learning model developed by a commercial company (RayStation Laboratories) with potential for development as a clinical solution. It is important to note that this is the first paper evaluating the patient position verification of a deep learning-based synthetic-CT generation model for liver radiotherapy treatment planning. The same model has been applied in the brain, pelvis, and head and neck, achieving dosimetric accuracy of less than 2% for each site and various site-specific MRI sequences [29]. However, the sCT generated has not been validated for positioning accuracy.

## 4.2 Methods and materials

### 4.2.1 Patient cohort and image acquisition

Ethical approval was granted under the Leeds East Research Ethics Committee (REC) (reference: 19/YH/0300; IRAS project ID: 255585) for the retrospective analysis of 47 liver cancer patients who had undergone volumetric modulated arc therapy (VMAT) external beam radiotherapy at our centre. Each patient underwent CT followed by MRI simulation typically within 2 hours. All

image acquisitions were in the radiotherapy treatment position in a patient specific vac bag, abdominal compression, and 250 ml of water taken orally.

3DCT images were acquired in end-exhale breath-hold on a Philips Brilliance Big Bore (Philips Healthcare, Amsterdam, Netherlands) at 120 KVp, and 107 mA with 1.1x1.1x2 $mm^3$ resolution. The liver planning target volume (PTV) and organ at risk (OAR) shown in the table 1 were delineated on CT scans by oncologists according to department protocol before being used in this study. In addition, liver target volumes are produced with the motion information of the tumour from 4D CT.

3D MR images were acquired using end-exhale breath-hold T1-weighted volumetric interpolated breath-hold examination (VIBE) sequences on a Siemens Aera 1.5 T(Siemens Healthineers, Erlangen, Germany) with 1.2x1.2x2.5 $mm^3$ resolution, 400 mm FOV, $20^o$ flip angle, (repetition time TR= 3.04 ms, echo time TE= 1.22 ms), and Bandwidth (480 Hz/Px). Image acquisition time was about 17 seconds. All patients were injected with a liver-specific contrast agent (Primovist), which allows the imaging of dynamic contrast enhancement of four phases (arterial, venous, late venous and delayed images).

4D cone beam computed tomography (4DCBCT) images were acquired during free breathing on an ELEKTA X-ray volume imaging (XVI) software (Elekta, Stockholm, Sweden) with a resolution of 1.2 × 1.2 × 2 $mm^3$ at 120 kVp and 32 mA. Liver patients receive 5 fractions, with a day 0 for patient setup. The number of 4D CBCT scans obtained per patient ranges from 12 to 20 within 2 weeks. During each treatment fraction, patients received at least three 4D CBCT scans: setup verification, post-correction verification, and post-treatment verification.

### 4.2.2 Image pre-processing

The MRI and CT datasets were assessed using a research version of RayStation11A (RaySearch Laboratories, Stockholm, Sweden). The available data were divided into approximately 80% training and 20% testing cohorts. A total of 36 patients were included in the training cohort, 15 with paired data and 21 patients with unpaired data. Based on recommended industry standard settings, the minimum number of paired data can be used for training is 15.

However, the number of unpaired data is unlimited, depending on data availability.

Before training, the training datasets were pre-processed to select the paired data by registering the delayed 3DT1w MRI to the 3DCT using hybrid intensity and structure based deformable registration (DIR) with mutual information. This helped to mitigate inter-scan variation in patient positioning between the CT and MRI scans. The DIR of CT and MRI images was visually assessed and categorised as either well-matched or not well-matched. 15 paired datasets were selected from the well-matched DIR group to minimise the impact of imperfect registration in the training process. External contours were generated for delayed 3DT1w MRI and transferred to the 3DCT images using RayStation 11A DTK tool. A further pre-processing step for the paired dataset after DIR involved resampling the delayed 3DT1w MRI to the CT frame of reference. This ensure that the image intensities and internal anatomical positioning between the MRI and CT scans are correctly aligned.

The remaining 21 patients were selected for unpaired datasets, which included all 3DT1w MRI sequence (arterial, venous, late venous, and delayed images) with their corresponding 3DCT without pre-processing. It is hypothesised that this inclusion enhances the algorithm's generalisability and accuracy in generating sCT images by capturing a full range of tissue contrasts.

### 4.2.3 sCT model and testing data

The deep learning model used in this study is the same as previously described in Bird et al [28]. Briefly, it follows a structure similar to the CycleGAN architecture [30]. The model was designed to include paired and unpaired data for training to overcome voxel-to-voxel correspondence between patient CT and MRI datasets. A detailed description of the model is provided by Bird et al [28], as follows:

“A 3-slice 2D CNN architecture similar to CycleGAN [30] was trained in semi-supervised fashion, using both paired and unpaired data, to generate synthetic CTs. As in CycleGAN the model consists of two generators, one which converts the images from MRI to CT ($G_{CT}$) and one from CT to MRI ($G_{MR}$), and two discriminators which tried to discriminate between real and fake images, with $G_{CT}$ being the network that was used to generated the sCTs. The

generators consisted of four convolution layers with stride 2, followed by 9 residual blocks and then 4 deconvolution layers. The discriminator took a randomly cropped a 140 × 140 patch as input, followed by 5 convolutional layers with stride 2. ReLU was used as activation function in all layers except in the last layer in both the generator and discriminator. The main difference to the original CycleGAN implementation is the inclusion of an extra paired term in the generator cost function, to make use of the existence of paired data in this context. The discriminator weight (w1) was 1, the cycle weight (w2) was 7 and the paired weight (w3) was 3. Each model was trained using only paired CT-MRI data."

The training was conducted over 200 epochs, with a learning rate of 0.0001 and took approximately 200 hours to complete. Training was performed using a high-performance GPU.

sCT model analysis was conducted using an independent cohort of 11 patients. The same pre-processing of paired data described in section 2.2 was applied to the delayed 3DT1w MRI and CT. The sCT image was generated in less than 30 seconds. New external contours were created for all sCT images, and the PTV and OAR transferred from the source CT to the sCT images using RayStation 11A DTK tool.

### 4.2.4 sCT image evaluation

#### 4.2.4.1 Hounsfield unit (HU) analysis

HU analysis included calculating the mean absolute error (MAE), which quantifies the mean absolute differences in HU values on a voxel-by-voxel basis, within the areas of the external contour. MAE was used to assess HU accuracy between each sCT and CT, which indicates how accurately the HU values in sCT images match those in standard CT images.

#### 4.2.4.2 Plan generation & dosimetric analysis

A VMAT plan was created and optimised on a CT scan following our local clinical protocol for liver treatment. The plans were developed in RayStation 11A, using a beam energy of 6 MV flattening filter-free (FFF) on a dose grid of 2 × 2 × 2 $mm^3$, and 2 to 4 beams with different angles, depending

on the tumour size and location. Figure 4.1 illustrates the beam arrangement of the CT, and sCT plans. The liver plan was prescribed a dose of 40-50 Gy in 5 fractions to the PTV, while two patients received prescribed doses of 25 Gy and 35 Gy in 5 fractions due to their PTVs being close to the heart. The relevant OARs, along with their prescription dose constraints from our standard clinical protocol, are detailed in Table 4.1. Each CT plan was then recalculated on the sCT without re-optimisation.

Dosimetric comparison between doses calculated on CT and sCT was performed using the dose volume histogram (DVH) for the PTV, specifically evaluating D95%. For OAR analysis, the clinically used treatment plans were assessed based on DVH parameters, as shown in Table 4.1. The dose differences were normalised to the prescription dose. The dosimetric differences between sCT and CT were computed using the following formula:

$$\frac{\mathrm{DsCT} - \mathrm{DCT}}{\mathrm{Dpres}} \times 100\%$$

Where ΔD is the dose difference on the DVH statistics, DsCT and DCT are the doses on sCT and CT, respectively, and Dpres is the prescribed dose.

**Table 4.1: LCC liver SABR protocol for OARs prescription dose and constrains.**

| Liver OARs | *Dose constraint* | *Optimal for 5 fractions* |
|---|---|---|
| Duodenum | Dmax (0.5cc) | <30Gy |
| Stomach | Dmax (0.5cc) | <30Gy |
| Small Bowel | Dmax (0.5cc) | <30Gy |
| Oesophagus | Dmax (0.5cc) | <32Gy |
| Colon | Dmax (0.5cc) | <32Gy |
| CBD | Dmax (0.5cc) | <50Gy |
| Liver | MeanD | <13Gy |
| Kidney R | MeanD | <10Gy |
| Kidney L | MeanD | <10Gy |
| Spinal cord | Dmax (0.1cc) | <23Gy |

*Abbreviation: the mean dose (MeanD), the maximum dose to 0.5cc (Dmax), organ at risk (OAR), Leeds Cancer Centre (LCC), and stereotactic ablative radiotherapy (SABR).*

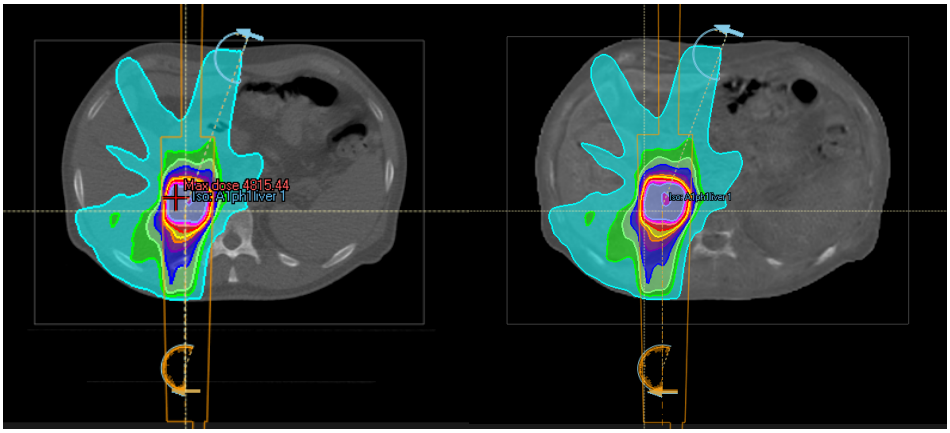

**Figure 4.1: Beam arrangement of the VMAT treatment plans, CT (Left) sCT (Right), illustrating arc rotation from 180° to 20° in both clockwise and counterclockwise directions. The color-coded isocentre represents the dose distribution, with a 40 Gy dose covering 95% of the volume.**

### 4.2.4.3 Patient positioning

#### 4.2.4.3.1 Reference data preparation

A total of 10 liver patients were included to evaluate the patient positioning accuracy of sCT as an alternative to CT. One patient was excluded due to the poor quality of the 4D CBCT. A new reference image was created using the sCT which was in the frame of reference of the CT. A new treatment

plan was created on the sCT with the same isocentre co-ordinates as the CT plan, ensuring that the reference position for translations and rotations in XVI are the same when using the CT or sCT as the reference image. Then, the sCT and CT data were imported into the clinical XVI software (Elekta, Stockholm, Sweden) for position verification, with the correction reference point selected at the plan isocentre.

#### 4.2.4.3.2 4D CBCT matching process

A total of 172 4D CBCT scans (mean 17 scans per patient) were used for image registration with both reference scans (CT and sCT) following the local matching protocol. A clip box, used for the registration process, was set up using each reference image and included liver anatomy, vertebrae, and ribs, excluding gases from the duodenum or stomach, as well as the small bowel where feasible. Figure 4.2 shows an example of a liver clip-box used for a CT reference. An automatic grey value registration algorithm was applied for all patients in accordance with the local protocol. To avoid operator bias, registration was initially performed on all CT data and then repeated for the sCT data with a one-day gap. In the 4D CBCT matching process, frame number 0 was selected before applying the correction as it represents the maximum exhale position, aligning with the position acquired from CT scans. Position errors were calculated in three translational (in mm) and three rotational (in ◦) directions.

#### 4.2.4.3.3 Patient Position verification

The accuracy of position verification was assessed by comparing the differences in translation and rotation between the reference images (CT or sCT) and the 4D CBCT. The mean and standard deviation of these differences were calculated for translation along the x, y, and z axes (left-right, anterior-posterior, superior-inferior) and for rotation around the x, y, and z axes (left-right/roll, anterior-posterior/pitch, superior-inferior/yaw). Systematic errors were evaluated using 95% confidence intervals.

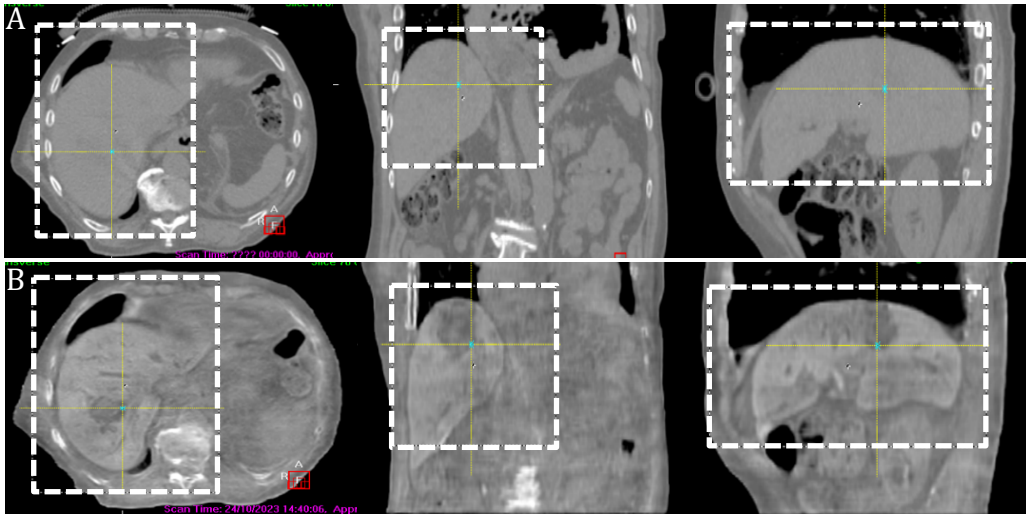


**Figure 4.2: Example of image registration clipbox positioned on a reference (A) CT and (B) sCT images for a liver patient in XVI (Elekta). The axial slice in (left), coronal (middle), and sagittal (right).**

### 4.2.5 Statistical analysis

Paired two-tailed t-tests were used to calculate 95% confidence intervals on the mean sCT-CT differences for dosimetric accuracy (defined as dosimetric uncertainty of sCT being within ±2% of CT) and for patient positioning to assess systematic error between the two reference images.

## 4.3 Results

### 4.3.1 HU analysis

The deep learning model successfully generated sCT images for all 11 patients. Figure 4.3 shows an example of axial slices in MRI, CT, and sCT for a single patient with liver cancer. The mean MAE for all patients was 109.5 ± 32.7 HU [range of 76.2-200.2 HU] in the body area.

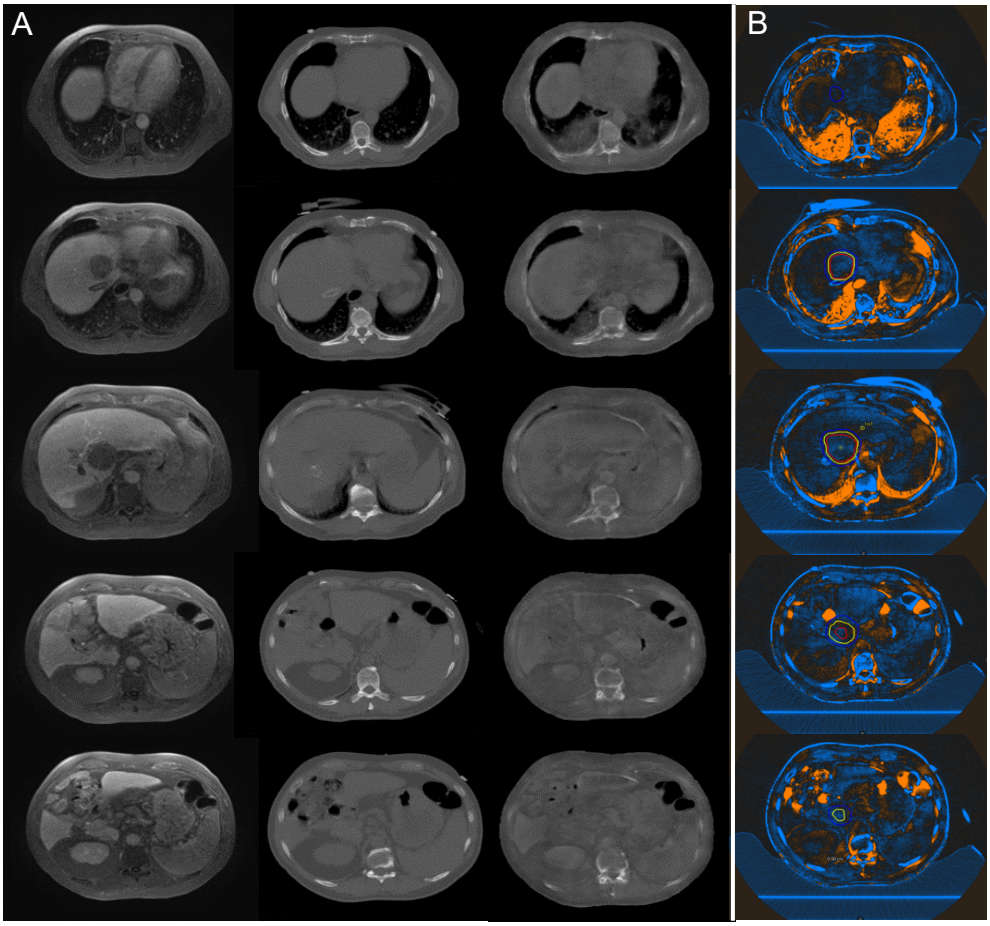


**Figure 4.3: (A) Axial slices of MRI (left), CT (middle) and sCT (right) for a liver cancer patient. Note that the bellows to assess the breathing trace is visible on CT. (B) Blue indicates areas where the CT HU values are higher than in the sCT, while orange indicates areas where the sCT HU values are higher than in the CT with a saturation threshold set at ±300 HU. The structure contours are shown as PTV (blue) ITV (yellow), and GTV (red).**

### 4.3.2 Dosimetric analysis

The mean differences between the clinically relevant DVH statistics are shown in Table 4.2. The relative mean dose difference for PTV between CT and sCT was 0.0 % (range: -1.4% to 1.3%, 95% confidence interval: -0.5 %to +0.5%). The mean OAR dose differences were <0.4 % (range: -1.6% to 1.6%,95% confidence intervals: -0.9% to +0.4%). The small bowel was an outlier and had a relative mean dose difference of -0.5%.

**Table 4.2: PTV and relative OAR dose differences between sCT and CT plans were analysed for the testing cohort. The mean difference and the 95% confidence interval range in dose difference between CT and sCT was calculated, where dose differences between sCT and CT were normalised to the prescribed dose.**

| Structures | Dose constraints | Dose difference (%) mean [range] | 95% confidence interval (%) | |
|---|---|---|---|---|
| | | | Lower | Upper |
| PTV | D95% | 0.0 [-1.4 to 1.3] | -0.5 | 0.5 |
| CBD | Dmax (0.5cc) | -0.4 [-1.5 to 0.7] | -0.9 | 0.2 |
| Colon | Dmax (0.5cc) | -0.1 [-0.7 to 0.5] | -0.3 | 0.2 |
| Duodenum | Dmax (0.5cc) | -0.0 [-0.8 to 0.6] | -0.4 | 0.3 |
| Kidney right | MeanD | -0.1 [-0.1 to 0.1] | -0.1 | 0.0 |
| Kidney left | MeanD | -0.0 [-0.1 to 0.0] | -0.1 | 0.0 |
| Liver | MeanD | 0.0 [-0.7 to 1.6] | -0.4 | 0.4 |
| Oesophagus | Dmax (0.5cc) | -0.4 [-1.1 to 0.0] | -0.8 | 0.0 |
| Small bowel | Dmax (0.5cc) | -0.5 [-2.4 to 0.0] | -1.5 | 0.5 |
| Spinal cord | Dmax (0.1cc) | -0.3 [-1.1 to 0.1] | -0.6 | 0.0 |
| Stomach | Dmax (0.5cc) | -0.4 [-1.6 to 0.7] | -0.8 | 0.0 |

*Abbreviation: planning target volume (PTV); common bill ducts (CBD); organ at risk (OAR); maximum dose (Dmax); and mean dose (meanD).*

### 4.3.3 Patient Position verification

Table 4.3 shows the registration differences between CT and 4D CBCT, and sCT and 4D CBCT for translations and rotations, including their associated 95% confidence intervals. For translations, the mean differences in all directions were less than 0.5 mm, with the 95% confidence intervals ranging from 0.0 mm to 0.1 mm. For rotations, the mean differences were less than 0.5° in all directions, with a 95% confidence interval of -0.2° to 0.6°. Figure 4.4 shows the

distribution of the positioning errors between CT and 4D CBCT and sCT and 4D CBCT for translations and rotations.

**Table 4.3: Shows the registration differences between CT and 4D CBCT minus sCT and 4D CBCT for translations and rotations in different directions, along with 95% confidence intervals.**

| reference image (sCT vs CT) | **Direction** | **Mean (SD)** | **95% confidence intervals (Upper; Lower)** |
|---|---|---|---|
| Translations (mm) | X (LR) | -0.3 (0.7) | (0.0; 0.0) |
| | Y (AP) | -0.1 (1.0) | (0.0; 0.0) |
| | Z (SI) | 0.5 (0.9) | (0.1; 0.0) |
| Rotations (°) | X (LR) | 0.5 (0.7) | (0.6; 0.4) |
| | Y (AP) | -0.3 (0.7) | (-0.2; -0.4) |
| | Z (SI) | 0.4 (0.5) | (0.5; 0.3) |

*Abbreviations: left-right (LR); superior-inferior (SI); posterior-anterior (PA); synthetic CT (sCT); computed tomography (CT); and standard deviation (SD).*

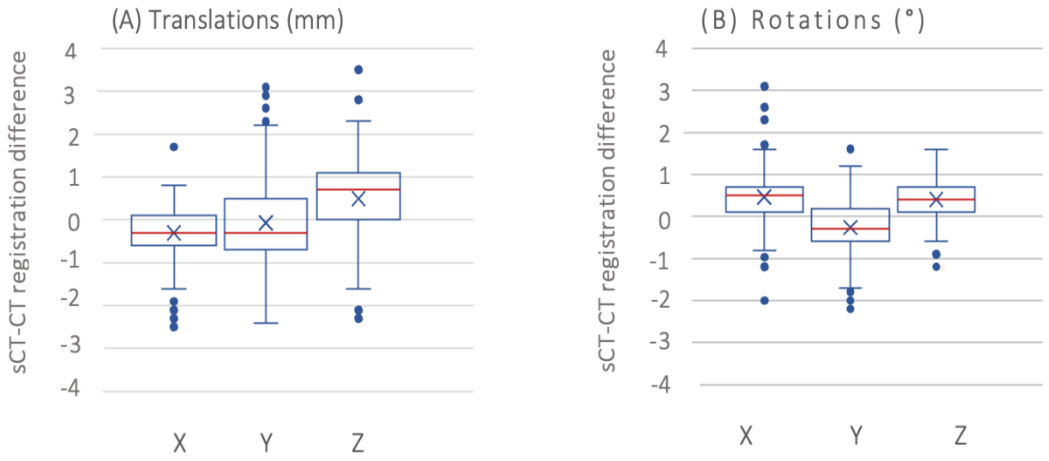


**Figure 4.4: Box plots of patient positioning verification results for 10 liver cancer patients. Each data point represents the difference between sCT to 4D CBCT minus CT to 4D CBCT registrations. The lower and upper fences correspond to the 25th and 75th percentiles, with the median (red line) in between and the mean represented by a cross (x). (A) Translation. The y-axis represents the distance in millimetres (mm), while the x-axis represents the three directions: X (left-right, LR), Y (anterior-posterior, AP), and Z (superior-inferior, SI). (B). Rotation. The y-axis represents the angle in degrees (°), while the x-axis represents the three directions: X (roll), Y (pitch), and Z (yaw).**

## 4.4 Discussion

This study evaluated the clinical feasibility of an MRI-only workflow for liver SABR. This is the first study to investigate sCT generation based on a deep learning model in terms of both dosimetric accuracy and positioning verification. The model demonstrated an sCT generation model that produces dosimetrically and anatomically accurate sCT, suitable for precise treatment planning and 4D CBCT-based patient positioning.

In this study, the sCT model is based on a CycleGAN architecture and combines paired and unpaired training data. This approach initially proposed by Jin et al [9] for the brain, demonstrated that a mix of paired and unpaired data outperformed models trained only with either paired or unpaired data. A key difference of this model is that it has been developed by a commercial (TPS) company (RaySearch Laboratories), which enhances its availability for use with more MRI sequences, independent of MRI vendors, in number of organ sites [29].

This study demonstrated a high level of dosimetric agreement between plans from CT recalculated on sCT, with a mean dosimetric accuracy of 0.0% for the D95% PTV and less than 0.5% for all OARs. Additionally, the systematic errors in image registration between sCT to 4D CBCT and CT to 4D CBCT, with mean differences of 0.5 mm in translation and less than 0.5° in rotation, demonstrated that sCT can be used as an alternative reference to CT. Overall, the sCT model met all evaluation criteria, with clinically acceptable results indicated by 95% confidence intervals within ±2 between the generated sCT and CT for liver patients.

HU analysis demonstrated a mean $MAE_{body}$ of 109.5 HU, which was comparable to the range reported in previous studies on sCT for the liver (mean $MAE_{body}$ ranging from 35.6 to 150 HU) [19-28, 31, 32]. It is important to note that this wide range of MAE may be influenced by the quality of the training data. Using the same model, smaller MAE was reported for the pelvis. This may be due to better MRI image quality in the pelvis, as it is not affected as much by motion and longer MRI acquisition times are possible [29]. Despite these factors, the impact of higher MAE on dosimetric accuracy remained minimal. This may be because HU discrepancies have less impact on VMAT planning, where multiple treatment angles help average out the differences in HU.

In terms of dosimetric accuracy, this study achieved improved mean differences in PTV D95% (0.0%) compared to previous studies of 0.9% [27], -0.5% [21]. The relative differences in all OARs were also comparable to those reported in previous studies [19-28]. A single patient showed dose differences in the small bowel, with a result of 2.4%. This is because differences in gas and bowel content cause a shift in their position between scans. Based on visual assessment, we hypothesized that this difference was large differences in HU values near the small bowel between the sCT and CT. This difference was caused by a significant amount of free fluid near the liver in the CT, which appeared as a dark signal in the T1w MRI. Consequently, when generating the sCT from the MRI, the model misinterpreted this as air. Additionally, although the difference in the PTV dose for this patient was small (-1.4%), it was the largest observed compared to other patients. This patient had the largest dosimetric differences for OARs as well such as CBD, liver, and stomach. However, these differences are still considered to be clinically acceptable as they do not exceed ±2% [33].

Overall, the 4D CBCT position verification analysis indicated that the systematic translational differences between sCT and CT were within acceptable limits, comparable to the clinical CT-based protocol for liver SABR at the LCC. This protocol indicates that an acceptable error is less than 2 mm for correction to proceed with treatment, while errors larger than 2 mm are considered for re-scanning. The majority of the image registrations fell within this range, with many scans showing differences of less than 2 mm, which is clinically acceptable for correction and treatment. Rotational differences are not typically considered in the liver SABR protocol unless they are excessively large. However, this study focused on the ability of the XVI system to accurately registered sCT as a reference compared to CT. Based on the results, there was a strong agreement between the two scans, despite the inherent uncertainties in the registration process, especially with 4D CBCT scans. Factors such as organ motion, sCT image quality, and inter-observer variation contribute to these uncertainties.

Notably, outliers were found in two patients (Figure 4.4). One of these patients was previously discussed, showing the largest differences in translation, with 3.5 mm, and rotation, with 3.1° in the right to left direction due

to internal positioning differences and variations in HU values. It is hypothesized that the second patient's differences were due to significant variations in gas between the sCT and CT scans in the small bowel. It is important to note that these two patients had 18 and 19 4D CBCT registrations, indicating that some errors occurred repeatedly. In addition, Figure 4.3 showed residual positional differences between the same axial slices on CT, MRI, and sCT. The overall errors observed are primarily due to patient positioning changes and breathing motion, which were not eliminated during the image preparation process.

Despite these variations, the overall differences reported in this study are considered to be clinically acceptable which confirms that sCT can reliably serve as an alternative reference to CT, supporting precise patient positioning in liver radiotherapy treatment planning. The results suggested that the observed variations were unlikely to be the result of systematic biases in the model, further highlighting the reliability of the sCT model for use in liver radiotherapy treatment planning.

No prior studies have evaluated positioning verification with 4D CBCT specifically for the liver, making this study a significant contribution to the field as it fills this gap by providing a comprehensive assessment of the sCT model within an MRI-only workflow for liver radiotherapy treatment planning. To compare our findings with prior research, we examined studies on pelvic MRI-only workflows due to their close anatomical similarity to other available sCT data. Although a direct comparison cannot be made because of different imaging modalities and registration techniques, a previous systematic review highlighted examples of clinical validation for patient treatment positioning using CBCT and digitally reconstructed radiograph (DDR), with results that were compatible with our findings [34].

It is important to note that all sCT models for the liver published in the literature were built in-house, highlighting the need for commercial solutions from vendors. Existing MRI-only workflows solutions for other anatomies are often limited to one vendor and specific sequences. Although this sCT model is not yet available as a commercial solution for the liver, its feasibility for adoption by various hospitals is high. This is due to its incorporation into a widely used treatment planning system (RayStation). The accuracy of this model was excellent and comparable to other sCT solutions available for pelvic or prostate

MRI-only workflows [6, 13, 35]. This represents a significant step towards the implementation of MRI-only radiotherapy for the liver, addressing current workflow challenges by minimising geometric errors associated with image registration, reducing patient appointments, and potentially lowering costs [36]. However, the adoption of MRI-only radiotherapy for liver treatments is currently limited by the requirement for 4D MRI to assess liver motion, as 4D CT remains the standard for motion management in liver SABR radiotherapy treatment planning. Further research is essential to integrate validated 4D MRI techniques for liver treatments, which would enable a comprehensive evaluation of MRI-only workflows for liver radiotherapy [18].

This study is not without limitations. One key issue was the sub-optimal MRI image quality. Although the results indicated that the generated sCT performed well, it is possible that the poor MRI quality may have influenced the training of the model rather than the final sCT output. Additionally, the image quality of the sCT could be improved by including more training data. Abdominal MRI quality is often compromised by motion artefacts due to patients' difficulty in maintaining breath-holds, especially considering that they undergo a CT simulation first, which can make the MRI simulation uncomfortable. While paired data with well-matched CT and MRI scans were used for training, training the model with higher quality images could enhance the sCT image quality and model accuracy, particularly for structures like ribs. This would further enhance the patient positioning. Another limitation is that the CycleGAN model is not yet clinically released as a commercial solution. Bird et al demonstrated its accuracy and capability in different anatomical sites [29] – here we investigated the liver, proving its feasibility for use in clinical settings. Additionally, the limited number of patients tested for model validation restricts the ability to generalise the findings. Testing the model on a larger patient population, including a variety of clinical scenarios, would better support the generalisation of the model and ensure its robustness across different clinical situations. However, this study provided strong evidence supporting the feasibility of using sCT model in clinical practice.

## 4.5 Conclusion

This study is the first to evaluate the dosimetric accuracy and position verification of a sCT model generated by a deep learning algorithm developed

by commercial company for liver SABR treatment, bringing it closer to clinical implementation. The model demonstrated high dosimetric accuracy and precise patient positioning. Despite the sub-optimal MRI quality, the model achieved clinically acceptable accuracy, with the largest variations due to individual patient differences. These findings represent a significant advancement in the implementation of MRI-only workflows for liver SABR treatments, addressing key challenges and assisting broader clinical adoption.

## 4.6 Reference


[1] SABR UK Consortium. Stereotactic Ablative Body Radiation Therapy (SABR) 2015 [Available from: https://www.sabr.org.uk/wp-content/uploads/2019/04/SABRconsortium-guidelines-2019-v6.1.0.pdf.

[2] Lewis S, Dawson L, Barry A, Stanescu T, Mohamad I, Hosni A. Stereotactic body radiation therapy for hepatocellular carcinoma: From infancy to ongoing maturity. JHEP Reports. 2022;4:100498

[3] Shanker MD, Moodaley P, Soon W, Liu HY, Lee YY, Pryor DI. Stereotactic ablative radiotherapy for hepatocellular carcinoma: A systematic review and meta-analysis of local control, survival and toxicity outcomes. J Med Imag Radiat Oncol. 2021;65:956-68. https://doi.org/10.1111/1754-9485.13309.

[4] Alrabiah K, Liao G, Shen Q, Chiang C-L, Dawson LA. The evolving role of radiation therapy as treatment for liver metastases. Journal of the National Cancer Center. 2022

[5] Høyer M, Swaminath A, Bydder S, Lock M, Romero AM, Kavanagh B, et al. Radiotherapy for liver metastases: a review of evidence. International Journal of Radiation Oncology* Biology* Physics. 2012;82:1047-57

[6] Lerner M, Medin J, Jamtheim Gustafsson C, Alkner S, Olsson LE. Prospective Clinical Feasibility Study for MRI-Only Brain Radiotherapy. Frontiers in oncology. 2022;11:812643-. 10.3389/fonc.2021.812643.

[7] Bird D, Henry AM, Sebag-Montefiore D, Buckley DL, Al-Qaisieh B, Speight R. A Systematic Review of the Clinical Implementation of Pelvic Magnetic Resonance Imaging (MR)-Only Planning for External Beam Radiation Therapy. 2019

[8] Tyagi N, Zelefsky MJ, Wibmer A, Zakian K, Burleson S, Happersett L, et al. Clinical experience and workflow challenges with magnetic resonance-only radiation therapy simulation and planning for prostate cancer. Physics and Imaging in Radiation Oncology. 2020;16:43-9. https://doi.org/10.1016/j.phro.2020.09.009.

[9] Jin CB, Kim H, Liu M, Jung W, Joo S, Park E, et al. Deep CT to MR Synthesis Using Paired and Unpaired Data. Sensors (Basel). 2019;19. 10.3390/s19102361.

[10] Johnstone E, Wyatt JJ, Henry AM, Short SC, Sebag-Montefiore D, Murray L, et al. Systematic Review of Synthetic Computed Tomography Generation Methodologies for Use in Magnetic Resonance Imaging-Only Radiation Therapy. Int J Radiat Oncol Biol Phys. 2018;100:199-217. 10.1016/j.ijrobp.2017.08.043.

[11] Boulanger M, Nunes J-C, Chourak H, Largent A, Tahri S, Acosta O, et al. Deep learning methods to generate synthetic CT from MRI in radiotherapy: A literature review. Physica medica. 2021;89:265-81. https://doi.org/10.1016/j.ejmp.2021.07.027.

[12] Spadea MF, Maspero M, Zaffino P, Seco J. Deep learning based synthetic-CT generation in radiotherapy and PET: A review. Med Phys. 2021;48:6537-66. 10.1002/mp.15150.

[13] Ranta I, Wright P, Suilamo S, Kemppainen R, Schubert G, Kapanen M, et al. Clinical feasibility of a commercially available MRI-only method for radiotherapy treatment planning of the brain. J Appl Clin Med Phys. 2023;24:e14044. https://doi.org/10.1002/acm2.14044.

[14] healthcare P. MRCAT Pelvis

MR-RT clinical application [Available from: https://www.philips.co.uk/healthcare/product/HCNMRF266/mrcat-pelvis-mr-rt-clinical-application.
[15] healthcare P. MRCAT Brain MR-RT clinical application [Available from: https://www.philips.co.uk/healthcare/product/HCNMRF320/mrcat-brain-mr-rt-clinical-application.
[16] Spectronic M. MRI only radiotherapy planning using MRI Planner [Available from: https://medical.spectronic.se/page-2/page6/index.html.
[17] Siemens-healthineers. MR-only Radiotherapy Planning [Available from: https://www.siemens-healthineers.com/en-uk/magnetic-resonance-imaging/clinical-specialities/synthetic-ct.
[18] Aljaafari L, Bird D, Buckley DL, Al-Qaisieh B, Speight R. A systematic review of 4D magnetic resonance imaging techniques for abdominal radiotherapy treatment planning. Physics and Imaging in Radiation Oncology. 2024;31:100604. https://doi.org/10.1016/j.phro.2024.100604.
[19] Cusumano D, Lenkowicz J, Votta C, Boldrini L, Placidi L, Catucci F, et al. A deep learning approach to generate synthetic CT in low field MR-guided adaptive radiotherapy for abdominal and pelvic cases. Radiother Oncol. 2020;153:205-12
[20] Florkow MC, Guerreiro F, Zijlstra F, Seravalli E, Janssens GO, Maduro JH, et al. Deep learning-enabled MRI-only photon and proton therapy treatment planning for paediatric abdominal tumours. Radiother Oncol. 2020;153:220-7
[21] Fu J, Singhrao K, Cao M, Yu V, Santhanam AP, Yang Y, et al. Generation of abdominal synthetic CTs from 0.35 T MR images using generative adversarial networks for MR-only liver radiotherapy. Biomed Phys Eng Express. 2020;6:015033
[22] Hernandez AG, Fau P, Wojak J, Mailleux H, Benkreira M, Rapacchi S, et al. Synthetic computed tomography generation for abdominal adaptive radiotherapy using low-field magnetic resonance imaging. Physics and Imaging in Radiation Oncology. 2023;25:100425
[23] Kang SK, An HJ, Jin H, Kim J-i, Chie EK, Park JM, et al. Synthetic CT generation from weakly paired MR images using cycle-consistent GAN for MR-guided radiotherapy. Biomedical engineering letters. 2021;11:263-71
[24] Lapaeva M, Saint-Esteven ALG, Wallimann P, Günther M, Konukoglu E, Andratschke N, et al. Synthetic computed tomography for low-field magnetic resonance-guided radiotherapy in the abdomen. Physics and imaging in radiation oncology. 2022;24:173-9
[25] Li X, Yadav P, McMillan AB. Synthetic computed tomography generation from 0.35 T magnetic resonance images for magnetic resonance–only radiation therapy planning using perceptual loss models. Practical Radiation Oncology. 2022;12:e40-e8
[26] Liu L, Johansson A, Cao Y, Dow J, Lawrence TS, Balter JM. Abdominal synthetic CT generation from MR Dixon images using a U-net trained with 'semi-synthetic'CT data. Physics in Medicine & Biology. 2020;65:125001
[27] Liu Y, Lei Y, Wang T, Kayode O, Tian S, Liu T, et al. MRI-based treatment planning for liver stereotactic body radiotherapy: validation of a deep learning-based synthetic CT generation method. The British Journal of Radiology. 2019;92:20190067

[28] Nousiainen K, Santurio GV, Lundahl N, Cronholm R, Siversson C, Edmund JM. Evaluation of MRI-only based online adaptive radiotherapy of abdominal region on MR-linac. J Appl Clin Med Phys. 2023;24:e13838

[29] Bird D, Speight R, Andersson S, Wingqvist J, Al-Qaisieh B. Deep learning MRI-only synthetic-CT generation for pelvis, brain and head and neck cancers. Radiother Oncol. 2024;191:110052. https://doi.org/10.1016/j.radonc.2023.110052.

[30] Zhu JY, Park T, Isola P, Efros AA, editors. Unpaired Image-to-Image Translation Using Cycle-Consistent Adversarial Networks. 2017 IEEE International Conference on Computer Vision (ICCV); 2017 22-29 Oct. 2017.

[31] Qian P, Xu K, Wang T, Zheng Q, Yang H, Baydoun A, et al. Estimating CT from MR abdominal images using novel generative adversarial networks. Journal of Grid Computing. 2020;18:211-26

[32] Xu K, Cao J, Xia K, Yang H, Zhu J, Wu C, et al. Multichannel residual conditional GAN-leveraged abdominal pseudo-CT generation via Dixon MR images. IEEE Access. 2019;7:163823-30

[33] Korsholm ME, Waring LW, Edmund JM. A criterion for the reliable use of MRI-only radiotherapy. Radiat Oncol. 2014;9:1-7. https://doi.org/10.1186/1748-717X-9-16.

[34] Bird D, Henry AM, Sebag-Montefiore D, Buckley DL, Al-Qaisieh B, Speight R. A Systematic Review of the Clinical Implementation of Pelvic Magnetic Resonance Imaging–Only Planning for External Beam Radiation Therapy. International Journal of Radiation Oncology*Biology*Physics. 2019;105:479-92. https://doi.org/10.1016/j.ijrobp.2019.06.2530.

[35] Persson E, Jamtheim Gustafsson C, Ambolt P, Engelholm S, Ceberg S, Bäck S, et al. MR-PROTECT: Clinical feasibility of a prostate MRI-only radiotherapy treatment workflow and investigation of acceptance criteria. Radiat Oncol. 2020;15:1-13

[36] Persson E, Svanberg N, Scherman J, Jamtheim Gustafsson C, Fridhammar A, Hjalte F, et al. MRI-only radiotherapy from an economic perspective: Can new techniques in prostate cancer treatment be cost saving? Clin Transl Radiat Oncol. 2023;38:183-7. 10.1016/j.ctro.2022.11.012.

# Chapter 5 Clinical validation of using a commercial synthetic-computed tomography solution for brain MRI-only radiotherapy treatment planning.

**Chapter note:** This work was presented as a Proffered Paper at ESTRO 2025 (see Appendix C). This chapter has been published in *Technical Innovations & Patient Support in Radiation Oncology 2025;35:100589. https://doi.org/10.1016/j.tipsro.2025.100328.*

## Abstract

**Background and purpose:** MRI-only radiotherapy treatment planning (RTP) relies on synthetic-CT (sCT) images for dose calculation. This study evaluates the clinical feasibility of using a commercial sCT solution in brain RTP, MRCAT Brain, focusing on dosimetric accuracy and patient setup verification.

**Method and materials:** For dosimetric evaluation, 93 patients with brain cancer who were treated with volumetric modulated arc therapy (VMAT) using a CT/MRI fusion workflow were included. sCT images were generated using MRCAT Brain. The sCT images were rigidly co-registered to the CT images. The clinical plan produced on the CT was recalculated on the sCT. Dosimetric accuracy was assessed by comparing dose differences in dose volume histogram (DVH) statistics for the planning target volume (PTV) and organs at risk (OARs).

For patient setup verification, 70 patients were included, and a total of 572 cone beam CT (CBCT) registrations were performed with sCT and CT as reference images. The sCT matching accuracy was validated by comparing the translational and rotational differences between sCT-CBCT and CT-CBCT registrations.

**Results:** The PTV relative mean dose difference between CT and sCT were 0.3%, 0.4%, and 0.2% for D50%, D2%, and D98%, respectively. The OAR relative mean dose differences were less than 0.3% for all OARs. 4 of 93 patients (4.3%) showed gross dosimetric errors of greater than ±2%. 3/4 were caused by sCT error. For positioning verification, all results were between ±1 mm and ±1°.

**Conclusion:** This study demonstrates the clinical feasibility of the MRCAT solution for brain MRI-only RTP, with dosimetric differences being clinically acceptable, along with submillimetre and sub-degree accuracy in patient setup verification.

**Keywords**: MRI-only planning; synthetic-CT model; Brain cancer; Artificial intelligence.

## 5.1 Introduction

Brain radiotherapy treatment planning (RTP) relies on magnetic resonance imaging (MRI) for target delineation owing to its superior soft tissue contrast compared to computed tomography (CT) [1-3]. However, CT simulation remains essential for dose calculation and patient positioning during treatment delivery. The use of both imaging modalities requires co-registration of MRI and CT images, which can result in registration errors [4]. There is growing interest in implementing MRI-only RTP to eliminate uncertainties arising from co-registration and to simplify the workflow. An important benefit of MRI-only RTP is to eliminate the need for a CT scan. The patient only needs a single MRI scan for both delineation and treatment planning reducing time spent in the hospital.

MRI-only RTP requires an accurate synthetic-CT (sCT) image to provide electron density for dose calculation and patient positioning verification by registering to CBCT during treatment. With improvements in artificial intelligence (AI), researchers have increasingly focused on deep learning-based sCT models due to their enhanced performance [5-7]. Four commercial solutions using AI models are available as CE-marked and FDA-cleared software to directly produce brain sCT image from MRI data: MRCAT (Philips, Amsterdam, Netherlands), syngovia RT (Siemens Healthineers, Erlangen, Germany), MRI Planner (Spectronic Medical, Helsingborg, Sweden), and MR-Box (Therapanacea, Paris, France).

Clinical validation of these brain sCT products has been reported, and some have already been implemented clinically in specialist centres [8-14]. Three studies evaluated the MRCAT solution, Emin et al. [8] clinically implemented MRI-only in two cohorts, 30 patients for commissioning and 30 for validation, reporting relative differences within ±0.7 % for the planning target

volume (PTV) and ±1.3 % organs at risk (OAR). However, this study did not include a quantitative assessment of patient positioning. Ranta et al. [10] reported a mean PTV difference of ≤0.6% and normal brain tissue differences of ≤1.7%, of 50 patients with positioning accuracy ranging from -2 to 2.5 mm (translation) and -1° to 0.5° (rotation) evaluated in only 20 patients using Varian Eclipse. Similarly, another study reported a mean PTV difference of -0.5% and an OAR difference of ≤0.7% in a cohort of 18 patients; however, positioning accuracy was not evaluated [11]. In addition, Lerner et al. [15] clinically implemented the MRI Planner solution in a cohort of 21 patients, demonstrating dose differences range within ±1% for the PTV and OAR, along with excellent CBCT positioning accuracy with within ± 1 mm in translation using the Varian Eclipse image registration tool. However, previous evaluation relied on the treatment planning system (TPS) rather than dedicated positioning software used on a linac during treatment.

Other studies using Syngovia reported mean differences of 0.2% [13, 14] for the PTV and ≤1.6% [14] for the OAR. However, patient positioning was evaluated using 2D/2D kV images with the Brainlab Exactrac system, showing translational shifts of up to 5 mm and rotational errors of up to 4°. To the best of our knowledge, none of the previous studies have compared sCT and CT for CBCT-based patient positioning using a commercially available positioning software system. Therefore, this study aims for the first time in the literature to evaluate the MRCAT solution in brain radiotherapy across a large cohort of 94 patients to assess its dosimetric accuracy, and to verify patient positioning using the Elekta XVI system, following the exact clinical workflow including its registration features, similarity measures, and tolerances.

## 5.2 Methods and materials

### 5.2.1 Patient cohort and image acquisition

Ethical approval was granted under the Leeds East Research Ethics Committee (REC) (reference: 19/YH/0300; IRAS project ID: 342888) to include data from 93 retrospective patients who received brain radiotherapy for palliative or radical treatment. The inclusion criteria required that patients had been treated with volumetric modulated arc therapy (VMAT) and underwent both CT and MRI simulations as part of their clinical pathway, with synthetic CT

images generated during their MRI simulation following the acquisition of a source MRI scan. The exclusion criteria for MRCAT sCT generation, include bone disease and large tattoos in the head area. A thermoplastic head mask with three reference points, laser positioning markers and neck and knee support were used to immobilise patients during MRI and CT simulations, as well as throughout the radiotherapy treatment sessions. CT and MRI scans were conducted within a few hours to minimise positioning errors. The image acquisition detailed are in Table 5.1.

**Table 5.1: shows the image acquisition details for CT, MRI, and CBCT.**

| Image acquisition | Parameters | | Make & Model |
|---|---|---|---|
| **CT** | Resolution ($mm^3$) | 1.2 x 1.2 x 2 | Philips Brilliance Big Bore (Koninklijke Philips N.V., the Netherlands) |
| | Tube voltage kVp | 120 | |
| | Tube current (mAs) | 295 | |
| | FOV | 600 x600 x236 | |
| | Scan time (s) | 15.2 | |
| **MRI** | Sequence | T1w 3D mDIXON FFE | 1.5T MR-RT scanner Philips Ingenia (Koninklijke Philips N.V., Amsterdam, the Netherlands) |
| | Acq. voxel size ($mm^3$) | 1.1x1.1x1.4 | |
| | Recon. voxel size ($mm^3$) | 0.6x0.6x1 | |
| | TE1/TE2 (ms) | 2/4.4 | |
| | TR (ms) | 6.8 | |
| | Flip angle (◦) | 12 | |
| | BW [Hz/px] | 481 | |
| | FOV ($mm^3$) | 232 ×270 ×260 | |
| | Scan time (min: s) | 2:56 | |
| **CBCT** | Resolution ($mm^2$) | 1 x 1 mm | XVI software (Elekta, Stockholm, Sweden) |
| | Slice thickness | 2 mm | |
| | kVp (kV) | 120 | |
| | Tube Current (mA) | 0.4 | |
| | Scan time (min) | 1 | |

*Abbreviation: computed tomography (CT); magnetic resonance imaging (MRI); acquisition (Acq); reconstruction (Recon); bandwidth (BW); pixel (px); echo time (TE); repetition time (TR); minutes: seconds (min:s); field of view (FOV) and cone beam CT (CBCT).*

### 5.2.2 sCT generation

The sCT images were generated using MRCAT brain, a commercially available product based on a deep learning algorithm (magnetic resonance for calculating attenuation, MRCAT Brain, version 4.0; Philips Oy, Vantaa, Finland). The algorithm uses a dedicated MRI acquisition, the 3D T1-weighted mDIXON XD FFE MRCAT source scan, which provides in-phase, fat-only, and water-only images to generate MRCAT image. The MRCAT Brain algorithm employs a supervised, fully convolutional encoder–decoder convolutional neural network (CNN) trained on matched pairs of MR and CT data to perform voxel-wise regression for synthetic CT generation [16]. The sCT images are automatically reconstructed from the MRCAT source MRI and provide relevant density information for dose calculation as part of the post-processing, with no user input.

### 5.2.3 Plan generation

The CT, sCT, clinical treatment structures and plan were imported for each patient into RayStation Research version 12A-SP1 ML (RaySearch Laboratories, Stockholm, Sweden). The target was delineated on MRI, and the organs at risk (OAR) on CT. All patients were treated with VMAT plans with 4–5 mm PTV margin. The standard prescribed dose for radical treatment of brain tumours (e.g., glioma or meningioma) ranges from 50.4 Gy to 60 Gy delivered over 28–30 fractions; for palliative treatment, it ranges from 30 Gy to 40 Gy over 6–15 fractions. A beam energy of 6 MV flattening filter-free (FFF) and a dose grid of 3 × 3 × 3 $mm^3$ were used according to our clinical protocol for external beam treatment. The sCT images were rigidly co-registered with 6 degrees of freedom to the CT and resampled into the CT frame of reference to ensure accurate alignment of image intensities and internal anatomical positioning between the sCT and CT scans. The planning target volume (PTV) and OAR contouring were then transferred from the CT onto the sCT, except for the external contour, it can be automatically generated in RayStation. The clinical

plan calculated on the CT without optimisation was then recalculated on the sCT for evaluation.

### 5.2.4 Dosimetric evaluation

A dosimetric comparison between CT and sCT was performed using dose-volume histogram (DVH) statistics for the PTV and OARs. DVH statistics were selected according to our local clinical protocol and in line with ICRU Report 83 guidelines [17]. For the PTV, the analysis included D50, D2, and D98. For the OARs, the evaluated DVH statistics included: Dmean and D0.1cc for the following OARs: brainstem, optic chiasm, optic nerves (left and right), orbits (left and right, and Dmean only for: cochlea (left and right), lacrimal glands (left and right), and lenses (left and right). The dosimetric differences between sCT and CT were computed using the following formula:

$$\Delta D = \frac{DsCT - DCT}{Dpres} \times 100\%$$

Where ΔD is the dose difference on the DVH statistics, $D_{sCT}$ and $D_{CT}$ are the doses on sCT and CT, respectively, and $D_{pres}$ is the prescribed dose.

### 5.2.5 Patient set-up verification

#### 5.2.5.1 Reference data preparation

70 patients who received brain radiotherapy were included to assess the accuracy of patient positioning verification, using sCT in comparison to CT as the reference image on treatment delivery. 286 CBCTs were registered to the CT and sCT, respectively. For 47 patients, 5 CBCTs were evaluated; however, due to missing data, 5 patients had 4 CBCTs, 3 patients had 3 CBCTs, and 15 patients had only 1 or 2 CBCTs. A new treatment plan was generated on the sCT, using the same isocentre coordinates as the CT plan to ensure consistent reference positions for the matching. sCT, CT, and CBCT datasets were imported into the clinical XVI software. Image registration was performed using the clinical XVI software version 5.0 (Elekta, Stockholm, Sweden), replicating the clinical treatment process.

#### 5.2.5.2 CBCT matching process

572 image registrations were re-performed offline on CBCT and CT, and CBCT and sCT, following the local matching protocol. A clip box was used to

include the skull and skull base while excluding the C-spine. Figure 5.1 shows an example of a brain clip-box used for a CT and sCT reference. An auto-matching grey value algorithm was applied for all patients using rigid registration. All registrations were performed by a single operator to ensure consistency across cases and eliminate inter-operator variability from the clinical workflow. The operator first registered all CT data, then repeated the registration on the sCT data with two days interval.

Positional errors were corrected in six degrees of freedom: three translations (measured in mm) and three rotations (measured in degrees). Translations were evaluated along the x, y, and z axes (left-right, anterior-posterior, superior-inferior), while rotations were assessed along the x (pitch), y (yaw), and z axes (roll). The mean difference was calculated for each axis. The systematic error in image registration between the two references, sCT and CT, were computed using the following formula:

$$\Delta T = T_{sCT/CBCT} - T_{CT/CBCT}$$

$$\Delta R = R_{sCT/CBCT} - R_{CT/CBCT}$$

where ΔT represents the translational difference in all directions (X, Y, Z), and ΔR represents the rotational difference in all directions (pitch, roll, yaw).

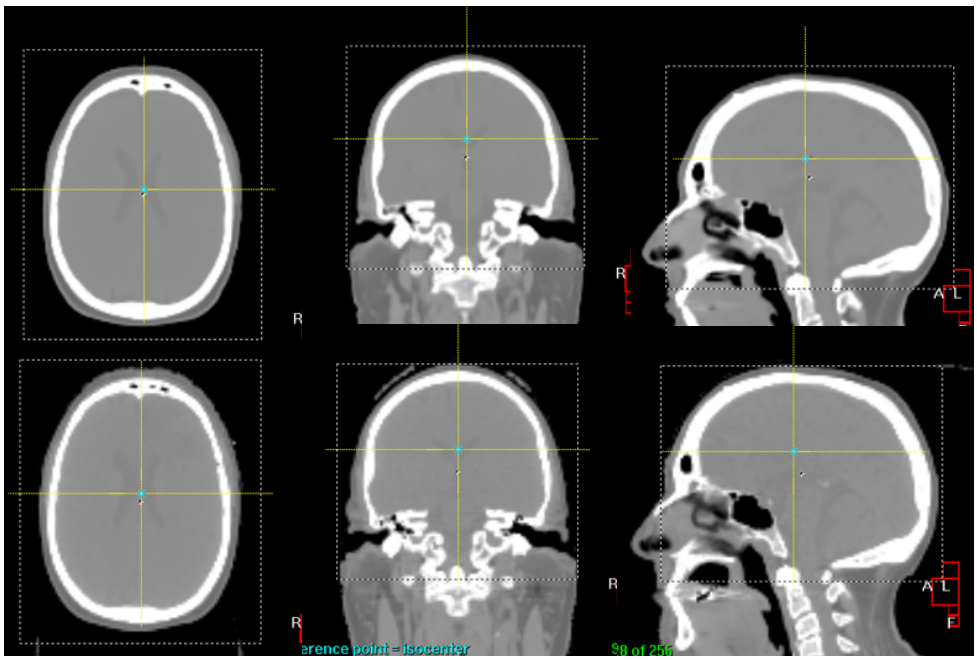


**Figure 5.1: Example of image registration clipbox positioned on a reference, sCT (top row) and CT (bottom row) images for a brain patient in XVI (Elekta). The axial slice in (left), coronal (middle), and sagittal (right).**

### 5.2.6 Statistical analysis

Paired two-tailed t-tests were used to calculate 95% confidence intervals on the mean sCT-CT differences for dosimetric accuracy (defined as dosimetric uncertainty of sCT being within ±2% of CT) and for patient positioning to assess systematic error between the two reference images.

## 5.3 Results

### 5.3.1 Dosimetric evaluation

Figure 5.2 shows example axial slices in CT and sCT for brain patients. Four patients showed significant dosimetric errors of ±2.0% or larger. When visually assessed 3 out of 4 were associated with sCT anatomical errors. The relative mean dose differences of the DVH statistics and the 95% confidence interval range are shown in Table 5.2. The PTV relative mean dose difference were 0.3%, 0.4%, and 0.2% for D50%, D2%, and D98%, respectively. Two patients demonstrating a PTV relative dose difference of $\geq$ ±2.0%, due to missing bone in the skull base or nasal bone, are shown in Figure 5.2. The 95% CI falls within a lower bound of 0.1% and an upper bound of 0.5%.

The OAR relative dose differences were less than 0.3% for all OARs. Notably, large outliers were observed in two patients who had dose differences greater than ±2.0%. One patient showed dose differences of -3.6% and -7.6% in the right orbit and lens, respectively due to signal void in MRI caused a sCT error. However, the second patient showed a dose difference of -2.6% in the left lacrimal gland, which is considered less significant due to its small volume being located on a dose gradient and was not caused by sCT anatomical errors. The 95% CI falls within a lower bound of -0.3% and an upper bound of 0.4%. Figure 5.3 shows the distribution of dose differences (%) between sCT minus CT in DVH statistics for PTV and OAR.

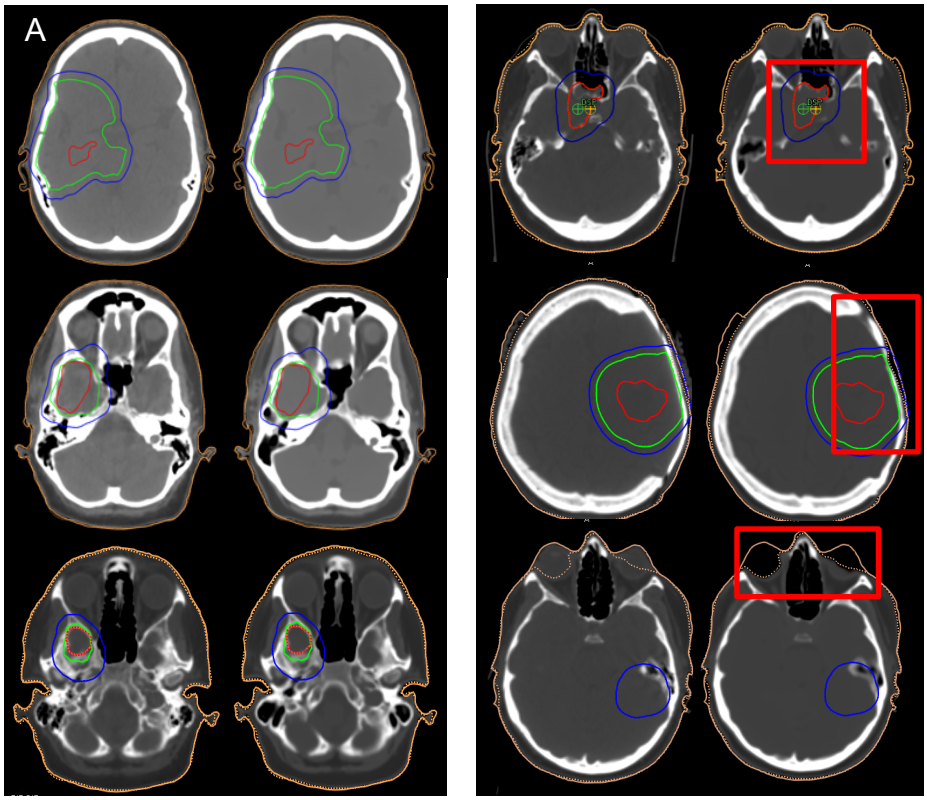


**Figure 5.2: (A) Axial slices of CT (left) and sCT (right). Based on expert visual assessment, sCT images demonstrate reliable anatomical detail comparable to conventional CT scans. (B) Axial slices from three patients demonstrating dosimetric errors due to gross sCT anatomical failures, resulting in MRCAT images that are unacceptable for clinical use, CT (left) and sCT (right). The top and middle images show sCT errors in the PTV (bone), while the bottom image shows an sCT error in the OAR (orbits and lens). The structure contours are shown as PTV (blue) CTV (green), and GTV (red).**

**Table 5.2: PTV and OAR relative mean dose difference and the 95% confidence interval range between sCT and CT.**

| Structure (number of patients) | DVH statistics (Gy) | Mean dose difference (95% CI lower, upper bound) (%) |
|---|---|---|
| **PTV (n=93)** | D50% | 0.3 (0.2, 0.3) |
| | D2% | 0.4 (0.3, 0.5) |
| | D98% | 0.2 (0.1, 0.2) |
| **Brainstem (n=93)** | Dmean | 0.2 (0.2, 0.2) |
| | D0.1cc | 0.3 (0.3, 0.4) |
| **Optic Chiasm (n=90)** | Dmean | 0.2 (0.2, 0.3) |
| | D0.1cc | 0.3 (0.2, 0.3) |
| **Pituitary (n=79)** | Dmean | 0.2 (0.2, 0.3) |
| **Optic Nerve L (n=93)** | Dmean | 0.2 (0.1, 0.2) |
| | D0.1cc | 0.2 (0.2, 0.3) |
| **Optic Nerve R (n=92)** | Dmean | 0.2 (0.1, 0.2) |
| | D0.1cc | 0.3 (0.2, 0.3) |
| **Orbit L (n=92)** | Dmean | 0.0 (0.0, 0.0) |
| | D0.1cc | 0.1 (0.1, 0.1) |
| **Orbit R (n=92)** | Dmean | -0.1 (-0.1, 0.0) |
| | D0.1cc | 0.1 (0.0, 0.1) |
| **Cochlea L (n=93)** | Dmean | 0.2 (0.1, 0.3) |
| **Cochlea R (n=93)** | Dmean | 0.2 (0.1, 0.3) |
| **Lacrimal Gland L (n=93)** | Dmean | -0.2 (-0.2, -0.1) |
| **Lacrimal Gland R (n=93)** | Dmean | -0.1(-0.2, 0.0) |
| **Lens L (n=91)** | Dmean | 0.0 (-0.1, 0.0) |
| **Lens R (n=91)** | Dmean | -0.1(-0.3, 0.1) |

*Abbreviation: planning target volume (PTV); mean dose (Dmean); Left (L); Right (R); and confidence interval (CI).*

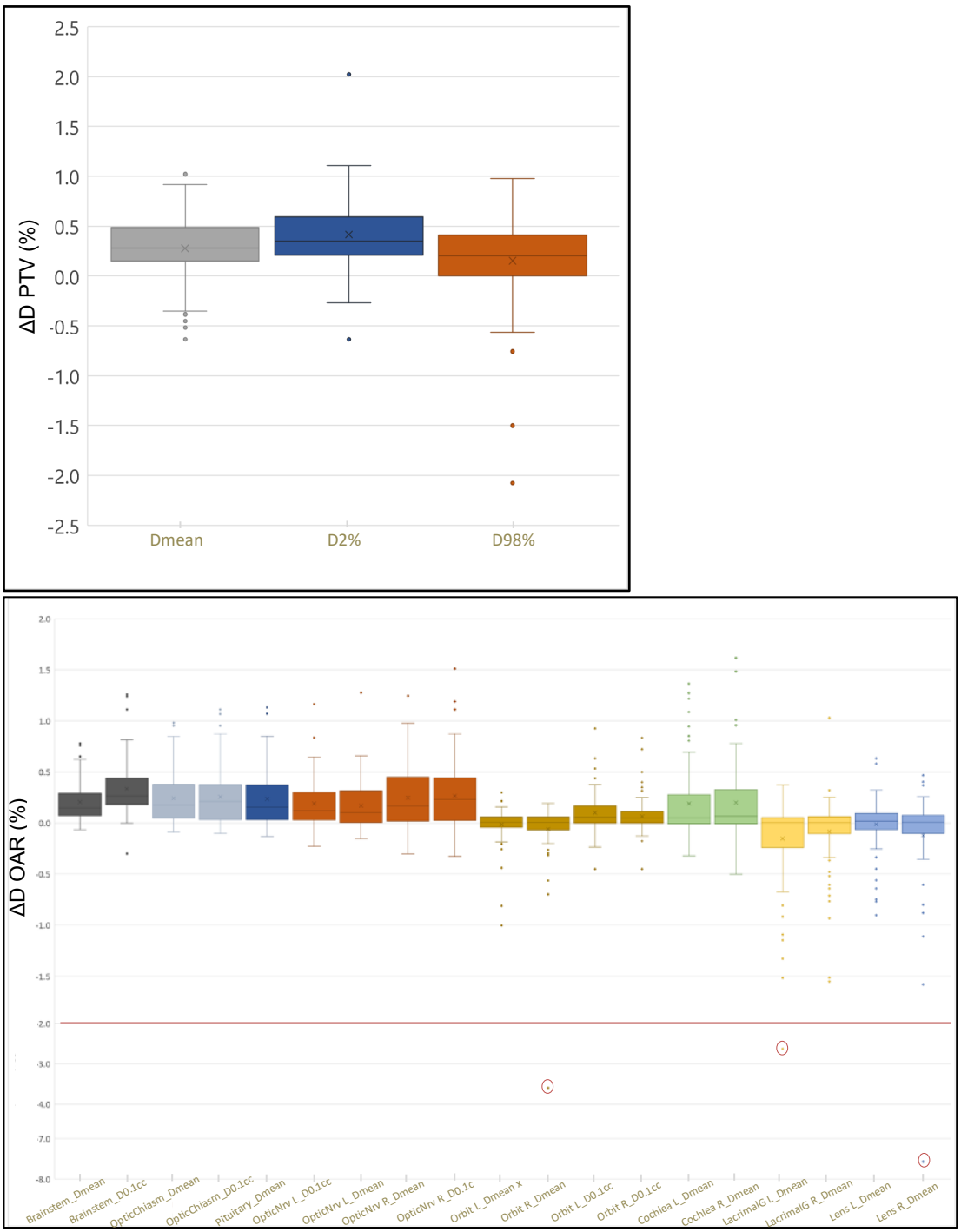


**Figure 5.3: Boxplots for (A) PTV and (B) OARs show dose differences (%) between CT plans and sCT recalculations on the Y-axis. The X-axis represents the contour and specific DVH. The box represents the interquartile range (IQR), the horizontal line indicates the median, whiskers show values within 1.5 times the IQR, and points are outliers. The red circles show the larger outliers.** *Abbreviation: planning target volume (PTV); organ at risk (OAR); mean dose (Dmean); Left (L); Right (R); optic nerve (OpticNrv); and lacrimal gland (LacrimalG).*

### 5.3.2 Patient set-up verification

Figure 5.4 shows the box plots of positional differences between CBCT-CT and CBCT-sCT in translation and rotation. The mean positional differences in all directions were 0.0 mm for translation and 0.0° for rotation. The range of translational shifts were between [0.2: -0.7 mm], [0.6: -0.3 mm], and [0.6: -0.8 mm] in the X, Y, and Z directions, respectively. The range of rotational shifts were between [0.9: -0.9º], [0.6: -0.5º], and [0.5: -1º] in the pitch, yaw and roll, respectively. The 95% confidence intervals were ranging from 0.04 mm to -0.04 mm and 0.03º to -0.05º for translations and rotations, respectively.

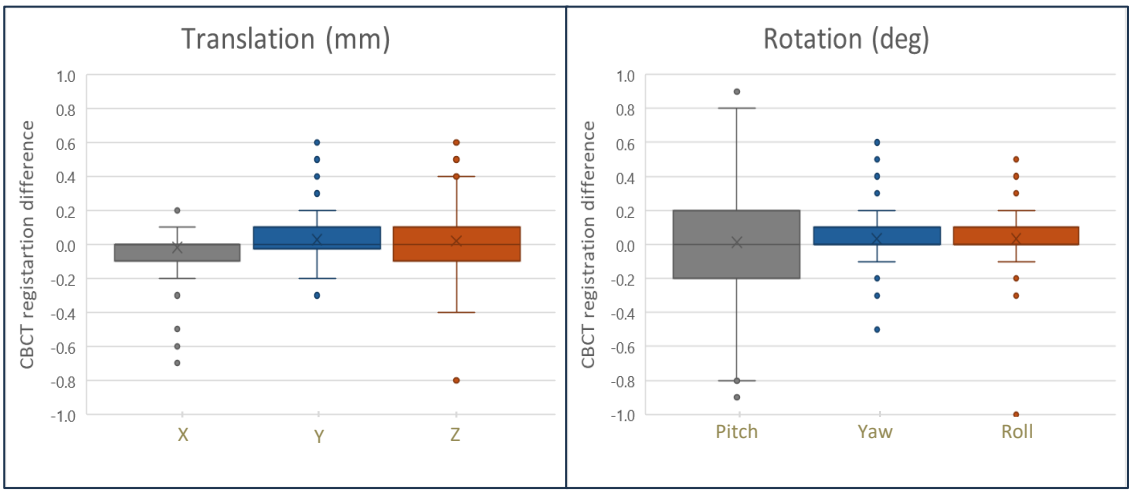


**Figure 5.4: Shows Box plots position error differences between CBCT-sCT minus CBCT-CT for (A) translation and (B) rotation in all direction. The box represents the IQR, the horizontal line indicates the median, whiskers show values within 1.5 times the IQR, and the outliers represented as points.**

## 5.4 Discussion

This study aims to assess the dosimetric accuracy and patient setup verification of MRCAT Brain and demonstrate its clinical feasibility for MRI-only RTP. Compared to previous studies, this study evaluated a large cohort of 94 patients and demonstrated the model's generalisability and suitability for brain MRI-only RTP. In addition, the quantitative assessment of patient setup verification in CBCT registration using a commercially available positioning software system remains unaddressed. This study, for the first time in the literature, evaluated the performance of the Elekta XVI system on a cohort of 70 patients to ensure it is suitable for using sCT as a reference image. Overall, dosimetric and patient setup evaluations confirm that MRCAT produces accurate sCT images, making it a reliable solution for brain MRI-only

radiotherapy. Brain MRCAT met all evaluation criteria, with no clinically significant difference indicated by 95% confidence intervals (considered to be <±2%) [18].

Multiple commercially available solutions have been introduced by vendors for clinical use. Several studies have assessed their clinical feasibility and implementation, reporting relative mean dose differences ranging from -0.7% to 0.5% for PTV and -1.4% to 1.7% for OARs [8, 12-15, 19, 20]. Compared to these findings, this study found significantly better mean dose differences in the PTV and all relevant OARs.

Although relative mean dose differences were found to be clinically acceptable, there were two notable outliers in PTV dose differences (2% for $D_2$% and -2.1% for $D_{98}$%). These two cases are not suitable for clinical use due to gross sCT failures, mainly due to missing bone at nasal cavity or surgical sites. In Case 1, there was no clear cause visible on the MRI; however, this region is known to be challenging due to the presence of both air and bone, which may have contributed to inaccurate bone reconstruction by the MRCAT model. A key reason is that MRCAT relies on Dixon MRI sequences, which differentiate between fat and water but do not provide direct bone contrast, especially for small bones and dense tissue. In Case 2, the patient had undergone major surgery, and a section of the skull was replaced with a metal mesh. Although the MRI has no obvious artefact, the anatomy was likely very different from usual bone structure, which may have caused MRCAT to fail in reconstructing the bone correctly in that region. Therefore, to clinically implement MRCAT Brain, an effective quality assurance (QA) method is needed to identify patients who may experience these dose differences.

OARs outliers were also observed in two patients, with dose differences exceeding ±2%. The first patient showed a dose difference of -3.6% in the right orbit and -7.6% in the right lens. This patient's MRCAT source showed a signal void, possibly due to eye cosmetics distorting the magnetic field, which led to the complete loss of soft tissue in the right orbit and partial loss in the left orbit. This resulted in a significant anatomical sCT failure and led to dosimetric errors in the eye regions. The second patient showed a dose difference of -2.6% in the left lacrimal gland due to the gland’s small size being located on a steep dose gradient next to bone with slight difference in bone densities. In addition, there

was patient positional difference, resulting in external body contouring discrepancy of 0.6 cm on average, contributing to the observed dose difference. Our results showed smaller mean dose differences compared to previous studies that included these OARs. One study reported relative mean dose differences of ≤ ±0.7% in orbit, lens, and cochlea [20]. Another study found -1.1% and -0.9% in the left and right cochlea, respectively [8]. These regions are among the most challenging in MRI-only brain radiotherapy due to their small size, sensitivity to positional differences, and bone and air interfaces. As shown in Figure 5.3, the sCT plans delivered colder dose in the lacrimal gland and cochlea of up to -1.5% compared to CT plans, indicating systematic difference in the sCT plans, as these are bone heavy regions where it is challenging to obtain accurate density information. Although our results show that these differences are considered clinically acceptable, it is important to note that they are more uncertain than those observed in other OARs and PTVs.

In general, common artefacts associated with sCT generated from AI were observed in the brain [9, 21-23]. These artefacts include issues such as missing nasal bone, and skull bone due to surgical clips; differences in the external contour due to patient positioning; variations in bone density in the ear canal; and misclassification of bone and air. However, these artefacts were small and clinically insignificant, considering dose differences between sCT and CT within ±2%.

For patient setup verification, the translational and rotational differences between sCT/CBCT and CT/CBCT were less than ±1 mm and ±1°in all directions. These results are comparable to, or better than, reported studies based on CBCT patient positioning using Eclipse TPS which range from -0.3 to 0.5 mm [12, 15] and -2 to 2.5 mm [10], and -0.3 to 0.3° [12] and -1 to 0.5°[19]. In contrast, two studies based on 2D/2D kV imaging using Brainlab observed larger differences, with translational shifts of 5 mm and rotational errors of 4°[13, 14]. In this study, the potential errors in the systematic differences were very small, as indicated by the narrow 95% confidence intervals.

When correlating the dosimetric outliers with patient setup accuracy, no significant impact was found. Since the brain is a rigid organ, and image registration primarily relies on bony structures. Minor artefacts such as a missing frontal bone or anatomic anomalies due to surgery did not compromise

the overall quality of CBCT- registration. Although the residual errors were small, we observed that the outliers in the X-direction came from a single patient across multiple fractions, similarly in the Y and Z directions. Therefore, the sCT images generated from MRCAT are an accurate alternative to CT reference for CBCT image registration during treatment, it exceeds acceptable standards with sub-millimetre accuracy.

Despite the overall accuracy was clinically acceptable, four cases (representing 4.3% of cases) showed significant dosimetric errors in the sCT, were 3 out 4 cases showed sCT anatomical errors, making them unsuitable for clinical use. Therefore, this study confirms the necessity to establish a comprehensive QA program to ensure safe clinical implementation for MRI only RTP [21]. Patient-specific QA should be performed by radiographers after MRI simulation to detect any significant sCT artefacts. A second check should then be conducted by medical physicists or dosimetrists prior to treatment planning. It is important to note that AI-generated sCT models may introduce errors and are not always completely reliable. For example, as shown in Figure 5.2(B) middle images, post-surgical changes may cause a minor artifact, such as thinner bone in the skull region, that might be missed during visual assessment alone. Therefore, additional verification steps, such as recalculating dose distributions using CBCT, are recommended to ensure the reliability and accuracy of sCT-based treatment plans. A local QA protocol for sCT commercial solutions has been introduced in the literature [8, 9, 15], highlighting visual assessment of any artefacts that may compromise the image quality of sCT or treatment planning  as discussed above.

## 5.5 Conclusion

This study demonstrated the clinical feasibility of brain MR-only treatment planning using the MRCAT solution as part of the commissioning process. In a large cohort of patients, all evaluated criteria were clinically acceptable with dose differences remained within ±2%, and patient setup verification achieved sub-millimetre and sub-degree precision in patient setup verification using a clinical CBCT registration software for the first time in the literature. However, in 3.2% of cases, MRCAT failed to generate acceptable sCT, requiring careful checking before clinical implementation.

## 5.6 References


[1] Chandarana H, Wang H, Tijssen R, Das IJ. Emerging role of MRI in radiation therapy. Journal of Magnetic Resonance Imaging. 2018;48:1468-78

[2] Weltens C, Menten J, Feron M, Bellon E, Demaerel P, Maes F, et al. Interobserver variations in gross tumor volume delineation of brain tumors on computed tomography and impact of magnetic resonance imaging. Radiother Oncol. 2001;60:49-59. https://doi.org/10.1016/S0167-8140(01)00371-1.

[3] Prabhakar R, Haresh K, Ganesh T, Joshi R, Julka P, Rath G. Comparison of computed tomography and magnetic resonance based target volume in brain tumors. Journal of Cancer Research and Therapeutics. 2007;3:121-3. https://doi.org/10.4103/0973-1482.34694.

[4] Ulin K, Urie MM, Cherlow JM. Results of a multi-institutional benchmark test for cranial CT/MR image registration. Int J Radiat Oncol Biol Phys. 2010;77:1584-9. https://doi.org/10.1016/j.ijrobp.2009.10.017.

[5] Spadea MF, Maspero M, Zaffino P, Seco J. Deep learning based synthetic-CT generation in radiotherapy and PET: A review. Medical physics (Lancaster). 2021;48:6537-66. https://doi.org/10.1002/mp.15150.

[6] Boulanger M, Nunes J-C, Chourak H, Largent A, Tahri S, Acosta O, et al. Deep learning methods to generate synthetic CT from MRI in radiotherapy: A literature review. Physica medica. 2021;89:265-81. https://doi.org/10.1016/j.ejmp.2021.07.027.

[7] Huijben EMC, Terpstra ML, Galapon A, Jr., Pai S, Thummerer A, Koopmans P, et al. Generating synthetic computed tomography for radiotherapy: SynthRAD2023 challenge report. Med Image Anal. 2024;97:103276. https://doi.org/10.1016/j.media.2024.103276.

[8] Emin S, Rossi E, Rooth EM, Dorniok T, Hedman M, Gagliardi G, et al. Clinical implementation of a commercial synthetic computed tomography solution for radiotherapy treatment of glioblastoma. Physics and Imaging in Radiation Oncology. 2024;30:100589. https://doi.org/10.1016/j.phro.2024.100589.

[9] Rossi E, Emin S, Gubanski M, Gagliardi G, Hedman M, Villegas F. Contouring practices and artefact management within a synthetic CT-based radiotherapy workflow for the central nervous system. Radiat Oncol. 2024;19:27. https://doi.org/10.1186/s13014-024-02422-9.

[10] Ranta I, Wright P, Suilamo S, Kemppainen R, Schubert G, Kapanen M, et al. Clinical feasibility of a commercially available MRI-only method for radiotherapy treatment planning of the brain. J Appl Clin Med Phys. 2023;24:e14044. https://doi.org/10.1002/acm2.14044.

[11] Yip TTY, Li Z, Li T. Clinical validation of MR-generated synthetic CT by MRCAT for brain tumor radiotherapy. J Appl Clin Med Phys. 2025;26. https://doi.org/10.1002/acm2.14494.

[12] Lerner M, Medin J, Jamtheim Gustafsson C, Alkner S, Siversson C, Olsson LE. Clinical validation of a commercially available deep learning software for synthetic CT generation for brain. Radiat Oncol. 2021;16:1-11. https://doi.org/10.1186/s13014-021-01794-6.

[13] Levardon M, Autret D, Le Dorze T, Guillerminet C, Dufreneix S. Brain MR-only workflow in clinical practice: A comparison among generators for quality assurance and patient positioning. J Appl Clin Med Phys. 2024:e14583. https://doi.org/10.1002/acm2.14583.

[14] Masitho S, Szkitsak J, Grigo J, Fietkau R, Putz F, Bert C. Feasibility of artificial-intelligence-based synthetic computed tomography in a magnetic resonance-only radiotherapy workflow for brain radiotherapy: Two-way dose validation and 2D/2D kV-image-based positioning. Physics and Imaging in Radiation Oncology. 2022;24:111-7. https://doi.org/10.1016/j.phro.2022.10.002.

[15] Lerner M, Medin J, Jamtheim Gustafsson C, Alkner S, Olsson LE. Prospective clinical feasibility study for MRI-only brain radiotherapy. Frontiers in Oncology. 2022;11:812643. https://doi.org/10.3389/fonc.2021.812643.

[16] Goodfellow I, Bengio Y, Courville A, Bengio Y. Deep learning: MIT press Cambridge; 2016.

[17] The ICRU Report 83: prescribing, recording and reporting photon-beam intensity-modulated radiation therapy (IMRT) 2012 [97-9]. Available from: https://academic.oup.com/jicru/article-lookup/doi/10.1093/jicru/ndq002.

[18] Korsholm ME, Waring LW, Edmund JM. A criterion for the reliable use of MRI-only radiotherapy. Radiat Oncol. 2014;9:1-7. https://doi.org/10.1186/1748-717X-9-16.

[19] Ranta I, Wright P, Suilamo S, Kemppainen R, Schubert G, Kapanen M, et al. Clinical feasibility of a commercially available MRI-only method for radiotherapy treatment planning of the brain. J Appl Clin Med Phys. 2023;24:e14044. 10.1002/acm2.14044.

[20] Yip TTY, Li Z, Li T. Clinical validation of MR-generated synthetic CT by MRCAT for brain tumor radiotherapy. J Appl Clin Med Phys. 2025:e14494

[21] Villegas F, Dal Bello R, Alvarez-Andres E, Dhont J, Janssen T, Milan L, et al. Challenges and opportunities in the development and clinical implementation of artificial intelligence based synthetic computed tomography for magnetic resonance only radiotherapy. Radiother Oncol. 2024:110387

[22] Bird D, Speight R, Andersson S, Wingqvist J, Al-Qaisieh B. Deep learning MRI-only synthetic-CT generation for pelvis, brain and head and neck cancers. Radiother Oncol. 2024;191:110052. https://doi.org/10.1016/j.radonc.2023.110052.

[23] Lerner M, Medin J, Jamtheim Gustafsson C, Alkner S, Siversson C, Olsson LE. Clinical validation of a commercially available deep learning software for synthetic CT generation for brain. Radiat Oncol. 2021;16:66. 10.1186/s13014-021-01794-6.

# Chapter 6 Discussion, future directions, and conclusion

## 6.1 Summary of thesis aims

Since the introduction of MRI into radiotherapy, its use has contributed to improving treatment outcomes [1-3]. One area of MRI use in radiotherapy that has gained increasing attention is MRI-only radiotherapy treatment planning. The development of MRI-only radiotherapy has progressed from a research concept to clinical implementation, as demonstrated in the prostate, where clinical workflows have already been established [4-6]. This suggests it is only a matter of time before MRI-only radiotherapy expand to other treatment sites. At the same time, 4D MRI has emerged as a hot topic in radiotherapy research, due to its ability to capture respiratory motion with high soft tissue contrast. In the context of liver MRI-only radiotherapy, 4D MRI is considered a key requirement as an alternative to 4D CT, which is currently used clinically for motion management. The overall goal of this thesis is to provide clinical evidence that MRI-only radiotherapy is technically achievable, and clinically implementable across different anatomical sites, using either a research-based model or commercial solution to generate sCT images. Regardless of the approach, clinical validation remains essential to ensure both accuracy and patient safety. Three studies were designed to investigate key challenges associated with implementing MRI-only radiotherapy in liver and brain. First, replacing 4D CT with 4D MRI in abdominal radiotherapy requires a thorough understanding of current 4D MRI techniques, which was explored through a systematic review in Chapter 3. This chapter aimed to identify the current techniques, limitations, and barriers to clinical adoption, while also highlighting recent advancements that may encourage further research and clinical investigation. This represents one of the key challenges in implementing MRI-only radiotherapy for the liver. The second challenge is generating high-quality sCT images for the liver, which was evaluated in Chapter 4. This study aimed to assess the full MRI-only clinical workflow, starting from dosimetric evaluation to patient positioning verification compared to the current MRI-CT workflow. To move toward full implementation of MRI-only radiotherapy, Chapter 5 aimed to validate an existing commercial solution (Philips MRCAT Brain). The objective was to assess the clinical feasibility of the MRCAT solution for brain radiotherapy by evaluating its dosimetric and patient positioning performance,

and to identify its limitations and determine whether it meets requirements for routine use in brain MRI-only radiotherapy.

## 6.2 Findings and their implications

### 6.2.1 A systematic review of 4D magnetic resonance imaging techniques for abdominal radiotherapy treatment planning (Chapter 3).

Emerging evidence shows that 4D CT has limitations that can negatively affect liver SABR outcomes and can be unreliable for assessing tumour motion during treatment planning [7-9]. This has led to growing interest in 4D MRI as a potential alternative. While 4D MRI is still under active investigation and has yet to be standardised for clinical use, a variety of acquisition and reconstruction methods have been explored. The systematic review of these techniques presented in Chapter 3, identified five key findings: (1) 4D MRI has the potential to improve abdominal radiotherapy treatment planning for patients by providing more accurate tumour definition and motion assessment compared to 4D CT. However, it would be recommended to validate 4D MRI using both 4D CT and phantoms for a robust and comprehensive assessment. (2) 4D MRI reconstructed from 3D MRI acquisition shows promise as a feasible approach for motion management in abdominal radiotherapy planning in term of spatial resolution. (3) Large slice thickness currently achieved on 4D MRI reconstructed from multi-slice 2D acquisition are unsuitable for clinical purposes. (4) The current barriers for clinical implementation of 4D MRI in radiotherapy are the limited availability of validated commercial solutions and the lack of larger patient cohort studies that directly compare it to 4D CT. These comparisons are essential to highlight the potential clinical benefits of 4D MRI, particularly concerning target volume delineation and radiotherapy plan optimisation. This systematic review highlights the gap in current knowledge regarding the different methods explored for 4D MRI, especially whether these methods meet the clinical requirements for radiotherapy planning and address the barriers to their widespread implementation.

Notably, many researchers have focused on 4D MRI reconstructed from fast 3D acquisitions, which is considered one of the key advantages of 4D MRI over 4D CT. Unlike 4D CT, which is usually reconstructed from 2D slices and is

therefore more prone to artefacts, 4D MRI can use 3D acquisitions that provide isotropic resolution. This results in higher signal-to-noise ratio, better geometric accuracy, and more reliable motion capture, without slice misalignment and more robust sorting into respiratory phases. When using 4D MRI in radiotherapy, several important factors must be considered, including image contrast, geometric accuracy, spatial resolution, and the time required for both acquisition and reconstruction, depending on the intended purpose of 4D MRI such as motion estimation, target delineation, or use in MR-guided radiotherapy (MRgRT) or online adaptation. The trade-offs between these parameters can vary depending on the clinical objective. One common acquisition used in 4D MRI is the stack-of-stars (SOS), which has limited contrast T1 or a mixture of T1 and T2 contrast. Generally, 4D MRI can achieve spatial resolution of less than 1.5 mm in-plane and less than 3 mm slice thickness. Scan times vary but are often under 8 minutes, while reconstruction time for 3D acquisition can take up to 10 minutes. To maintain spatial fidelity, geometric distortion correction needs to be applied. Although 4D MRI is now commercially available from Siemens, other vendors have not yet released clinical solutions, and its widespread adoption remains limited. Clear recommendations are therefore needed to support safe and successful clinical implementation.

In May 2025, the systematic review search was updated to include studies published from 2024 to May 2025. Nine additional papers were identified and met the inclusion criteria, as described in Chapter 3. Seven studies investigated advances in 3D time-resolved 4D MRI reconstruction using deep learning or motion modelling methods [10-16]. Two studies proposed multitasking MRI techniques for abdominal radiotherapy planning that generate both T1w and T2w contrasts within a single 4D MRI acquisition, which enhance tumour delineation, with early clinical feasibility demonstrated in liver SABR [10, 14]. Two studies use deep learning methods to accelerate reconstruction and improve image resolution for 4D MRI [11, 13]. Further development of ultra-quality 4D MRI has been investigated, enabling more accurate tumour contouring and improved dosimetric accuracy compared to 4D CT in liver cancer [12, 15]. Another study investigated 4D MRI with enhanced T1w contrast [16]. While the majority of recent work has focused on 4D MRI reconstructed from 3D acquisitions, two studies investigated multislice 2D MRI acquisition [17,

18]. One study developed a reconstruction method for 4D MRI fingerprinting, a growing technique that provides both motion information and quantitative mapping [18]. Another study evaluated the feasibility and clinical outcomes of two-phase T2w 4D-MRI using amplitude-triggering techniques for liver metastases [17]. Overall, these studies add to the understanding of 4D MRI development, especially by contributing early clinical outcome evidence and demonstrating new technical directions, and they also underline the importance of 4D MRI in radiotherapy treatment planning for accurate tumour delineation and motion management. However, they did not change the main conclusions of the systematic review.

### 6.2.2 sCT images evaluation for liver and brain MRI-only radiotherapy (Chapter 4 and 5)

The accuracy of sCT images was evaluated in two clinical sites: liver and brain radiotherapy to determine their suitability for MRI-only radiotherapy. Both dosimetric accuracy and patient positioning verification were assessed, as these are critical requirements for clinical implementation. For the liver, sCTs were generated using a deep learning model integrated into a research version of a commercial TPS, which is independent of the MRI vendor and sequence used. The same DL architecture, described in Chapter 4, had previously been evaluated dosimetrically only for the brain, pelvis, and head and neck sites [19], demonstrating its robustness and generalisability. A recent review on AI-based sCT generation recommended that sCTs should achieve high accuracy for both dose calculation and patient positioning [20], as demonstrated in Chapter 4. To the best of our knowledge, no previous study has evaluated patient positioning verification of sCT images for the liver. Achieving accurate and reliable sCT images, however, requires training and validation on clinical MRI/CT datasets, with performance influenced by the size, quality, and diversity of the training data [20]. In contrast, the availability of commercial solutions from vendors can help accelerate the transition to routine clinical practice, as they have already been trained and validated on clinical CT/MRI datasets and are ready to generate sCT images directly from the provided MRI data, as described in Chapter 5. Brain sCT images (MRCAT) were retrospectively collected for the pre-commissioning phase and evaluated for both dosimetric accuracy and patient positioning in a large patient cohort, and using clinical positioning XVI

software for the first time. The following sections present each evaluation for the liver and brain sites.

#### 6.2.2.1 Dosimetric accuracy

Dosimetric accuracy is considered clinically critical, as errors in dose calculation can directly impact treatment efficacy and patient safety. In Chapter 4, a CycleGAN-based model, trained using a combination of paired and unpaired MRI/CT data, was used to generate sCT images for liver. Dose distributions calculated on CT were recalculated on sCTs and compared using DVH statistics. Overall, the results showed excellent agreement, with relative mean dose difference of 0.0% (range from -1.4% to 1.3%) for PTV D95% and less than -0.5% (range from -2.4% to 1.6%) for all OARs. These results demonstrated that the sCT images produced clinically insignificant dose differences, with small 95% confidence intervals (defined as dosimetric uncertainty of sCT being within ±2% of CT [21]), except one case showed -2.4% in small bowel as discussed in Chapter 4. This performance was achieved despite challenges such as abdominal motion, internal gas, image registration differences between MRI and CT, and the use of a relatively small training dataset. This demonstrates the robustness and clinical relevance of the model where large datasets are not available. In Chapter 5, sCTs generated using the commercial MRCAT solution for brain radiotherapy showed relative mean dose differences of less than 0.4% for all PTV statistics (range: 0.1% to 0.5%) and less than 0.3% for all OARs (range: –0.2% to 0.3%). Similar to liver sCT, these results demonstrated that the MRCAT images produced clinically insignificant dose differences, with small 95% confidence intervals. Given the relatively rigid anatomy of the brain and the reliability of the commercial model, this high level of dosimetric agreement was expected and supports the suitability of MRCAT for clinical use. Notably, this evaluation was performed on a large patient cohort of 93 cases, further confirming the robustness and generalisability of the solution. Both methods produced clinically acceptable results, but the brain sCTs demonstrated slightly higher consistency in dose distribution than the liver cases. This likely reflects anatomical differences, since non-rigid organ motion and air-pocket variations in the abdominal cavity introduce additional challenges. Overall, in this thesis the findings demonstrate that both research and commercial sCT generation methods can provide dosimetric accuracy

suitable for MRI-only workflows, supporting their clinical translation for liver and brain radiotherapy.

#### 6.2.2.2 Patient positioning verification

Following the evaluation of dosimetric accuracy, the next step in validating the MRI-only workflow was to determine whether sCT images can also serve as a reliable reference for patient setup before treatment delivery. Patient positioning verification was therefore assessed by comparing sCT and CT as reference images for 4D-CBCT/3D-CBCT registration within the clinical XVI system. In Chapter 4, systematic differences relative to CT were <0.5 mm in all translational directions and <0.5° in rotation. These differences remained within clinically acceptable thresholds for correction, despite challenges from abdominal motion and the limited quality of 4D CBCT imaging. In Chapter 5, differences were minimal within ±1 mm translationally and ±0.1° rotationally, as expected in regions with minimal anatomical variation. While liver cases showed slightly greater variability than brain, the differences were still not clinically significant and can be due to motion artefacts, suboptimal image quality of sCT or patients positioning differences between MRI and CT. Importantly, sCT images provided sufficient anatomical detail to support accurate and reliable patient setup in both anatomical sites. The use of sCT as a reference in standard clinical software such as XVI further supports the feasibility for liver and brain MRI-only workflows. To date, no prior studies have evaluated sCT-based CBCT registration for patient setup in liver; most have focused either on dosimetry or image quality. This work therefore provides the first evidence that sCT can be used not only for dose calculation but also for patient positioning in liver radiotherapy. Similarly, this is the first study to evaluate MRCAT for brain radiotherapy in a large patient cohort using clinical XVI system, which support its applicability in clinical workflows. Overall, the findings demonstrate that sCT images generated from both research and commercial models can successfully serve as reference images for XVI-based CBCT positioning verification in brain and liver cancer patients, underlining their suitability for MRI-only radiotherapy.

## 6.3 Limitations

While this thesis aimed to assess key challenges associated with liver and brain MRI-only radiotherapy, several limitations should be acknowledged.

### 6.3.1 4D MRI Systematic Review

The systematic review of 4D MRI methodologies for abdominal radiotherapy is not without limitations, as discussed in Chapter 3. Many 4D MRI methods have been developed within MRgRT, such as for abdominal and lung applications. However, due to specific interest in liver, the scope of this systematic review was limited to abdomen. Although the primary focus of this review was the use of 4D MRI in radiotherapy treatment planning, some of the proposed methods have already been clinically implemented in MRgRT and could be adapted for MRI simulation. This suggests that useful information from MRgRT applications may not have been fully captured in this systematic review. Examples of actual clinical use include multi-slice 2D based 4D MRI [22, 23] and 3D acquisition based 4D MRI [24].

### 6.3.2 Technical limitations of the DL model for liver sCT

**I.** Limited training and testing cases: The retrospective MRI data collected were not all suitable for training the model, as some had an insufficient FOV. For example, in some MRI cases, the liver slices were outside the FOV coverage. Although the model was trained on a small number of cases, it still achieved clinically acceptable accuracy. It is expected that more testing data would improve its robustness and generalisability to a wider liver patient population.

**II.** Sub-optimal MRI image quality: A certain degree of variation in image quality is actually desirable in the training dataset, as it can strengthen the model's robustness [20, 25]. In Chapter 4, for example, many of the poor quality MRI images were caused by motion artefacts, often due to patients unable to sustain breath hold during their image acquisition. As a result, sub-optimal image quality made it more difficult to accurately register the MRI data with the corresponding CT simulation images. While the DL model doesn't depend entirely on paired CT-MRI training data, any mismatch between the two can still influence how well it performs. To reduce the impact of positioning differences, deformable image registration was applied, which helped to better align the datasets. However, these limitations appear not to have significant differences on the overall accuracy of the final sCT output.

**III.** The deep learning model used to generate sCT images for the liver is still at the research stage, is not commercially available, and has not been CE-

marked. Thus, it is not intended for clinical implementation at this time. All of MRI training data came from Semiens scanner; however, at our centre all liver patients have since been moved to a Philips MRI simulator that uses a different liver sequence (Dixon). Therefore, the model would need to be retrained to be applicable to this data. However, the evaluation of the sCT in this study provides other researchers and clinicians a benchmark for the level of image quality that can be achieved in synthetic CT generation for the liver, which demonstrates the technical feasibility of implementing liver MRI-only radiotherapy.

### 6.3.3 Challenges in sCT evaluation metrics

Dose assessment focused solely on DVH metrics, without including gamma index analysis. However, additional analyses would not have changed the study's conclusions as the dosimetric differences between sCT and CT were found to be minimal. Overall, the evaluation addressed the main research questions and demonstrated clinically acceptable results. These findings support the suitability of the generated sCT images for MRI-only radiotherapy in both the liver and the brain.

### 6.3.4 MRI-only considerations

While this work demonstrated high dosimetric accuracy and reliable patient positioning of the sCT for both liver and brain, several potential advantages and practical aspects of an MRI-only workflow were not directly assessed. For example, one key advantage is the elimination of CT-MRI registration errors, which was not measured in this thesis. Including such an analysis could expand the clinical impact and provide practical evidence for centres considering adoption of MRI-only radiotherapy.

## 6.4 Future research directions

### 6.4.1 Future work related to 4D MRI in radiotherapy

From the comprehensive systematic review, it is clear that further research is required before 4D MRI can be widely implemented in abdominal radiotherapy. For example, further work is needed to validate 4D MRI against 4D CT and motion phantoms with range of motion, establish standardised acquisition protocols to ensure reliable motion quantification, and evaluate its

impact on treatment planning and delivery. Clinical validation in liver patients will require prospective evaluation of 4D MRI compared to standard 4D CT in terms of geometric, motion metrics, dosimetric impact.

Another promising area for 4D MRI is its use not only for motion assessment but also for dose calculation through the generation of 4D sCT. Recent research has explored the feasibility of producing 4D sCT from 4D MRI using deep learning models, which could offer several potential benefits including supporting MRI-only radiotherapy for liver, dose calculation is possible for each respiratory phase, and dose accumulation. Future work should also consider alternatives to the conventional ITV method from 4D CT, which can be overly conservative for large breathing amplitudes. The mid-ventilation (MidV) approach, recommended by the British Institute of Radiology [26], treats breathing motion as a random error, potentially improving OAR sparing or enabling dose escalation without compromising target coverage.

### 6.4.2 Future work related to liver MRI-only radiotherapy planning

This study addressed a key technical challenge for liver MRI-only radiotherapy, which is the validation of sCT generation, and it demonstrated clinically acceptable accuracy. However, further work is needed to develop liver MRI-only radiotherapy and support its wider clinical implementation. An interesting area for investigation is the evaluation of the current model using Dixon sequences, as explored in Chapter 4, using larger training and validation cohort to determine whether different MR acquisition can improve model performance and the overall sCT quality. To facilitate wider adoption of MRI-only radiotherapy, it is important to provide evidence of the potential benefits of eliminating MRI-CT registration errors by quantifying these errors and assessing their clinical impact. Additionally, there is growing interest in exploring liver MRI quantitative imaging biomarkers derived from advanced MRI sequences. Integrating such biometrics into MRI-only planning pathways could further enhance personalised treatment and improve patient outcomes.

### 6.4.3 Future work related to brain MRI-only radiotherapy planning

At LCC, the implementation of a dedicated MRI simulator represents a major step towards the department’s goal of commissioning MRI-only radiotherapy planning across several treatment sites. This work provides strong

evidence that the Philips MRCAT solution is suitable for clinical use. Building on these findings, clinical implementation has already begun, and the first patients have been treated with brain MRI-only radiotherapy, to which this thesis has made a significant contribution. However, prospective studies are required to evaluate MRI-only workflows following the clinical implementation and to identify any limitations that may arise in routine clinical practice. Long-term validation of the Philips MRCAT solution will also be essential to ensure its safety, accuracy, and sustainability in routine use. Another area for potential future research is to add a spin echo (SE) sequence as an additional check for the QA protocol. This is because this sequence is less sensitive to air–tissue interfaces and eye makeup artefacts than the gradient echo mDixon used in MRCAT. It would also be worth investigating whether automated segmentation of brain structures could be integrated into MRI-only workflows to speed up planning even further. Finally, functional MRI could be explored as a way to improve tumour visualisation, predict how well patients will respond, and track treatment progress over time. More research is needed to investigate the potential benefits of brain MRI-only radiotherapy by assessing registration uncertainties, economics benefit and time saving compare to the current CT-MRI workflow. This could help many centres decide on the adoption of MRI-only workflows, clarify the potential benefits for patients, and facilitate its widespread clinical implementation.

## 6.5 Conclusion

The interest in MRI-only radiotherapy has grown significantly in recent years, driven by its potential to improve target delineation, eliminate CT-MRI registration errors, streamline the treatment planning process, and enable a single imaging appointment, which is more convenient for patients, and efficient for healthcare providers. This thesis has contributed to the growing field of MRI-only radiotherapy by addressing key challenges and demonstrating the technical feasibility and clinical suitability of liver and brain MRI-only radiotherapy.

To enable a fully MRI-only workflow for liver cancer radiotherapy, several challenges still need to be addressed, including the development and validation of 4D MRI to replace 4D CT for respiratory motion management, and the need for reliable commercial sCT solutions for the liver. The literature is promising,

with many methods and techniques proposed to integrate 4D MRI into clinical practice. The systematic review presented in this thesis, published as “A systematic review of 4D magnetic resonance imaging techniques for abdominal radiotherapy treatment planning” [27], demonstrated that 4D MRI is technically feasible for clinical implementation.

Another key challenge is that sCT generation must also achieve dosimetric accuracy suitable for clinical use, and must allow sCT to replace CT as the reference image for patient treatment position verification. In this study, sCT generation for liver cancer was shown to be technically achievable, with dose differences relative to the planning CT within 2%, which is considered clinically acceptable. This study also introduces the first published evaluation of sCT-based patient positioning for liver radiotherapy, using the clinical XVI system to replicate the current workflow using sCT images. The results demonstrated excellent positioning agreement when compared with CT reference. These findings, presented in the publication “Evaluating the dosimetric and positioning accuracy of a deep learning-based synthetic-CT model for liver radiotherapy treatment planning” [28]. showed an essential step supporting the clinical implementation of MRI-only radiotherapy for liver cancer.

Similar validation steps were undertaken to evaluate the clinical suitability of the Commercial MRCAT solution, representing an important step toward the safe clinical implementation of brain MRI-only radiotherapy. This study demonstrated the robustness and generalisability of the MRCAT product for clinical use, with consistent performance across a large number of cases. The evaluation demonstrated high dosimetric accuracy and minimal systematic registration errors for patient positioning verification. Importantly, this work provides the first published evidence in the literature of using CBCT-based image registration with the clinical XVI system for brain MRI-only radiotherapy, representing a solid method with direct applicability in clinical practice. These findings were presented in the publication “Clinical validation of using a commercial synthetic-computed tomography solution for brain MRI-only radiotherapy treatment planning” [29].

The work presented in this thesis provides technical validation and clinical evidence of clinically applicable methods that bring MRI-only

radiotherapy for the liver and brain closer to routine clinical implementation, with the ultimate goal of improving treatment planning precision and patient care.

## 6.6 Reference


[1] Chandarana H, Wang H, Tijssen R, Das IJ. Emerging role of MRI in radiation therapy. Journal of Magnetic Resonance Imaging. 2018;48:1468-78

[2] Li M, Zhang Q, Yang K. Role of MRI-based functional imaging in improving the therapeutic index of radiotherapy in cancer treatment. Frontiers in Oncology. 2021;11:645177

[3] Dirix P, Haustermans K, Vandecaveye V, editors. The value of magnetic resonance imaging for radiotherapy planning. Seminars in radiation oncology; 2014: Elsevier.

[4] Korhonen J, Visapää H, Seppälä T, Kapanen M, Saarilahti K, Tenhunen M. Clinical experiences of treating prostate cancer patients with magnetic resonance imaging–only based radiation therapy treatment planning workflow. International Journal of Radiation Oncology, Biology, Physics. 2016;96:S225

[5] Persson E, Jamtheim Gustafsson C, Ambolt P, Engelholm S, Ceberg S, Bäck S, et al. MR-PROTECT: Clinical feasibility of a prostate MRI-only radiotherapy treatment workflow and investigation of acceptance criteria. Radiation oncology (London, England). 2020;15:77-13. 10.1186/s13014-020-01513-7.

[6] Tyagi N, Fontenla S, Zelefsky M, Chong-Ton M, Ostergren K, Shah N, et al. Clinical workflow for MR-only simulation and planning in prostate. Radiat Oncol. 2017;12:119. 10.1186/s13014-017-0854-4.

[7] Sentker T, Schmidt V, Ozga A-K, Petersen C, Madesta F, Hofmann C, et al. 4D CT image artifacts affect local control in SBRT of lung and liver metastases. Radiother Oncol. 2020;148:229-34. 10.1016/j.radonc.2020.04.006.

[8] Dhont J, Vandemeulebroucke J, Burghelea M, Poels K, Depuydt T, Van Den Begin R, et al. The long- and short-term variability of breathing induced tumor motion in lung and liver over the course of a radiotherapy treatment. Radiother Oncol. 2018;126:339-46. 10.1016/j.radonc.2017.09.001.

[9] Yamamoto T, Langner U, Loo BW, Jr., Shen J, Keall PJ. Retrospective analysis of artifacts in four-dimensional CT images of 50 abdominal and thoracic radiotherapy patients. Int J Radiat Oncol Biol Phys. 2008;72:1250-8. https://doi.org/10.1016/j.ijrobp.2008.06.1937.

[10] Chen JZ, Christodoulou AG, Han P, Xiao JY, Han F, Hu ZH, et al. Abdominal MR Multitasking for radiotherapy treatment planning: A motion-resolved and multicontrast 3D imaging approach. Magn Reson Med. 2025;93:108-20. 10.1002/mrm.30256.

[11] Zhi SH, Wang YH, Xiao HN, Bai T, Li B, Tang YS, et al. Coarse-Super-Resolution-Fine Network (CoSF-Net): A Unified End-to-End Neural Network for 4D-MRI With Simultaneous Motion Estimation and Super-Resolution. Ieee Transactions on Medical Imaging. 2024;43:162-74. 10.1109/tmi.2023.3294245.

[12] Li S, Zhu X, Xiao H, Liu W, Zhang Y, Cai J, et al. Dosimetric investigation of multi-parametric 4D-MRI for radiotherapy in liver cancer. Radiat Oncol. 2025;20:51

[13] Xu D, Miao X, Liu HJ, Scholey JE, Yang WS, Feng M, et al. Paired conditional generative adversarial network for highly accelerated liver 4D

MRI. Physics in Medicine and Biology. 2024;69. 10.1088/1361-6560/ad5489.
[14] April Chau OW, Geoghegan T, Everts J, Chen J, Feng M, Chen WC, et al. Multi-contrast 4DMR via MR multitasking: Early clinical experience and implication for liver stereotactic body radiation therapy. Radiotherapy and oncology : journal of the European Society for Therapeutic Radiology and Oncology. 2025;206:110839. https://dx.doi.org/10.1016/j.radonc.2025.110839.
[15] Liao Y-P, Xiao H, Wang P, Li T, Aguilera TA, Visak JD, et al. Internal Target Volume Estimation for Liver Cancer Radiation Therapy Using an Ultra Quality 4D MRI. Advances in Radiation Oncology. 2025:101774
[16] Chen JJ, Xia D, Huang CC, Shanbhogue K, Chandarana H, Feng L. Free-breathing time-resolved 4D MRI with improved T1-weighting contrast. Nmr in Biomedicine. 2024;37. 10.1002/nbm.5247.
[17] Wang HZ, Zheng X, Sun JW, Zhu XG, Dong DZ, Du Y, et al. 4D-MRI assisted stereotactic body radiation therapy for unresectable colorectal cancer liver metastases. CLINICAL AND TRANSLATIONAL RADIATION ONCOLOGY. 2024;45. 10.1016/j.ctro.2023.100714.
[18] Wong YL, Li T, Liu C, Lee HFV, Cheung LYA, Hui ESK, et al. Reconstruction of multi-phase parametric maps in 4D-magnetic resonance fingerprinting (4D-MRF) by optimization of local T1 and T2 sensitivities. Medical Physics. 2024;51:4721-35. 10.1002/mp.17001.
[19] Bird D, Speight R, Andersson S, Wingqvist J, Al-Qaisieh B. Deep learning MRI-only synthetic-CT generation for pelvis, brain and head and neck cancers. Radiother Oncol. 2024;191:110052. https://doi.org/10.1016/j.radonc.2023.110052.
[20] Villegas F, Dal Bello R, Alvarez-Andres E, Dhont J, Janssen T, Milan L, et al. Challenges and opportunities in the development and clinical implementation of artificial intelligence based synthetic computed tomography for magnetic resonance only radiotherapy. Radiother Oncol. 2024;198:110387. 10.1016/j.radonc.2024.110387.
[21] Korsholm ME, Waring LW, Edmund JM. A criterion for the reliable use of MRI-only radiotherapy. Radiat Oncol. 2014;9:1-7. https://doi.org/10.1186/1748-717X-9-16.
[22] van de Lindt TN, Nowee ME, Janssen T, Schneider C, Remeijer P, van Pelt VWJ, et al. Technical feasibility and clinical evaluation of 4D-MRI guided liver SBRT on the MR-linac. Radiother Oncol. 2022;167:285-91. 10.1016/j.radonc.2022.01.009.
[23] van de Lindt T, Sonke JJ, Nowee M, Jansen E, van Pelt V, van der Heide U, et al. A Self-Sorting Coronal 4D-MRI Method for Daily Image Guidance of Liver Lesions on an MR-LINAC. Int J Radiat Oncol Biol Phys. 2018;102:875-84. 10.1016/j.ijrobp.2018.05.029.
[24] Paulson ES, Ahunbay E, Chen X, Mickevicius NJ, Chen G-P, Schultz C, et al. 4D-MRI driven MR-guided online adaptive radiotherapy for abdominal stereotactic body radiation therapy on a high field MR-Linac: Implementation and initial clinical experience. Clinical and translational radiation oncology. 2020;23:72-9. https://dx.doi.org/10.1016/j.ctro.2020.05.002.
[25] Spadea MF, Maspero M, Zaffino P, Seco J. Deep learning based synthetic-CT generation in radiotherapy and PET: A review. Med Phys. 2021;48:6537-66. 10.1002/mp.15150.

[26] Tudor GSJ, et al. Geometric Uncertainties in Daily Online IGRT [Available from: https://bir.org.uk/publications/geometric-uncertainties.aspx.

[27] Aljaafari L, Bird D, Buckley DL, Al-Qaisieh B, Speight R. A systematic review of 4D magnetic resonance imaging techniques for abdominal radiotherapy treatment planning. Physics and Imaging in Radiation Oncology. 2024;31:100604. https://doi.org/10.1016/j.phro.2024.100604.

[28] Aljaafari L, Speight R, Buckley DL, Al-Qaisieh B, Andersson S, Bird D. Evaluating the dosimetric and positioning accuracy of a deep learning based synthetic-CT model for liver radiotherapy treatment planning. Biomed Phys Eng Express. 2025;11: 035014. 10.1088/2057-1976/adc818.

[29] Aljaafari L, Speight R, Buckley DL, Bird D, Al-Qaisieh B. Clinical validation of using a commercial synthetic-computed tomography solution for brain MRI-only radiotherapy treatment planning. Technical Innovations and Patient Support in Radiation Oncology. 2025;35:100589. 10.1016/j.tipsro.2025.100328.

# Appendices

**The appendices provide supporting materials referenced throughout the thesis. They are organised as follows:**

Appendix A: Supplementary materials for the systematic review of 4D MRI (Chapter 3).

Appendix B: Additional information for Chapter 3.

Appendix C: Conference participation during my PhD.

Appendix D: LeedsCAT approval letters.

Appendix E: Published paper copy.

# Appendix A Supplementary materials

## Supplementary material A
## Search protocol used for all four databases to obtain relevant studies for the review.

| Databases | # | Search terms |
|---|---|---|
| **Medline** | 1 | (4D or "4 dimen*" or "four dimen*" or cine or cinematic or dynamic).tw |
| **database** | 2 | Magnetic Resonance Imaging, Cine/ |
| | 3 | MR or MRI or "Mag* res* im*").tw. |
| | 4 | 1 and 3 |
| | 5 | 2 or 4 |
| | 6 | (motion or breathing cycle* or "respiratory-correlated MR" or "time-resolved MR" or gated or gating or free-breathing or moving target* or breath-hold*).tw. |
| | 7 | Breath Holding/ |
| | 8 | 6 or 7 |
| | 9 | (RT or radiother* or radi* therapy or "radiation oncology").tw. |
| | 10 | Radiotherapy/ |
| | 11 | 9 or 10 |
| | 12 | 5 and 8 and 11 |
| | 1 | (4D or "4 dimen*" or "four dimen*" or cine or cinematic or dynamic).tw. |

| | | |
|---|---|---|
| **Embase database** | 2 | (MR or MRI or "Mag* res* im*").tw |
| | 3 | cine magnetic resonance imaging/ |
| | 4 | 1 and 2 |
| | 5 | 3 or 4 |
| | 6 | (motion or breathing cycle* or "respiratory-correlated MR" or "time-resolved MR" or gating or gated or free-breathing or moving target* or breath-hold*).tw. |
| | 7 | breathing/ or breath holding |
| | 8 | 6 or 7 |
| | 9 | (RT or radiother* or radi* therapy or "radiation oncology").tw. |
| | 10 | radiotherapy/ |
| | 11 | 9 or 10 |
| | 12 | 5 and 8 and 11 |
| **Scopus** | 1 | (TITLE-ABS-KEY (4d OR “4 dimen*” OR “four dimen*” OR cine OR cinematic OR dynamic) |
| | 2 | TITLE-ABS-KEY (mr OR mri OR “Magnetic resonance imaging”) |
| | 3 | TITLE-ABS-KEY (motion OR “breathing cycle*” OR “respiratory-correlated MR” OR “time-resolved MR” OR gating OR gated OR “free-breathing” OR “moving target*” OR “breath-hold*”) |
| | 4 | TITLE-ABS-KEY (rt OR radiother* OR “radi* therapy” OR “radiation oncology”)) |
| | 5 | 1 AND 2 AND 3 AND 4 |
| **Web of Science** | 1 | (4d OR “4 dimen*” OR “four dimen*” OR cine OR cinematic OR dynamic) (all field) |
| | 2 | (mr OR mri OR “Magnetic resonance imaging”) (all field) |
| | 3 | motion OR “breathing cycle*” OR “respiratory-correlated MR” OR “time-resolved MR” OR gating OR gated OR “free-breathing” OR “moving target*” OR “breath-hold*”) (all field) |
| | 4 | (rt OR radiother* OR “radi* therapy” OR “radiation oncology”) (all field) |
| | 5 | 1 AND 2 AND 3 AND 4 |

## Supplementary material B

**Overview of the key imaging parameters and methodologies used for different abdominal organs to reconstruct 4D MRI from 3D MRI data acquisition**

| Author [ref] | Organ (patient number) | Acquisition type | Image contrast | Surrogate | Binning | Spatial Resolution (Temporal Resolution) | FOV | Scan Time (Recon. Time) |
|---|---|---|---|---|---|---|---|---|
| Stemkens (2015) [10] | Pancreas (6) | 3D RSOS | T2/T1w 3D GRE | 1D nav | 10 Phase | 2.0×2.0×4.0 $mm^3$ (NR) | 330x330x96 $mm^3$ | 8 min 35 s (2 min 44 s) |
| Deng (2015) [11] | Liver (2) | 3D Radial | T1w 3D GRE | SG | 10 Phase | 1.56×1.56×1.56 $mm^3$ RC (300-500 ms) | 300×300×300 $mm^3$ | 8 min (NR) |
| Yang (2015) [12] | Pancreas (10) | 3D Radial | T1w 3D GRE | SG | 10 Phase | 1.56×1.56×1.56 $mm^3$ RC (300-500 ms) | 300×300×300 $mm^3$ | 8 min (5 hrs) |

| | | | | | | | | |
|---|---|---|---|---|---|---|---|---|
| Feng (2016) [13] | Liver (1) | 3D RSOS | T1w 3D GRE | SG | 4 Phase | 1.1×1.1×3 $mm^3$ (NR) | 360×360×240 $mm^3$ | ~95 s (~15 min/slice) |
| Jin (2016) [14] | Pancreas (9) | 3D Radial | T1w 3D GRE | SG | 10 Phase | 1.6x1.6x1.6 $mm^3$ RC (300-500 ms) | 300x300x300 $mm^3$ | 8 min (NR) |
| Deng (2017) [15] | Liver (1) Pancreas (3) | 3D Radial | T1w 3D GRE | SG | 10 Phase | 1.56×1.56×1.56 $mm^3$ (NR) | 400x400x400 $mm^3$ | 7 min 23 s (NR) |
| Stemkens (2017)[16] | Kidney (5) | 3D RSOS | T2/T1w 3D GRE | SG | 10 Phase | 1.9×1.9×2 $mm^3$ TR (360 ms) | 300–350×300 – 350×132– 200 $mm^3$ | 3 min 22 s – 5 min 3 s (NR) |
| Breuer (2018)**[17]** | Liver (2) | 3D Cartesian | T1w 3D GRE | SG | 10 Amplitude | 2.1×2.1×2.1 $mm^3$ (NR) | 400×400×185 $mm^3$ | 5 min 36 s (NR) |
| Oar (2018) [18] | Liver (5) Pancreas (3) | 3D RSOS | T1w 3D GRE | SG | 5 Amplitude | 1.2×1.2×3.0 $mm^3$ (NR) | 380×380 $mm^2$ | 5 min (NR) |
| Yang (2018) [19] | Pancreas (10) | 3D Radial | T1w 3D GRE | SG | 10 Amplitude | 1.56×1.56 ×1.56 $mm^3$ RC (300-500 ms) | 400×400×400 $mm^3$ | 5 min (8 hrs) |

| | | | | | | | | |
|---|---|---|---|---|---|---|---|---|
| Deng (2019) [20] | Liver (1)<br>Pancreas (7) | 3D RSOS | T1w<br>3D GRE | SG | 10 Amplitude | 1.98x1.98x1.98 $mm^3$<br>(NR) | 380 ×380×206 $mm^3$ | 9 min (NR) |
| Mickevicius and Paulson<br>(2019) [21] | Liver (3) | SR -SOPI | T1w 3D<br>GRE | 1D nav | 6 Phase | 2.5 $mm^3$ to 2.9 $mm^3$<br>(NR) | 360 x 360 $mm^2$ | 6 min<br>30 s (80 min) |
| Stemkens<br>(2019)[22] | Kidney (5) | 3D RSOS | T2/T1w 3D GRE | SG | 5 Amplitude and Phase | 1.9×1.9×4.0 $mm^3$<br>(NR) | 300×300×200 $mm^3$ | 3.5-5 min (NR) |
| Navest (2020)[23] | Pancreas (1) | 3D RSOS | T1w<br>3D GRE | Noise nav | 7 Phase | 1.3x1.3x3 $mm^3$<br>(NR) | 400x197x400 $mm^3$ | NR |
| Weick (2020)[24] | Liver and adrenal gland (4) | 3D Cartesian | T1w<br>3D GRE | SG | 10<br>Amplitude | 2.1x2.1x2.1 $mm^3$<br>(NR) | 400×400×185 $mm^3$ | 3-5 min /<br>330 min |
| Feng (2021)[25] | Liver (15) | 3D RSOS | T1w<br>3D GRE | SG | 10 Amplitude | 1.25×1.25×5 $mm^3$<br>1.50×1.50×4 $mm^3$<br>TR (300ms) | 320×320 $mm^2$<br>384×384 $mm^2$ | 2 min 18s<br>8.5 min<br>(73.82 min) |
| Freedman<br>(2021)[26] | Liver (3)<br>Pancreas (17) | 3D RSOS | T1w<br>3D GRE | SG | 16 Phase | 1.25x1.25x3.3 $mm^3$<br>(NR) | 400×400 $mm^2$ –<br>480×480 $mm^2$ | 4 min 21s –<br>5 min 45 s |

| | | | | | | | | |
|---|---|---|---|---|---|---|---|---|
| | | | | | | | | (28 s) |
| Romaguera, (2021)[27] | Liver (11) | 3D RSOS | T2/T1w 3D GRE | SG | 10 Phase | 1.5×1.5×5 $mm^3$ (NR) | 450×450×250 $mm^3$ | 3 min (NR) |
| Mansour (2022)**[28]** | Liver (11) | 3D RSO | T2/T1w 3D GRE | SG | 10 Phase | 2×2 ×2.5 $mm^3$ TR (450ms) | NR | 8 min (10 hrs) |
| Thomas (2022)**[29]** | Liver (12) | 3D RSOS | T1w 3D GRE | SG | 4 amplitude[1] | 1.3x1.3x3 $mm^3$ (NR) | 480 x 480 $mm^2$ | 8–10 min (NR) |
| Wong (2022)**[30]** | Liver (2) Pancreas (1) | 3D Cartesian | T1w 3D GRE TWIST | rPPV | NR | 2.7x2.7x4.5 to 3x3x5 $mm^3$ TR (333 ms) | 350-382 $mm^2$ | NR |
| Xiao (2022)**[31]** | Liver (39) | 3D Radial | T1w 3D GRE TWIST | BA | 10 Phase | 2.7×2.7×2.7 $mm^3$ (NR) | NR | 50s (NR) |
| Feng (2023)**[32]** | Liver (7) | 3D RSOS | T2/T1w 3D GRE | 2D nav | 10 Phase | 1.4×1.4x5 $mm^3$ TR (0.3s/volume) | 360 × 360 $mm^2$ | 2 min 49 s (NR) |
| Liu (2023)**[33]** | Liver (7) | 3D RSOS | T2/T1w 3D GRE | SG | 21 Phase | 2-2.45 x 2-2.45 x 3-4 $mm^3$ | 192 x 192 $mm^2$ | 5 min (4.5 min) |

| | | | | | | | | |
|---|---|---|---|---|---|---|---|---|
| | | | | | | TR (340 ms) | | |
| Murray (2023)**[35]** | Abdominal tumours (21) | 3D RSOS | T1w<br><br>3D GRE | SG | 4 and 10 amplitudes | 1.25–1.5 x 1.25–1.5 x4–5 mm<br><br>(NR) | NA | ~1- 2.25 min (0.69 and 0.75s) |
| Xiao (2023)[34] | Liver (43) | 3D Cartesian | T1w<br><br>3D GRE TWIST | BA[2] | 10 Phase | 2.7 x 2.7 x 2.7 $mm^3$<br><br>TR (500 ms) | 432 x 345 x 172 $mm^3$ | 49.6 s (3 s) |
| | Liver (5) | 3D Cartesian | T1w<br><br>3D GRE<br><br>THRIVE | NR | NR | 3.0 x 3.0 x 3.0 $mm^3$<br><br>TR (500 ms) | 420 x 420 x 159 $mm^3$ | 64 s (NR) |

***Abbreviations***: NR: not reported, min: minutes, hrs: hours, RSOS: 3D Radial stack-of stars, nav: navigator, SG: Self-gating, SR-4D-SOPI: Super-resolution simultaneous orthogonal plane imaging, TWIS: time-resolved imaging with interleaved stochastic trajectories, rPPV: The respiratory positional probability volume, Recon: reconstruction RC: Respiratory correlated. TR: Time resolved.

[1] Amplitude binning: Two-directional amplitude where the data in each amplitude bin is divided into inspiration and expiration groups based on the motion direction.

[2] Body area (BA): an internal motion surrogate, which is using changes of body surface area to extract the breathing signal.

## Supplementary material C

**Summary of the key findings from 4D MRI reconstructed from 3D MRI data acquisition**

| Author (Year) [Ref] | Validation comparing to 4DMR | Validation metrics | Other key information | |
|---|---|---|---|---|
| | | | **Motion and volume** | **Overall image quality of proposed 4DMRI** |
| Stemkens (2014) [10] | NA | Peak-to-Peak motion | -7.4 ± 1.6 mm duodenum.<br>-5.4 ± 0.7 mm tumour | (1) MRI navigator more accurate than respiratory bellows.<br>(2) Radial sampling reduced undersampling and artifacts |
| Deng (2015) [11] | real-time 2DMRI | Tumour CC | 0.938 (SI), < 0.8 (AP, LR) | (1) Less overall image quality (i.e. signal inhomogeneity) and variation in tissue contrast<br>(2) No statistically significant difference in image sharpness |
| | | MAD | ≤ 1.2 mm in (SI) | |
| | | MDD | <-0.8 mm (SI),<-1.6 mm (AP),< -0.7 mm (LR) | |
| Yang (2015) [12] | real-time 2DMRI | Tumour CC | 0.9 ± 0.0 (SI), 0.8 ± 0.1 (AP), 0.7 ± 0.18 (LR) | (1) Free of stitching artifacts |
| | | MAD | 0.8 ± 0.5 mm (SI), 0.4 ± 0.2 mm (AP), 0.5 ± 0.2 mm (LR) | |
| | 4DCT | Tumour CC | 0.9 ± 0.06 (SI), 0.7 ± 0.16 (AP), 0.4 ± 0.2 (LR) | |
| | | MAD | 1.1 ± 0.4 mm (SI), 0.5 ± 0.2 mm (AP), and 0.5 ± 0.3 mm (LR) | |
| | | SD-GTV from 10 phases | 0.8 1± 0.54 $cm^3$ 4DMRI, 1.02 ± 0.67 $cm^3$ 4DCT | |
| Feng (2016) [13] | XD-GRASP vs iGRASP | NA | NA | (1) Improved overall image quality with less motion artifact compared to iGRASP |
| Jin (2016) [14] | de-noised vs raw data 4DMRI | Tumour CC | 0.9994 ± 0.0003 | (1) Improved overall image quality |
| | | SD-GTV from 10 phase | 0.6 ± 0.4 $cm^3$ 4DMRI<br>0.8 ± 0.6 $cm^3$ 4DCT | |

| | | | | |
|---|---|---|---|---|
| Deng (2017) [15] | SS-4D-MRI vs NS-4D-MRI | Tumour CC | 0.96 ± 0.06 (SI), 0.78 ± 0.2 4 (AP) and 0.46 ± 0.44 (RL) | (1) Superior vessel delineation and higher SNR and CR<br>(2) Fewer streaking artifacts (4-point scale) |
| Stemkens (2017) [16] | Motion models[1] vs real-time 2DMRI | mean RMSEs | 2.69 ± 0.68 mm STATIC, 2.37 ± 0.78 mm AVG-RESP ,1.09 ± 0.47 mm PCA model | NA |
| Breuer (2018) [17] | 4DCT | NA | NA | (1) Superior lesion visualisation compared to 4DCT |
| Oar (2018) [18] | 4DCT | Median Tumour ED | 11.2 mm 4DCT,10.1 mm 4DMRI<br>median difference: -0.6 mm | (1) Superior edge detection and over all image quality (four-point scale) |
| Yang (2018) [19] | SS-4D-MRI vs NS-4D-MRI | CC | 0.93 ± 0.10 (SI), 0.65 ± 0.31 (AP), 0.77 ± 0.23 (LR) | (1) Enhanced imaging signal and increased vessel CNR compared to NS-4DMRI and 4DCT |
| Deng (2019) [20] | MoCoAve[2] vs non- MoCoAve | Tumour CC | 0.91 ± 0.08 (SI), 0.51 ± 0.44 (AP), 0.37 ± 0.23 (LR) | (1) Higher SNR, fewer artifacts and increased in overall image quality (3-point scale) (2) No statistically significant difference in image sharpness |
| | | Tumour MAD | 0.5 ± 0.3 mm (SI) | |
| | | SD-GTV from 10 phases | 1.4 8±1.35 cm³ MoCoAve, 2.17±1.31 cm³ non-MoCoAve | |
| Mickevicius and Paulson (2019) [21] | SR reconstructions | NA | NA | (1) The respiratory motion was well-defined without any mismatching of sorted slices |
| Stemkens (2019) [22] | 5DMRI[3], CE-4DMRI vs real-time 2DMRI | SI GTV motion | CE-4DMRI demonstrated approximately 10% smaller motion than real-time 2DMRI | (1) 5DMRI reduced the motion artifact compared to DCE |
| Navest (2020) [23] | Noise-nav vs SG | NA | NA | (1) Less streaking artifacts compared to self-gating |
| Weick (2020) [24] | Dir-Reg[4] vs nn-Reg IR[4] | Median COV all ROIs | Reduced by 5.6% ± 5.3% for exhalation and 7.0% ± 4.2% | (1) Superior overall image quality compared to nn-Reg (4-point scale) |

| | | | | |
|---|---|---|---|---|
| | | | for inhalation compared to the nn-Reg | |
| Feng (2021) [25] | real-time 2DMRI | $R^2$ | 0.948 | (1) Suspected lesions were clearly visible in the 3D images across three planes. |
| Freedman (2021) [26] | 4D-Dracula[5] vs 4D-MoCo[5] | Median tumour ranges | Below 2.4 mm. | (1) Lower overall image quality (2) Clinically acceptable for contouring in RT (four-point scale) |
| | | Median inter-observer DSC | >0.86 GTV | |
| Romaguera (2021) [27] | 4DMRI vs Ultrasound | Volumetric Prediction Mean Error | 1.67 ± 1.68 mm | NA |
| Mansour (2022) [28] | XD-GRASP and DR | NA | NA | (1) The liver motion clearly showed the positions of both the tumour and liver in 10 phases |
| Thomas (2022) [29] | 4DCT | Dosimetric Coverage of PTVs from CT and MRI plans | ▪ No significant difference when optimised on their respective target<br>▪ Statistically significant lower of MRI target compared to CT target when they optimised on CT plan | (1) Equal or better liver tumours clarity at extreme phases (4-point Likert scale)<br>(2) Higher sharpness scores at extreme phases |
| | | Mean liver dose, OAR and ITVs volume | No statistically significant difference between CT and MR optimised plans | |
| Wong (2022) [30] | 4DCT | ITV volume | The ITV derived from 4DCT was statistically insignificantly larger than PPV144,0% and rPPV144,5% | NA |
| Xiao (2022) [31] | UQ 4DMRI generated by DDEM | Tumour motion errors (mm) | <1 mm in all directions | (1) Significantly enhanced overall image quality |

| | | | | |
|---|---|---|---|---|
| Feng (2023) [32] | 2D nav or 1D nav vs SSIM curve[6] | Motion CC | 0.886 ± 0.049 2D nav, 0.791 ± 0.148 1D nav | (1) The 2D nav outperformed the 1D nav in detecting respiratory variations and/or body movements during the off-view stage |
| Liu (2023) [33] | NeRP model[7] | SSIM | 0.98 ± 0.01 | (1) Image quality deceased at outside the two training phases. |
| | | GTV HD-95% | 2.41 ± 0.77 mm | |
| | | Mean GTV motion | <1 mm in all directions. | |
| Murray (2023) [35] | Movienet[8] Vs XD-GRASP | MS-SSIM | 0.93–0.96 Movienet, 0.98–0.99 XD-GRASP | (1) Significantly removed streaking artifact and improve overall image quality |
| | | MSE | <0.02 Movienet, <0.0005 XD-GRASP: | |
| Xiao (2023) [34] | HQ Mp D2R model[9] vs LQ 4DMRI | Relative ROI ME | <2.7 mm in all directions. | (1) Significantly enhanced image quality |

***Abbreviations:*** CC: Correlation Coefficient, CE-4DMRI: Contrast-enhanced 4DMRI, COV: Coefficient of variation, CR: contrast resolution, DCE: dynamic contrast enhancement, DDEM: dual-supervised deformation estimation model, dir-Reg: direct image registration, DR: Deformable registrations, DSC: Dice coefficient, ED: Euclidean Distances, SR: Super-resolution, HD: Hausdorff distance, iGRASP: iterative Golden-angle Radial Sparse Parallel MRI, MAD: Mean Absolute Difference, MDD: Motion Displacement Difference, ME: Motion errors, MoCo: 4D joint motion-compensated high-dimensional total variation algorithm, MoCoAve: motion correction averaging, MS-SSIM: multiscale- structure similarity index.NA: not applicable, Nav: navigator, nn-Reg: non-direct image registration, NS-4DMRI: non-selective excitation 4DMRI, rPPV: respiratory positional probability volume, RMSE: root means square error, ROI: region of interest, SD: Standard deviation, SG: Self-gating surrogates, SNR: signal to noise ratio, SR: Superior Reconstruction, SS-4DMRI: slab selective excitation 4DMRI, SSIM: structure similarity index, UQ: Ultra-quality, and XD-GRASP: Xtra-Dimensional Golden-angle Radial Sparse Parallel MR.

[1] Motion models: STATIC model, which assumes no motion and uses a mid-position 3D reference for treatment planning; AVG-RESP model, which determines respiratory phase using real-time 2DMRI, producing a time-weighted 4DMRI to reflect individual respiratory phases during radiation, and PCA model uses principal component analysis on 4DMRI deformation vector fields to generate a scalable motion model, adjusting for drifts and variations in breathing patterns by corresponding to real-time 2DMRI.

[2] MoCoAve: post-processing technique.

[3] 5DMRI: 4DMRI at different timepoints post contrast

[4] Dir-Reg: non-rigid image registration where all the phases directly register to end-exhale and end-inhale, and nn-Reg: non-rigid image registration where consecutive neighbouring phases are registered until the end-exhale and end-inhale in reached.

[5] D-Dracula 4D image reconstruction uses deep radial convolutional neural network, 4D-MoCo: 4D image reconstruction called 4D joint motion-compensated high-dimensional total variation,

[6] SSIM curve: The validation method involved calculating the SSIM between the most recent 3D image and all previous 3D images for each patient, resulting in a signal curve considered a ground-truth (3D reference).

[7] NeRP model: is an advanced MRI technique that uses sparse sampling and neural representation learning with a sparse prior for efficient 3D motion tracking in real-time.

[8] Movienet: a deep learning approach for 4D-MRI reconstruction

[9] D2R model uses a downsampling-invariant deformable registration (D2R) model for real-time, multi-parametric 4D image reconstruction.

## Supplementary material C

**Summary of the key findings from 4D MRI reconstructed from 3D MRI data acquisition**

| Author (Year) [Ref] | Validation comparing to 4DMR | Validation metrics | Other key information | |
|---|---|---|---|---|
| | | | **Motion and volume** | **Overall image quality of proposed 4DMRI** |
| Stemkens (2014) [10] | NA | Peak-to-Peak motion | -7.4 ± 1.6 mm duodenum.<br>-5.4 ± 0.7 mm tumour | (1) MRI navigator more accurate than respiratory bellows.<br>(2) Radial sampling reduced undersampling and artifacts |
| Deng (2015) [11] | real-time 2DMRI | Tumour CC | 0.938 (SI), < 0.8 (AP, LR) | (1) Less overall image quality (i.e. signal inhomogeneity) and variation in tissue contrast<br>(2) No statistically significant difference in image sharpness |
| | | MAD | ≤ 1.2 mm in (SI) | |
| | | MDD | <-0.8 mm (SI),<-1.6 mm (AP),< -0.7 mm (LR) | |
| Yang (2015) [12] | real-time 2DMRI | Tumour CC | 0.9 ± 0.0 (SI), 0.8 ± 0.1 (AP), 0.7 ± 0.18 (LR) | (1) Free of stitching artifacts |
| | | MAD | 0.8 ± 0.5 mm (SI), 0.4 ± 0.2 mm (AP), 0.5 ± 0.2 mm (LR) | |
| | 4DCT | Tumour CC | 0.9 ± 0.06 (SI), 0.7 ± 0.16 (AP), 0.4 ± 0.2 (LR) | |
| | | MAD | 1.1 ± 0.4 mm (SI), 0.5 ± 0.2 mm (AP), and 0.5 ± 0.3 mm (LR) | |
| | | SD-GTV from 10 phases | 0.8 1± 0.54 $cm^3$ 4DMRI, 1.02 ± 0.67 $cm^3$ 4DCT | |

| | | | | |
|---|---|---|---|---|
| Feng (2016) [13] | XD-GRASP vs iGRASP | NA | NA | (1) Improved overall image quality with less motion artifact compared to iGRASP |
| Jin (2016) [14] | de-noised vs raw data 4DMRI | Tumour CC | 0.9994 ± 0.0003 | (1) Improved overall image quality |
| | | SD-GTV from 10 phase | 0.6 ± 0.4 $cm^3$ 4DMRI<br>0.8 ± 0.6 $cm^3$ 4DCT | |
| Deng (2017) [15] | SS-4D-MRI vs NS-4D-MRI | Tumour CC | 0.96 ± 0.06 (SI), 0.78 ± 0.2 4 (AP) and 0.46 ± 0.44 (RL) | (1) Superior vessel delineation and higher SNR and CR<br>(2) Fewer streaking artifacts (4-point scale) |
| Stemkens (2017) [16] | Motion models[1] vs real-time 2DMRI | mean RMSEs | 2.69 ± 0.68 mm STATIC, 2.37 ± 0.78 mm AVG-RESP ,1.09 ± 0.47 mm PCA model | NA |
| Breuer (2018) [17] | 4DCT | NA | NA | (1) Superior lesion visualisation compared to 4DCT |
| Oar (2018) [18] | 4DCT | Median Tumour ED | 11.2 mm 4DCT,10.1 mm 4DMRI<br>median difference: -0.6 mm | (1) Superior edge detection and over all image quality (four-point scale) |
| Yang (2018) [19] | SS-4D-MRI vs NS-4D-MRI | CC | 0.93 ± 0.10 (SI), 0.65 ± 0.31 (AP), 0.77 ± 0.23 (LR) | (1) Enhanced imaging signal and increased vessel CNR compared to NS-4DMRI and 4DCT |
| Deng (2019) [20] | MoCoAve[2] vs non- MoCoAve | Tumour CC | 0.91 ± 0.08 (SI), 0.51 ± 0.44 (AP), 0.37 ± 0.23 (LR) | (1) Higher SNR, fewer artifacts and increased in overall image quality (3-point scale) (2) No statistically significant difference in image sharpness |
| | | Tumour MAD | 0.5 ± 0.3 mm (SI) | |
| | | SD-GTV from 10 phases | 1.4 8±1.35 $cm^3$ MoCoAve, 2.17±1.31 $cm^3$ non-MoCoAve | |
| Mickevicius and Paulson (2019) [21] | SR reconstructions | NA | NA | (1) The respiratory motion was well-defined without any mismatching of sorted slices |

| | | | | |
|---|---|---|---|---|
| Stemkens (2019) [22] | 5DMRI[3], CE-4DMRI vs real-time 2DMRI | SI GTV motion | CE-4DMRI demonstrated approximately 10% smaller motion than real-time 2DMRI | (1) 5DMRI reduced the motion artifact compared to DCE |
| Navest (2020) [23] | Noise-nav vs SG | NA | NA | (1) Less streaking artifacts compared to self-gating |
| Weick (2020) [24] | Dir-Reg[4] vs nn-Reg IR[4] | Median COV all ROIs | Reduced by 5.6% ± 5.3% for exhalation and 7.0% ± 4.2% for inhalation compared to the nn-Reg | (1) Superior overall image quality compared to nn-Reg (4-point scale) |
| Feng (2021) [25] | real-time 2DMRI | $R^2$ | 0.948 | (1) Suspected lesions were clearly visible in the 3D images across three planes. |
| Freedman (2021) [26] | 4D-Dracula[5] vs 4D-MoCo[5] | Median tumour ranges | Below 2.4 mm. | (1) Lower overall image quality (2) Clinically acceptable for contouring in RT (four-point scale) |
| | | Median inter-observer DSC | >0.86 GTV | |
| Romaguera (2021) [27] | 4DMRI vs Ultrasound | Volumetric Prediction Mean Error | 1.67 ± 1.68 mm | NA |
| Mansour (2022) [28] | XD-GRASP and DR | NA | NA | (1) The liver motion clearly showed the positions of both the tumour and liver in 10 phases |
| Thomas (2022) [29] | 4DCT | Dosimetric Coverage of PTVs from CT and MRI plans | ▪ No significant difference when optimised on their respective target<br>▪ Statistically significant lower of MRI target compared to CT target when they optimised on CT plan | (1) Equal or better liver tumours clarity at extreme phases (4-point Likert scale)<br>(2) Higher sharpness scores at extreme phases |
| | | Mean liver dose, OAR and ITVs volume | No statistically significant difference between CT and MR optimised plans | |

| | | | | |
|---|---|---|---|---|
| Wong (2022) [30] | 4DCT | ITV volume | The ITV derived from 4DCT was statistically insignificantly larger than PPV144,0% and rPPV144,5% | NA |
| Xiao (2022) [31] | UQ 4DMRI generated by DDEM | Tumour motion errors (mm) | <1 mm in all directions | (1) Significantly enhanced overall image quality |
| Feng (2023) [32] | 2D nav or 1D nav vs SSIM curve[6] | Motion CC | 0.886 ± 0.049 2D nav, 0.791 ± 0.148 1D nav | (1) The 2D nav outperformed the 1D nav in detecting respiratory variations and/or body movements during the off-view stage |
| Liu (2023) [33] | NeRP model[7] | SSIM | 0.98 ± 0.01 | (1) Image quality deceased at outside the two training phases. |
| | | GTV HD-95% | 2.41 ± 0.77 mm | |
| | | Mean GTV motion | <1 mm in all directions. | |
| Murray (2023) [35] | Movienet[8] Vs XD-GRASP | MS-SSIM | 0.93–0.96 Movienet, 0.98–0.99 XD-GRASP | (1) Significantly removed streaking artifact and improve overall image quality |
| | | MSE | <0.02 Movienet, <0.0005 XD-GRASP: | |
| Xiao (2023) [34] | HQ Mp D2R model[9] vs LQ 4DMRI | Relative ROI ME | <2.7 mm in all directions. | (1) Significantly enhanced image quality |

***Abbreviations:*** CC: Correlation Coefficient, CE-4DMRI: Contrast-enhanced 4DMRI, COV: Coefficient of variation, CR: contrast resolution, DCE: dynamic contrast enhancement, DDEM: dual-supervised deformation estimation model, dir-Reg: direct image registration, DR: Deformable registrations, DSC: Dice coefficient, ED: Euclidean Distances, SR: Super-resolution, HD: Hausdorff distance, iGRASP: iterative Golden-angle Radial Sparse Parallel MRI, MAD: Mean Absolute Difference, MDD: Motion Displacement Difference, ME: Motion errors, MoCo: 4D joint motion-compensated high-dimensional total variation algorithm, MoCoAve: motion correction averaging, MS-SSIM: multiscale- structure similarity index.NA: not applicable, Nav: navigator, nn-Reg: non-direct image registration, NS-4DMRI: non-selective excitation 4DMRI, rPPV: respiratory positional probability volume, RMSE: root means square error, ROI: region of interest, SD: Standard deviation, SG: Self-gating surrogates, SNR: signal to noise ratio, SR: Superior Reconstruction, SS-4DMRI: slab selective excitation 4DMRI, SSIM: structure similarity index, UQ: Ultra-quality, and XD-GRASP: Xtra-Dimensional Golden-angle Radial Sparse Parallel MR.

[1] Motion models: STATIC model, which assumes no motion and uses a mid-position 3D reference for treatment planning; AVG-RESP model, which determines respiratory phase using real-time 2DMRI, producing a time-weighted 4DMRI to reflect individual respiratory phases during radiation, and PCA model uses principal component analysis on 4DMRI deformation vector fields to generate a scalable motion model, adjusting for drifts and variations in breathing patterns by corresponding to real-time 2DMRI.

[2] MoCoAve: post-processing technique.

[3] 5DMRI: 4DMRI at different timepoints post contrast

[4] Dir-Reg: non-rigid image registration where all the phases directly register to end-exhale and end-inhale, and nn-Reg: non-rigid image registration where consecutive neighbouring phases are registered until the end-exhale and end-inhale in reached.

[5] D-Dracula 4D image reconstruction uses deep radial convolutional neural network, 4D-MoCo: 4D image reconstruction called 4D joint motion-compensated high-dimensional total variation,
[6] SSIM curve: The validation method involved calculating the SSIM between the most recent 3D image and all previous 3D images for each patient, resulting in a signal curve considered a ground-truth (3D reference).
[7] NeRP model: is an advanced MRI technique that uses sparse sampling and neural representation learning with a sparse prior for efficient 3D motion tracking in real-time.
[8] Movienet: a deep learning approach for 4D-MRI reconstruction
[9] D2R model uses a downsampling-invariant deformable registration (D2R) model for real-time, multi-parametric 4D image reconstruction.

## Supplementary material D

**Overview of the key imaging parameters and methodologies used for different abdominal organs to reconstruct 4D MRI from multislice-2D MRI data acquisition**

| **Author (year)[Ref]** | **Organ (Patients number)** | **Acquisition type** | **Sequence (Image contrast)** | **Surrogate** | **Binning Methods** | **Spatial Resolution** pixel size, slice thickness **(Temporal Resolution)** | **FOV** | **Scan Time (Recon. Time)** |
|---|---|---|---|---|---|---|---|---|
| Liu (2014) [37] | Liver (7) | 2D Cartesian, cine, sagittal and axial | T2/T1w GRE | BA | 10 Phase | 1.9×1.9 x5 mm (333 ms) | 480×480mm | NR |
| Yang (2014) **[38]** | Liver (7) | 2D Cartesian, cine, axial | T2/T1w GRE | BA | Phase | 1.6–2.5×2.8–3.75 x5 mm (333 ms) | 300–480× 360–480 mm | NR |
| Glide-hurst (2015) **[39]** | Stomach (1) Liver (1) | 2D Sagittal | T2w-TSE | Respiratory bellows | 4,8 Amplitude | 1×1x4 mm (NR) | 380×210x200 mm | 7–11 min (NR) |
| Paganelli (2015) [40] | Liver (24) | 2D Cartesian, interleaved, Oblique | T2/T1w GRE | MI | 8 Amplitude and Phase | 1.28 ×1.28x5 mm | 320×285x100 mm | 1.2 min (2 min) |

| | | | | | | | | |
|---|---|---|---|---|---|---|---|---|
| | | | | | | (180 ms) | | |
| Uh (2016) [41] | Abdominal tumours (6) | 2D Cartesian, cine, coronal | T2/T1 GRE | Diaphragm nav | 10 Amplitude probability | 1.8×1.8 x5 mm (333 ms) | 350×350x100 mm | 8 min 12 s (NR) |
| Uh (2017**) [42]** | Abdominal tumours (36) | 2D Cartesian, cine, coronal | T2/T1 GRE | Diaphragm nav | 10 Amplitude probability | x1.8x 4-5 mm (333 ms) | 350x350x140 mm | 11 – 20 min (NR) |
| Kesteren (2019) [43] | Pancreas (1) Stomach (1) | 2D Cartesian, interleaved, coronal | T2-w-SS | 1D nav | 10 Amplitude | 0.78×0.78x5 mm (NR) | 400×200x55 mm | 6 min (NR) |
| Meschini (2019) [44] | Liver (7) | 2D Cartesian, interleaved, Oblique | T2/T1 GRE | K-medoids clustering | 8 clustering approach | 1.28×1.28 x5 mm (180ms) | 12.5 cm slab | NR |
| Uh (2019) [36] | Abdominal tumours (6) | 2D Cartesian, coronal | T2w-TSE | 1D navigator | 10 Amplitude | 1.5×1.5x4 mm (NR) | 300×300x200 mm | 4-7 min (NR) |
| Chen (2021) [45] | Liver (23) | 2D Cartesian, NA | T2w-TSE | 1D nav | 10 Phase | 0.94×0.94x5 mm (NR) | NR | 5 min (NR) |
| Meschini (2021) [46] | Pancreas (5) Liver (2) | 2D cartesian, sagittal | T2/T1 GRE | NA | 8 Phase | NR | 12.5 cm slab | NR |
| Zhang (2021) [47] | Liver (5) | 2D Cartesian, Cine mode, axial | T2/T1 GRE | BA | 10 Phase | 1.88x1.88x5 mm (300ms) | NA | NR |
| Liu (2023) [48] | Liver (13) | 2D spiral, Sagittal | MRF-FISP | MRF signals | 8 Phase | 1.17x1.17x5 mm (NR) | 300x300 mm | NR |

***Abbreviations*: NR:** not reported, second, min: minutes, MRF:MR fingerprinting, Recon: Reconstruction, MI: **m**utual Information, Nav: navigator.

## Supplementary material E

**Summary of the key information from 4D MRI reconstructed from multislice 2D MRI data acquisition**

| Author (year) [REF] | Validation comparing to 4DMR | Validation metrics | Other key information | |
|---|---|---|---|---|
| | | | Motion | Overall image quality of proposed 4DMRI |
| Liu (2014)[37] | real-time 2DMRI | MAD | 1.5 ±1.6 mm (SI), 2.1±1.9 mm (RL), and 1.1 ± 1.0 mm (AP) | NA |
| | | Relative Error (%) | 14 ± 9.1% (SI), 21 ± 16% (AP), and 50 ± 35% (RL) | |
| Yang (2014)[38] | real-time 2DMRI | Tumour CC | 0.97 ± 0.03 (SI), 0.97 ± 0.02 (AP), and 0.99 ± 0.04 (RL) | (1) Superior CNR |
| | | Mean Tumour Amplitude | 0.6 ± 0.2 mm (SI), 0.3 ± 0.2 mm (AP), and 0.1 4 ± 0.1 mm (RL) | |
| | 4DCT | Tumour CC | 0.95 ± 0.02 (SI), 0.94 ± 0.02 (AP), and 0.96 ± 0.02 (RL) | |
| | | Mean Tumour Amplitude | 0.7 ± 0.0 mm (SI), 0.3 ± 0.1 mm (AP), and 0.2 ± 0.1 mm (RL) | |
| Glide-hurst (2015)[39] | NA | NA | NA | (1) High image quality with no significant artifact across all image series |
| Paganelli (2015)[39] | belt sorting vs MI soring | Median RMSE | 1.4 ± 1.1 mm in phase binning<br>1.2 ± 0.9 mm in amplitude binning | (1) Less motion artifact |
| Uh (2016)[41] | real-time 2DMRI | MAD | 1.4 mm ± 0.4 mm (AP) | NA |
| Uh (2017)[42] | previous 4DCT studies. | peak-to-peak motion | kidney motion was <5 mm<br>liver and spleen motion were often >10 | NA |

| | | | | |
|---|---|---|---|---|
| Kesteren (2019)[43] | Min95 binning[1] vs Phase, Amplitude binning[1] | NA | NA | (1) Phase and MaxIE binning both demonstrated sorting artifacts compared to MeanIE and Min95 strategies |
| Meschini (2019)[44] | Clustering sorting[2] vs MI and external surrogate (belt) | Median RMSE | 0.97-1.66 mm MI, 1.24 to 1.89 mm multiple points, 1.43 to 2.27 mm single point, 1.74 to 3.72 mm external surrogate | (1) Image quality was similar for MI and clustering sorting, but an external surrogate showed more artifacts. |
| Uh (2019) [36] | 4DCT | CTV to ITV volume | 2-46% 4DMRI, 9-63% 4DCT | NA |
| | | DSC | 92-95% for the youngest patients with similar breathing characteristics<br>82-88% for other patients due to variation in breathing characteristics. | |
| Chen (2021)[45] | 4DCT | Mean Volume Differences | Statistically significant reduction in GTV (16%) and ITV (12%) | (1) Sever artifacts were found more in 4DCT compared to 4DMRI |
| | | Mean GTV motion difference | 0.7 (LR), 0.9 (AP), and 1.9 (SI) mm | |
| Meschini (2021)[46] | 3D model validation with 4DMRI | DIR errors from reference points | 1.33 mm | NA |
| | | Tumour COM | 1.8 mm | |
| Zhang (2021)[47] | Original 4DMRI vs TEC 4DMRI | MAD | 0.5 ± 0.5 mm (SI) diaphragm, 0.7 ± 0.4 mm (SI) tumour | (1) The CNR of the tumour showed a statistically significant increase in TEC 4DMRI |
| Lui (2023)[48] | 4DMRF vs real-time 2DMRI | Mean amplitude motion | 1.5 ± 1.1 mm (SI) and 0.8 ± 0.6 mm (AP) | NA |
| | | Mean PCC for motion | 0.95 ± 0.05 (SI) and 0.93 ± 0.09 (AP) | |

***Abbreviations:*** BA: body area, CC: correlation coefficient, CNR: contrast-to-noise ratio, COM: tumour centers of mass, CoV: coefficient of variation, MAD: mean absolute difference, DIR: deformable image registration, DSC: Dice similarity coefficient, MAD: Mean Absolute Difference, MI: mutual information, MRF: magnetic resonance fingerprinting, mDSC: mean Dice coefficient, NA: not applicable, PCC: Pearson correlation coefficient, RMSE: diaphragm fitting root mean square errors, RL: right-left, SI: superior inferior, SSIM: structural similarity index measure, TEC: synthetic image contrast referred as tumour enhanced contrast 4DMRI .

[1] Min95 binning: amplitude binning where 95% of the acquired data included at end-inhale and end-exhale, MaxIE: amplitude binning, where inclusion thresholds are the end-inhale and end-exhale of diaphragm position, MeanIE: amplitude binning, where inclusion thresholds are the mean max-inhale and the mean end-exhale of diaphragm position,

[2] A clustering sorting: single points: the clustering is based on single internal reference point that tracked automatically, multiple points: the clustering is based on several internal reference points that tracked automatically.

# Appendix B Additional information (Chapter3)

## B.1 Methodology update

An updated systematic review search was conducted in May 2025, covering studies published from January 2024 to May2025, using the same databases, search strategy, and inclusion/exclusion criteria described in Chapter 3.

### B.1.1 Findings

The updated search identified nine additional studies meeting the inclusion criteria [1-9]. The included papers were grouped according to their acquisition methods, as described previously in Chapter 3. Seven of these proposed 4D MRI reconstruction from 3D acquisitions, whereas two used 4D MRI reconstructed from multi-slice 2D acquisitions.

### B.1.2 4D MRI reconstructed from 3D MRI data acquisition

Seven studies investigated advances in 4D MRI reconstruction using deep learning or motion modelling methods [1-9]. Two studies proposed multitasking MRI (MT-MRI) for abdominal radiotherapy planning, generating T1w, T2w, and proton density contrasts within a single 4D acquisition to provide an inherently co-registered multi-contrast sequence and respiratory-resolved 4D MRI, thereby enhancing tumour delineation for liver cancers [1, 4].The initial feasibility work by Chen et al.[1] assessed MT-MRI in five patients, demonstrating its technical robustness against a digital phantom, a commercial T1w 4D MRI sequence (StarVIBE), and a multislice T2 BLADE, which confirmed good image quality with acquisition achieved at 1.6 × 1.6 × 3.2 $mm^3$ resolution in 8 minute scan and 10 minute reconstruction times. The follow-up clinical study by Chau et al.[4] extended this work by implementing MT-MRI on an MR simulator and comparing it with post-contrast 4D CT. In 54 patients, tumour visibility and motion assessment were evaluated, and in a subset of 17 patients replanning was performed to assess target coverage between 4D MRI and 4D CT. This study demonstrated superior tumour visualisation and more accurate motion assessment than 4D CT, with significantly greater mean superior–inferior (SI) motion magnitude of 9.3 mm in MT-MRI vs 5.9 mm in 4D

CT. These findings highlighted that MT-MRI was a promising alternative to 4D CT for motion assessment and target delineation in liver radiotherapy planning.

Further development of ultra-quality (UQ) 4D MRI has been investigated, which enables more accurate tumour contouring and improved dosimetric accuracy compared to 4D CT in liver cancer [3, 6]. Liao et al. [6] combined a rapid low-resolution 4D THRIVE scan (3 × 3 × 3 $mm^3$ voxels, 0.7 s temporal resolution, 1-min acquisition) with high-resolution 3D MRI sequences to generate UQ 4D MRI across 10 respiratory phases. A dual-supervised deformation estimation model (DDEM) was used to generate DVFs for each phase, which were then applied to the high-resolution 3D MRI to create UQ 4D MRI. In a cohort of 13 patients, SI tumour motion measured on UQ 4D MRI was highly consistent with cine MRI, confirming accurate motion detection. Furthermore, ITV derived from UQ 4D MRI showed no significant volumetric difference compared with ITV derived from 4D CT (mean difference −1.6%). Li et al. [3] has extended this approach to investigate the dosimetric impact of multi-parametric UQ 4D MRI in 20 liver cancer patients. Low-resolution TWIST-VIBE scans (2.7 mm isotropic voxels) were combined with high-resolution 3D T1w and T2w images to generate multi-contrast UQ 4D MRI across 10 respiratory phases. Target contours were drawn using either 3D MRI or multi-parametric 4D MRI, and treatment plans were compared. The results showed that 3D MRI guided delineation tended to underestimate target volume and compromise dose coverage, whereas 4D MRI provided more accurate contours and maintained better target coverage.

Two studies used deep learning methods to accelerate reconstruction and improve image resolution for 4D MRI [2, 5]. Zhi et al. [2] developed a deep learning model that combined motion estimation and super-resolution into a single framework. Using prior 3D MRI information for anatomical guidance, the method was tested in 27 liver cancer patients. It successfully generated 4D MRI with higher spatiotemporal resolution, more accurate motion fields, and clearer tumour and diaphragm motion than existing deep learning networks and three state-of-the-art conventional algorithms. Xu et al. [5] developed a deep learning model to accelerate 4D MRI reconstruction while maintaining image quality. 48 patients were imaged using a free-breathing T1w SOS sequence, achieving 1.3 × 1.3 $mm^2$ in-plane resolution, 3 mm slice thickness, and an 8-10 minute scan

time. Compared with compressed sensing (CS) and other models, the method produced higher image quality with an inference time of only 0.15 s per volume, faster than CS (120 s). The model demonstrated rapid, high-quality 4D MRI reconstruction. Overall, both studies showed that deep learning methods can deliver accurate 4D MRI with improved resolution and dramatically reduced reconstruction times, supporting more precise motion assessment and target delineation in liver radiotherapy. Lastly, another study investigated 4D MRI with enhanced T1w contrast [7]. Chen et al. [7] proposed MP-Grasp4D, a 4D MRI technique that integrates inversion recovery (IR) preparation into stack-of-stars (SOS) 4D MRI to improve T1w contrast. MP-Grasp4D achieves sub-second temporal resolution (0.16 s per 3D volume) while simultaneously capturing respiratory motion and IR-induced contrast changes without the need for explicit motion binning. The method was evaluated in nine patients with liver cancer and compared with conventional Grasp4D. MP-Grasp4D achieved higher image quality scores across. Importantly, diagnostic quality was maintained even when scan times were shortened from 8 to 3–5 minutes. Overall, MP-Grasp4D provides 4D MRI with improved T1w contrast and high temporal resolution, offering clearer delineation of abdominal organs and lesions compared with standard Grasp4D.

### B.1.3 4D MRI reconstructed from multislice 2D MRI data acquisition

While the majority of recent work has focused on 4D MRI reconstructed from 3D acquisitions, two studies investigated multislice 2D MRI acquisitions [8, 9]. Wong et al. [9] developed a 4D magnetic resonance fingerprinting (4D-MRF) framework to reconstruct multiphase T1/T2 maps during free breathing in six liver cancer patients. Their proposed method of 4D MRF reduced mapping errors compared with conventional MRF and improved inter-phase consistency. Their findings demonstrated the feasibility of quantitative, motion-resolved T1/T2 mapping for liver radiotherapy planning, supporting more precise target characterisation and motion management. Wang et al. [8] evaluated 4D MRI in 76 patients SABR using contrast-enhanced T1w and two-phase T2w sequences. The two-phase T2w 4D MRI acquisition enabled motion assessment at end-inspiration and end-expiration using amplitude triggering techniques, with a slice thickness of 3–5 mm. Compared with CT, 4D MRI provided superior image quality, with strong clinical outcomes, including a 1-

year local control rate of 97.3% and only mild toxicities. These findings demonstrate the feasibility and clinical benefit of 4D MRI as an alternative to 4D CT for liver SBRT. However, these studies still achieved insufficient slice thickness for radiotherapy clinical use. These additional findings do not change any of the conclusions presented in the original paper (Chapter 3).

### B.1.4 References


[1] Chen JZ, Christodoulou AG, Han P, Xiao JY, Han F, Hu ZH, et al. Abdominal MR Multitasking for radiotherapy treatment planning: A motion-resolved and multicontrast 3D imaging approach. Magn Reson Med. 2025;93:108-20. 10.1002/mrm.30256.

[2] Zhi SH, Wang YH, Xiao HN, Bai T, Li B, Tang YS, et al. Coarse-Super-Resolution-Fine Network (CoSF-Net): A Unified End-to-End Neural Network for 4D-MRI With Simultaneous Motion Estimation and Super-Resolution. Ieee Transactions on Medical Imaging. 2024;43:162-74. 10.1109/tmi.2023.3294245.

[3] Li S, Zhu X, Xiao H, Liu W, Zhang Y, Cai J, et al. Dosimetric investigation of multi-parametric 4D-MRI for radiotherapy in liver cancer. Radiat Oncol. 2025;20:51

[4] April Chau OW, Geoghegan T, Everts J, Chen J, Feng M, Chen WC, et al. Multi-contrast 4DMR via MR multitasking: Early clinical experience and implication for liver stereotactic body radiation therapy. Radiotherapy and oncology : journal of the European Society for Therapeutic Radiology and Oncology. 2025;206:110839. https://dx.doi.org/10.1016/j.radonc.2025.110839.

[5] Xu D, Miao X, Liu HJ, Scholey JE, Yang WS, Feng M, et al. Paired conditional generative adversarial network for highly accelerated liver 4D MRI. Physics in Medicine and Biology. 2024;69. 10.1088/1361-6560/ad5489.

[6] Liao Y-P, Xiao H, Wang P, Li T, Aguilera TA, Visak JD, et al. Internal Target Volume Estimation for Liver Cancer Radiation Therapy Using an Ultra Quality 4D MRI. Advances in Radiation Oncology. 2025:101774

[7] Chen JJ, Xia D, Huang CC, Shanbhogue K, Chandarana H, Feng L. Free-breathing time-resolved 4D MRI with improved T1-weighting contrast. Nmr in Biomedicine. 2024;37. 10.1002/nbm.5247.

[8] Wang HZ, Zheng X, Sun JW, Zhu XG, Dong DZ, Du Y, et al. 4D-MRI assisted stereotactic body radiation therapy for unresectable colorectal cancer liver metastases. CLINICAL AND TRANSLATIONAL RADIATION ONCOLOGY. 2024;45. 10.1016/j.ctro.2023.100714.

[9] Wong YL, Li T, Liu C, Lee HFV, Cheung LYA, Hui ESK, et al. Reconstruction of multi-phase parametric maps in 4D-magnetic resonance fingerprinting (4D-MRF) by optimization of local T1 and T2 sensitivities. Medical Physics. 2024;51:4721-35. 10.1002/mp.17001.

# Appendix C  Conferences participation

Conference contributions linked to Chapters 3 to 5:

**Chapter 3**

- A systematic review of 4D MRI techniques for abdominal radiotherapy treatment planning *(Digital Poster).*
  *European Society for Radiotherapy and Oncology (ESTRO) 2024; Glasgow, UK.*

**Chapter 4**

- Deep learning-based synthetic CT generation for liver MR-only radiotherapy planning *(Digital Poster).*
  *10th MR in RT Symposium 2024; Rome, Italy.*
- Evaluating the dosimetric and positioning accuracy of a deep learning based synthetic-CT generation model for MRI-only planned liver radiotherapy *(oral presentation).*
  *Annual Radiotherapy and Oncology Meeting (BIR) 2025; London, UK.*

**Chapter 5**

- Clinical feasibility of using a commercial synthetic-CT solution for brain MRI-Only radiotherapy treatment planning *(Proffered Paper).*
  *European Society for Radiotherapy and Oncology (ESTRO) 2025; Vienna, Austria .*

**Awards**

- Leeds Oncology Research Day (LORD) 2022; Leeds
  - *Winner, Best Allied Health prize (oral presentation).*
- International PhD Academy Away Day 2024: Leeds
  - *Winner, Best 5-minute presentation.*

# Appendix D LeedsCAT approvals

The Leeds Teaching Hospitals NHS Trust

UNIVERSITY OF LEEDS

**Research Database**: Leeds Cancer Centre Computer Aided Theragnostics (LeedsCAT)
v1.0
REC reference: 19/YH/0300
IRAS project ID: 255585

**Radiotherapy Research Department**
Level 4 Offices, Bexley Wing
Leeds Teaching Hospitals NHS Trust
Leeds
LS97TF

DATE 30/03/2023

Dear Dr Bash al-Qaisieh and colleagues,

**RE project: Developing an MRI-only pathway for liver radiotherapy treatments (VIPRE)**

Your project has been considered by the LeedsCAT Governance board in March 2023. The LeedsCAT Governance board consists of representatives from Research and Innovation, Information Governance, PPI and experts in Radiotherapy.

A favourable decision was made under the terms below, and we can confirm that we are able to approve your project within the scope of the LeedsCAT research database ethical approval.

Terms:

- In order to comply with the NHS national data opt out policy (in effect from 31st July 2022) if you are responsible for the patient list needed for your research, you need to ensure that the data you plan to use does not come from those that have opted out. To check this please you're your NHS numbers list to jack.baldwin@nhs.net.
- With respect to the use of data we expect that you will comply with GDPR, Caldicott guidance, Information Governance procedures and all Trust policies
- If there are any significant changes to the project, including change in the list of people who will access project data, you will need to notify the LeedsCAT project manager. You will be routinely asked every 6 months to provide a project update, including changes to the project form and any outputs from the project.
- When the project has ended you will take the necessary steps to ensure the data is deleted or archived correctly.

Regards,

John Lilley
*on behalf of the LeedsCAT Governance Board*

LEEDS RADIOTHERAPY RESEARCH

The Leeds Teaching Hospitals NHS Trust

UNIVERSITY OF LEEDS

**Research Database**: Leeds Cancer Centre Computer Aided Theragnostics (LeedsCAT)
v2.0
REC reference: 19/YH/0143
IRAS project ID: 342888

**Radiotherapy Research Department**
Level 4 Offices, Bexley Wing
Leeds Teaching Hospitals NHS Trust
Leeds
LS97TF

17/9/24

Dear Bashar

RE project:

Clinical feasibility of a commercial synthetic computed tomography solution for brain MRI-only radiotherapy.

Your project has been considered by the LeedsCAT Governance board in September 2024. The LeedsCAT Governance board consists of representatives from Research and Innovation, Information Governance, PPI and experts in Radiotherapy.

A favourable decision was made, and we can confirm that we are able to approve your project within the scope of the LeedsCAT research database ethical approval.

Terms:

- In order to comply with the NHS national data opt out policy (in effect from 31st July 2022) if you are responsible for the patient list needed for your research, you need to ensure that the data you plan to use does not come from those that have opted out. To check this please email your NHS numbers list to jack.baldwin@nhs.net.
- With respect to the use of data we expect that you will comply with GDPR, Caldicott guidance, Information Governance procedures and all Trust policies
- If there are any significant changes to the project, including change in the list of people who will access project data, you will need to notify the LeedsCAT project manager
- When the project has ended you will take the necessary steps to ensure the data is deleted or archived correctly.

Regards,

John Lilley
*on behalf of the LeedsCAT Governance Board*

LEEDS RADIOTHERAPY RESEARCH

# Appendix E  Published papers

Chapter 3: Published in Physics and Imaging in Radiation Oncology (2024).

Chapter 4: Published in Biomedical Physics & Engineering Express (2025).

Chapter 5: Published in Technical Innovations & Patient Support in Radiation Oncology (2025).

Copies of the published articles are included in this appendix.